

ABANT İZZET BAYSAL UNIVERSITY
THE GRADUATE SCHOOL OF NATURAL AND
APPLIED SCIENCES
DEPARTMENT OF PHYSICS



STRUCTURAL AND OPTICAL CHARACTERIZATION OF
CADMIUM ZINC TELLURIUM THIN FILMS USED IN
CADMIUM ZINC TELLURIUM RADIATION DETECTORS

DOCTOR OF PHILOSOPHY

HASAN MALKAŞ

BOLU, DECEMBER 2015

APPROVAL OF THE THESIS

STRUCTURAL AND OPTICAL CHARACTERIZATION OF CADMIUM ZINC TELLURIUM THIN FILMS USED IN CADMIUM ZINC TELLURIUM RADIATION DETECTORS submitted by **Hasan MALKAŞ** in partial fulfillment of the requirements for the degree of Doctor of Philosophy in **Department of Physics, Abant Izzet Baysal University** by,

Examining Committee Members

Signature

Supervisor

Prof. Dr. Ercan YILMAZ AIBU



Member

Prof. Dr. Raşit TURAN METU



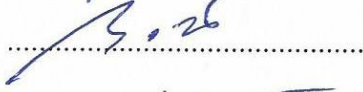
Member

Prof. Dr. Atilla KILIÇ AIBU



Member

Prof. Dr. Çetin BOZKURT AIBU



Member

Assoc Prof. Dr. Aliekber AKTAĞ AIBU



December 02, 2015

Prof. Dr. Duran KARAKAŞ

Director, **Graduate School of Natural and Applied Sciences**

DECLARATION

I hereby declare that all information in this document has been obtained and presented in accordance with academic rules and ethical conduct. I also declare that, as required by these rules and conduct, I have fully cited and referenced all material and results that are not original to this work.

Hasan MALKAŞ

A handwritten signature in blue ink, consisting of stylized initials and a surname, positioned above a horizontal line.

ABSTRACT

STRUCTURAL AND OPTICAL CHARACTERIZATION OF CADMIUM ZINC TELLURIUM THIN FILMS USED IN CADMIUM ZINC TELLURIUM RADIATION DETECTORS

PHD THESIS

HASAN MALKAŞ

**ABANT IZZET BAYSAL UNIVERSITY GRADUATE SCHOOL OF
NATURAL AND APPLIED SCIENCES**

DEPARTMENT OF PHYSICS

(SUPERVISOR: Prof. Dr. ERCAN YILMAZ)

BOLU, DECEMBER 2015

The microstructural and morphological characterizations of Cadmium Zinc Tellur (CZT) thin films were studied in details. The CZT thin films were deposited on glass substrates at 200, 300 and 400°C by radio frequency magnetron sputtering technique and annealed at 200, 300 and 450°C for an hour under N₂ and mixed N₂H₂ ambient at atmospheric pressure. X-ray Diffraction (XRD), Energy Dispersive Spectroscopy (EDS), Scanning Electron Microscopy (SEM), Atomic Force Microscopy (AFM), X-ray Photoelectron Spectroscopy (XPS), and UV transmission spectroscopy measurements were performed.

The XRD measurements emphasized that the annealed CZT films have a cubic-oriented (111), (220) and (311) polycrystalline structure, whereas as deposited films are mostly-amorphous. The effects of sputtering and annealing temperatures on the composition of the thin films were also discussed. EDS analysis was used to study the chemical composition of source and CZT thin films. SEM was used for surface morphology. It was concluded that post-annealing and deposition temperatures have explicitly effects on variation of the CZT thin film structure and morphology. AFM was used to study roughness of the CZT thin films which deposited under various sputtering and annealing temperatures. Then XPS measurements were performed in the depth profiling mode to comprehend the chemical composition of the films. Finally, transmission measurements were performed to find out band gaps of the samples. The optimum conditions were revealed for CZT deposition in accordance with their applications.

KEYWORDS: CdZnTe Thin Films, Sputtering, XRD, XPS, EDS, SEM, AFM.

ÖZET

**KADMİYUM ÇİNKO TELLERYUM RADYASYON DEDEKTÖRLERİNDE
KULLANILAN KADMİYUM ÇİNKO TELLERYUM İNCE FLİMLERİN
YAPISAL VE OPTİK KARAKTERİZASYONU
DOKTORA TEZİ
HASAN MALKAŞ
ABANT İZZET BAYSAL ÜNİVERSİTESİ FEN BİLİMLERİ ENSTİTÜSÜ
FİZİK ANABİLİM DALI
(TEZ DANIŞMANI: Prof. Dr. ERCAN YILMAZ)**

BOLU, ARALIK - 2015

Kadmiyum Çinko Tellür (CZT) ince filmlerin mikro yapısal ve morfolojiksel karakterizasyonu detaylı olarak incelendi. CZT ince filmler cam alt taşlar üzerine 200, 300 and 400°C' de radyo frekans magnetron püskürtme yöntemiyle üretildi. Üretilen filmler 200, 300 ve 450°C' de atmosferik basınçta N₂ ve karışık N₂H₂ ortamında bir saat süre ile tavlandı. X-Işınları Kırınımı (XRD), Enerji Dağılımlı X-Işınları Spektroskopisi (EDS), Tarayıcı Electron Mikroskopisi (SEM), Atomik Kuvvet Mikroskobu (AFM), X-Işınları Foto Elektron Spektroskopisi (XPS) ve UV geçirir spektroskopisi ölçümleri yapıldı.

Tavlanmayan filmlerde çoğunlukla amorf yapı gözlenirken, XRD ölçümleri tavllanmış CZT filmlerin kübik yönelimli (111), (220) ve (311) polikristal yapıya sahip olduğunu göstermektedir. Aynı zamanda büyütme ve tavlama sıcaklıklarının ince filmlerin yapısal kompozisyonu üzerindeki etkisi tartışılmıştır. EDS analizi kaynağın ve ince filmlerin kimyasal bileşimlerini araştırmak için kullanılmıştır. SEM yüzey morfolojisi için kullanılmıştır. Tavlama ve büyütme sıcaklığının CZT ince film yapısı ve morfolojisinin değişimi üzerinde belirgin bir etkisinin olduğu gözlenmiştir. AFM, çeşitli büyütme ve tavlama sıcaklıkları altında üretilen CZT ince filmlerin pürüzlüğünü incelemek için kullanılmıştır. XPS ölçümleri filmlerin kimyasal bileşimini anlamak amacıyla derinlik görüntü modunda yapılmıştır. Son olarak, transmisyon ölçümleri örneklerin bant aralıklarını belirlemek için yapılmıştır. En iyi CZT filmlerin büyütüldüğü en uygun şartlar belirlenmiştir.

ANAHTAR KELİMELELER: CdZnTe İnce Filmler, Püskürtme, XRD, XPS, EDS, SEM, AFM.

TABLE OF CONTENTS

	<u>Page</u>
ABSTRACT	v
ÖZET	vi
TABLE OF CONTENTS	vii
LIST OF FIGURES	ix
LIST OF TABLES	xiv
LIST OF ABBREVIATIONS AND SYMBOLS	xv
1. INTRODUCTION	1
2 THEORETICAL CONSIDERATIONS	7
2.1 Introduction	7
2.2 Semiconductor Materials.....	7
2.2.1. Structure of II-VI Materials	7
2.2.2. Band Structure of Semiconductors	9
2.3 Semiconductor Detectors.....	11
2.4 CdTe and CZT Detectors.....	11
2.5 Thin Film Growth Techniques	12
2.6 Material Characterization Techniques.....	16
2.6.1 Surface Analysis Methods	16
2.6.1.1 X-ray Photoelectron Spectroscopy (XPS)	17
2.6.1.2 Energy Dispersive Spectroscopy (EDS-EDX)	18
2.6.2 Microscopy Techniques	19
2.6.2.1 Scanning Electron Microscopy (SEM).....	20
2.6.2.2 Atomic Force Microscopy (AFM).....	20
2.6.3 Structural Characterization	22
2.6.3.1 X-ray Diffraction Technique.....	22
2.6.4 Optical Characterization	24
2.6.4.1 Optical Absorption.....	24
3. MATERIALS AND METHODS	26
3.1 Introduction	26
3.2 Deposition of Thin films	26
3.2.1 Substrate Preparation	26
3.2.2 Growth of CZT Thin Films by Sputtering Technique	27
3.3 Structural, Compositional and Surface Characterization	29
3.3.1 X-Ray Diffraction (XRD)	29
3.3.2 Energy Dispersive X-ray Analysis (EDXA) Measurements	30
3.3.3 Scanning Electron Microscopy (SEM).....	31
3.3.4 Atomic Force Microscopy (AFM)	32
3.3.5 X-ray Photoelectron Spectroscopy (XPS) Measurements	33
3.4 Optical Analysis	34
3.4.1 Absorption and Transmission Measurements.....	34

4. RESULTS AND DISCUSSIONS	35
4.1 Introduction	35
4.2 Characterization of CZT Thin Films Deposited by Sputtering Technique	35
4.2.1 Structural Analysis.....	35
4.2.2 Surface Morphology	44
4.2.2.1 SEM Measurements	44
4.2.2.2 AFM Measurements.....	51
4.2.3 Chemical Composition Analysis	62
4.2.4 Compositional Analysis.....	70
4.2.5 Optical Analysis	79
4.2.5.1 Absorption and Transmission Measurements	79
4.2.5.2 Bandgap of the Deposited CZT Films	81
5. CONCLUSIONS AND RECOMMENDATIONS	85
6. REFERENCES.....	87
7. CURRICULUM VITAE	95

LIST OF FIGURES

	<u>Page</u>
Figure 2.1. Zinc blende crystal structure of CdTe and ZnTe.....	8
Figure 2.2. Zinc blende crystal structure of CZT.....	9
Figure 2.3. The energy band structure diagrams for insulators, semiconductors, and conductors.....	10
Figure 2.4. Schematic diagram of XPS method	17
Figure 2.5. Schematic diagram of EDX-EDS system.....	19
Figure 2.6. Illustration of an AFM	21
Figure 2.7. X-rays Diffraction from parallel planes	23
Figure 2.8. A schematic diagram of the direct and indirect bandgap of semiconductor.....	25
Figure 3.1. Sputtering system used for deposition of CZT thin films. The devices of the sputtering system are: 1. Magnetron heads, 2. Substrate stage, 3. Heating elements (halogen lamps), 4. Thickness measuring crystal, 5. Ar gas flow control unit, 6. Vacuum valves, 7. Turbo molecular pump, 8. Roughing pump, 9. Substrate holder rotating arrangement, 10. RF/ DC magnetron connections, 11. Water Cooling System, and 12. System control unit	28
Figure 3.2. Vaksis three magnetron DC/RF sputtering system in Physics Department in Middle East Technical University.....	29
Figure 3.3. Rigaku MultiFlex X-Ray Diffractometer in Physics Department at Abant Izzet Baysal University.....	30
Figure 3.4. Scanning Electron Microscopy in Physics Department at Abant Izzet Baysal University.....	32
Figure 3.5. XPS System in Central Laboratory of Middle East Technical University.....	33
Figure 4.1. XRD spectra of CZT thin films grown at 200°C (as-grown) and annealed at 300°C and 450°C under N ₂ ambient, respectively.....	36
Figure 4.2. XRD spectra of CZT thin films grown at 200°C (as-grown) and annealed at 300°C and 450°C under N ₂ H ₂ ambient, respectively.....	37
Figure 4.3. XRD spectra of CZT thin films grown at 300°C (as-grown) and annealed at 300°C and 450°C under N ₂ ambient, respectively.....	37
Figure 4.4. XRD spectra of CZT thin films grown at 300°C (as-grown) and annealed at 300°C and 450°C under N ₂ H ₂ ambient, respectively	38
Figure 4.5. XRD spectra of CZT thin films grown at 400°C (as-grown) and annealed at 300°C and 450°C under N ₂ ambient, respectively.....	39
Figure 4.6. XRD spectra of CZT thin films grown at 400°C (as-grown) and annealed at 300°C and 450°C under N ₂ H ₂ ambient, respectively	39
Figure 4.7. SEM image of CZT thin films as-grown at 200°C the sputtering temperature (a) 1 μm and (b) 5 μm respectively.....	45
Figure 4.8. SEM image of CZT thin films deposited at 200°C the sputtering temperature and annealed at 300°C, (a) 400 nm (b) 1 μm (c) 5 μm respectively.....	46
Figure 4.9. SEM image of CZT thin films deposited at 200°C the sputtering temperature and annealed at 450°C (a) 1 μm and (b) 5 μm respectively.....	46

Figure 4.10. SEM image of CZT thin films at 300°C (as-grown) (a) 500 nm, (b) 1 μm, and (c) 5 μm respectively	47
Figure 4.11. SEM image of CZT thin films deposited at 300°C the sputtering temperature and annealed at 300°C images (a) 1 μm, and (b) 5 μm respectively	47
Figure 4.12. SEM image of CZT thin films deposited at 300°C the sputtering temperature and annealed at 450°C images (a) 1 μm, and (b) 5 μm respectively	48
Figure 4.13. SEM image of CZT thin films as-grown at 400°C the sputtering temperature (a) 1 μm, and (b) 5 μm respectively	49
Figure 4.14. SEM image of CZT thin films as-grown at 400°C the sputtering temperature and annealed at 300°C (a) 500 nm, (b) 1 μm, and (c) 5 μm respectively	49
Figure 4.15. SEM image of CZT thin films at 400°C (as-grown) and annealed at 450°C images (a) 500 nm, (b) 1 μm, (c) 5 μm, and (d) 10 μm respectively	50
Figure 4.16. AFM images of CZT thin films as-grown on glass substrates (a) -3.6;+4.5 nm in two dimensions, (b) 1 μm * 1 μm in three dimensions	51
Figure 4.17. AFM images of CZT thin films as-grown on glass substrates (a) -3.3;+4.2 nm in two dimensions, (b) 0.5 μm * 0.5 μm in three dimensions	52
Figure 4.18. AFM images of CZT thin films deposited at 200°C (as grown) on glass (a) -12.2;+26.7 nm in two dimensions, (b) 1 μm * 1 μm in three dimensions	52
Figure 4.19. AFM images of CZT thin films deposited at 200°C (as grown) on glass (a) -19;+56 nm in two dimensions, (b) 5 μm * 5 μm in three dimensions	53
Figure 4.20. AFM images of CZT thin films deposited at 200°C (as grown) on glass (a) -8.8;+13.4 nm in two dimensions, (b) 0.50 μm * 0.50 μm in three dimensions	53
Figure 4.21. AFM images of CZT thin films deposited at 200°C and annealed at 300°C on glass (a) -34;+80 nm in two dimensions, (b) 1 μm * 1 μm in three dimensions	53
Figure 4.22. AFM images of CZT thin films deposited at 200°C and annealed at 300°C on glass (a) -25;+188 nm in two dimensions, (b) 5 μm * 5 μm in three dimensions	54
Figure 4.23. AFM images of CZT thin films deposited at 200°C and annealed at 300°C on glass (a) -18;+60 nm in two dimensions, (b) 0.50 μm * 0.50 μm in three dimensions	54
Figure 4.24. AFM images of CZT thin films deposited at 200°C and annealed at 450°C on glass (a) -41;+45 nm in two dimensions, (b) 1 μm * 1 μm in three dimensions	54
Figure 4.25. AFM images of CZT thin films deposited at 200°C and annealed at 450°C on glass (a) -42;+26 nm in two dimensions, (b) 0.50 μm * 0.50 μm in three dimensions	55
Figure 4.26. AFM images of CZT thin films deposited at 300°C (as grown) on glass (a) -19.1;+27.3 nm in two dimensions, (b) 1 μm * 1 μm in three dimensions	55

Figure 4.27. AFM images of CZT thin films deposited at 300°C (as grown) on glass (a) -15.6;+16.5 nm in two dimensions, (b) 0.50 μm * 0.50 μm in three dimensions	56
Figure 4.28. AFM images of CZT thin films deposited at 300°C and annealed at 300°C on glass (a) image -8.8;+11.7 nm in two dimensions, (b) image of sample with 1 μm * 1 μm in three dimensions	56
Figure 4.29. AFM images of CZT thin films deposited at 300°C and annealed at 300°C on glass (a) -11.3;+17.3 nm in two dimensions, (b) 5 μm * 5 μm in three dimensions	56
Figure 4.30. AFM images of CZT thin films deposited at 300°C and annealed at 300°C on glass (a) 8.4;+8.6 nm in two dimensions, (b) 0.50 μm * 0.50 μm in three dimensions	57
Figure 4.31. AFM images of CZT thin films deposited at 300°C and annealed at 450°C on glass (a) -9.5;+11.9 nm in two dimensions, (b) 1 μm * 1 μm in three dimensions	57
Figure 4.32. AFM images of CZT thin films deposited at silicon sputtering temperature of 300°C and annealed at 450°C on glass (a) -2.7;+4.4 nm in two dimensions, (b) 0.20 μm * 0.20 μm in three dimensions...	57
Figure 4.33. AFM images of CZT thin films deposited at 300°C and annealed at 450°C on glass (a) image -3.4;+13.4 nm in two dimensions, (b) image of sample with 0.50 μm * 0.50 μm in three dimensions	58
Figure 4.34. AFM images of CZT thin films deposited at 400°C (as grown) on glass (a) -13.1;+20.6 nm in two dimensions, (b) with 1 μm * 1 μm in three dimensions	58
Figure 4.35. AFM images of CZT thin films deposited at silicon sputtering temperature of 400°C and as grown on glass (a) image -16;+15.8 nm in two dimensions, (b) image of sample with 0.50 μm * 0.50 μm in three dimensions	59
Figure 4.36. AFM images of CZT thin films deposited at 400°C and annealed at 300°C on glass (a) -10.8;+9.1 nm in two dimensions, (b) 1 μm * 1 μm in three dimensions	59
Figure 4.37. AFM images of CZT thin films deposited at silicon sputtering temperature of 400°C and annealed at 300°C on glass (a) -9.8;+7.1 nm in two dimensions, (b) 0.50 μm * 0.50 μm in three dimensions...	59
Figure 4.38. AFM images of CZT thin films deposited at 400°C and annealed at 450°C on glass (a) -12.1;+13.3 nm in two dimensions, (b) 1 μm * 1 μm in three dimensions	60
Figure 4.39. AFM images of CZT thin films deposited at 400°C and annealed at 450°C on glass (a) -12.9;+20.8 nm in two dimensions, (b) 5 μm * 5 μm in three dimensions	60
Figure 4.40. AFM images of CZT thin films deposited at 400°C and annealed at 450°C on glass (a) -10.8;+11.1 nm in two dimensions, (b) 0.50 μm * 0.50 μm in three dimensions	61
Figure 4.41. EDX measurement of CZT thin films samples as grown	64
Figure 4.42. EDX spectra of CZT thin films grown at 200°C sputtering temperature (as grown)	64
Figure 4.43. EDX spectra of CZT thin films grown at 200°C sputtering temperature and under 300°C annealing temperature.....	65
Figure 4.44. EDX spectra of CZT thin films grown at 200°C sputtering temperature and under 450°C annealing temperature.....	65

Figure 4.45. EDX spectra of CZT thin films grown at 300°C sputtering temperature and under 0°C annealing temperature.....	66
Figure 4.46. EDX spectra of CZT thin films grown at 300°C sputtering temperature and under 300°C annealing temperature.....	66
Figure 4.47. EDX spectra of CZT thin films grown at 300°C sputtering temperature and under 450°C annealing temperature.....	67
Figure 4.48. EDX spectra of CZT thin films grown at 400°C sputtering temperature (as grown)	67
Figure 4.49. EDX spectra of CZT thin films grown at 400°C sputtering temperature and under 300°C annealing temperature.....	68
Figure 4.50. EDX spectra of CZT thin films with sputtering temperature 400°C and annealing temperature 450°C	68
Figure 4.51. XPS spectra of O1s level in the CZT film deposited on glass at 200°C and as grown for 25 spectra	71
Figure 4.52. XPS spectra of Te3d5 level in the CZT film deposited on glass at 200°C and as grown for 25 spectra	72
Figure 4.53. XPS spectra of Zn2p3 level in the CZT film deposited on glass at 200°C and as grown for 25 spectra	72
Figure 4.54. XPS spectra of Cd3d5 level in the CZT film deposited on glass at 200°C and as grown for 25 spectra	72
Figure 4.55. XPS spectra of O1s level in the CZT film deposited on glass at 200°C and annealed at 300°C for 25 spectra	73
Figure 4.56. XPS spectra of Te3d5 level in the CZT film deposited on glass at 200°C and annealed at 300°C for 25 spectra	73
Figure 4.57. XPS spectra of Zn2p3 level in the CZT film deposited on glass at 200°C and annealed at 300°C for 25 spectra	73
Figure 4.58. XPS spectra of Cd3d5 level in the CZT film deposited on glass at 200°C and annealed at 300°C for 25 spectra	74
Figure 4.59. XPS spectra of O1s level in the CZT film deposited on glass at 400°C and as grown for 25 spectra	75
Figure 4.60. XPS spectra of Te3d5 level in the CZT film deposited on glass at 400°C and as grown for 25 spectra	75
Figure 4.61. XPS spectra of Zn2p3 level in the CZT film deposited on glass at 400°C and as grown for 25 spectra	75
Figure 4.62. XPS spectra Cd3d5 level in the CZT film deposited on glass at 400°C and as grown for 25 spectra	76
Figure 4.63. XPS spectra of O1s level in the CZT film deposited on glass at 400°C and annealed at 300°C for 25 spectra	76
Figure 4.64. XPS spectra of Te3d5 level in the CZT film deposited on glass at 400°C and annealed at 300°C for 25 spectra	76
Figure 4.65. XPS spectra of Zn2p3 level in the CZT film deposited on glass at 400°C and annealed at 300°C for 25 spectra	77
Figure 4.66. XPS spectra of Cd3d5 level in the CZT film deposited on glass at 400°C and annealed at 300°C for 25 spectra	77
Figure 4.67. XPS spectra of O1s level in the CZT film deposited on glass at 400°C and annealed at 450°C	77
Figure 4.68. XPS spectra of Te3d5 level in the CZT film deposited on glass at 400°C and annealed at 450°C	78
Figure 4.69. XPS spectra of Zn2p3 level in the CZT film deposited on glass at 400°C and annealed at 450°C	78

Figure 4.70. XPS spectra of Cd3d5 level in the CZT film deposited on glass at 400°C and annealed at 450°C	78
Figure 4.71. Transmission spectra of CZT thin film grown at 200, 300, and 400°C under 200°C annealing temperature.....	80
Figure 4.72. Transmission spectra of CZT thin film grown at 200, 300, and 400°C under 300°C annealing temperature.....	80
Figure 4.73. Transmission spectra of CZT thin film grown at 200, 300, and 400°C under 450°C annealing temperature.....	81
Figure 4.74. UV spectroscopy band gap measurement of CZT thin film grown at 200, 300, and 400°C under as grown.....	82
Figure 4.75. UV spectroscopy band gap measurement of CZT thin film grown at 200, 300, and 400°C under 300°C annealing temperature.....	82
Figure 4.76. UV spectroscopy band gap measurement of CZT thin film grown at 200, 300, and 400°C under 450°C annealing temperature.....	83

LIST OF TABLES

	<u>Page</u>
Table 2.1. Crystal Systems.....	23
Table 4.1.a) XRD measurements CZT thin films and analysis the peaks with ICDD database then calculated the x value and E_g , by using different deposition and annealing temperature under N_2 gases.....	42
Table 4.1.b) This table is continuing of table 4.2.a.....	42
Table 4.2 FWHM values and grain sizes for CZT films deposited at various sputtering and annealing temperatures under N_2	43
Table 4.3 FWHM values and grain sizes for CZT films deposited at various sputtering and annealing temperatures under N_2H_2	44
Table 4.4. Some parameters of CZT films deposited at various sputtering temperatures.....	62
Table 4.5. Atomic percentage (% value) of Cd; Zn; Te; in the compound found from EDX.....	69
Table 4.6. x value calculation is made according to EDX measurements from the atomic weight of Cd and Zn.....	69
Table 4.7. CZT thin films band gap values calculated annealing under N_2 ambient.....	84
Table 4.8. x values from all measurements.....	84

LIST OF ABBREVIATIONS AND SYMBOLS

A	: The absorbance
a	: The lattice constant
a_x	: The Lattice constant of CdZnTe [= $a(\text{Cd}_{1-x}\text{Zn}_x\text{Te})$]
a_{CdTe}	: The Lattice constant of CdTe
a_{ZnTe}	: The Lattice constant of ZnTe
AES	: Auger Electron Microscopy
AFM	: Atomic Force Microscopy
APCVD	: Atmosphere-Pressure Chemical Vapor Deposition
CZT	: $\text{Cd}_{1-x}\text{Zn}_x\text{Te}$ or CdZnTe
CVD	: Chemical Vapor Deposition
DC	: Direct Current
t	: Thicknes of the specimen
d_{hkl}	: The inter-planar spacing between crystallographic planes
EDS	: Energy Dispersive Spectroscopy
E_g	: Optical Band Gap
EPR	: Electron Paramagnetic Resonance
ESR	: Electron Spin Resonance
FWHM	: Full width at half maximum
I	: Transmitted light intensity
I_o	: Incident light intensity
ICDD	: The International Centre for Diffraction Data
LPCVD	: Low-Pressure Chemical Vapor Deposition
MOCVD	: Metal-Organic Chemical Vapor Deposition
n	: The order of diffracted beam
P	: The average grain size of the fabricated films
P_γ	: The possibility of emission for the took into account energy
PVD	: Physical vapor deposition
PECVD	: Plasma-Enhanced Chemical Vapor Deposition
R	: Reflection
RF	: Radio Frequency
RMS	: Root Mean Square

SSIMS	: Static Secondary Ion Mass Spectrometry (or Surface- SIMS)
SPM	: Scanning Probe Microscopy
SEM	: Scanning Electron Microscopy
TEM	: Transmission Electron Microscopy
T_s	: Sputtering temperature
T	: Transmittance
UV	: Ultraviolet
<i>x</i>	: Zinc concentration
XPS	: X-ray Photoelecctron Spectroscopy
XRD	: X-ray Diffraction
W_M	: Work function of metal
W_S	: Work function of silicon
Z	: Atomic number
β	: The FWHM of the peak corresponding to (<i>hkl</i>) plane
α	: The adsorption coefficient
λ	: Wavelength of the incident X-ray
θ	: Bragg's angle

ACKNOWLEDGEMENTS

The author wishes to express his deepest gratitude to his supervisor Prof. Dr. Ercan YILMAZ for their guidance, advice, criticism, encouragements and insight throughout the research.

The author would also like to thank to Assist. Prof. Dr. Aliekber AKTAĞ for his help and critical reading of the thesis. The author is grateful to them for valuable suggestions in correcting my errors.

My gratitude is extended to Prof. Dr. Çetin BOZKURT for their invaluable criticisms and feedback throughout the study.

The author also likes to express my appreciation to the other members of my Committee, Prof. Dr. Raşit TURAN and Prof. Dr. Atilla KILIÇ for their comments and assistance.

The author thankful to his friend Şenol Kaya for his help, sincerity, hospitality, and friendship.

Finally the author offers his special thanks to each member of his family without their encouragements and support this thesis would not have been possible.

The author wishes to thank Middle East Technical University for their generous support. This work is supported by Abant Izzet Baysal University under contract number: AIUB-BAP.2009.03.319, Ministry of Development of Turkey under contract number 2012K120360, and TUBITAK (Scientific and Technological Research Council of Turkey) Project no. 114F066.

1. INTRODUCTION

Investigation of semiconductor materials and their properties are of interest from both technological and scientific viewpoint. Semiconductor materials research started in 1950s mostly on Si and Ge and the basic structural, electrical and optical properties of these semiconductors were described. Semiconductor materials research then expanded to the semiconducting binary and ternary compound materials of III-V and II-VI group elements such as GaAs, CdTe, ZnTe and CZT.

In recent years, considerable work has been committed to develop a range of compound semiconductors for use as photon and charged particle detectors. In this study we explored and investigated one of the CdTe/ZnTe-based semiconducting compound materials: $\text{Cd}_{1-x}\text{Zn}_x\text{Te}$ (CZT) where x is the amount of Zn concentration. Because of their structural and optical properties CdTe and ZnTe are common II-VI semiconductors widely used in current technologies. When compared to other widespread semiconductors, CdTe/ZnTe based materials have advantages of high-energetic photons absorption efficiency due to high atomic number Z and wide band gap allowing the fabrication of highly resistive materials enabling the usage of detectors at room temperature, for instant, undoped CdTe is used for detection of X-ray and gamma-ray radiation and is also used in the solar cells manufacturing. Since CdTe and ZnTe have largest electro-optic coefficients of the linear electro-optic effect among II-VI compound crystals they became attractive choices for epitaxial growth of CZT as a detector for high energetic photons. Currently, CZT showed an increased interest to be used in applications which require high resolution and spectroscopic imaging in medical, security and nuclear research industry. Understanding and the knowledge of CZT material is important because it will provide how it may be applied to modify the structure and thereby tune the resulting properties of the material.

Cadmium based ternary II-VI compounds have been studied extensively over the last decade because of their interesting optical and electrical properties. These types of compounds are regarded as the ternary analogues of the II-VI binary semiconductors. II-VI materials have a cubic, zinc-blende type lattice. Compound semiconductors such as CdTe, ZnTe, and CZT are potential candidates for

photovoltaic applications (Ringel et al., 1990a-b); infrared, X-ray and gamma ray detectors (Enderlein and Horing, 1997; Butler J. F., et al., 1992; Niemela and Sipila, 1994). Adjusting the band gap energies ranging from 1.5 eV to 2.25 eV make these compounds promising candidates for light emitting devices and detectors in large wavelength range varying from ultraviolet to infrared. Their band gap energies are continuously changed by varying the composition of CZT (Zelaya-Angel et al., 2004; Prabakar et al., 2004a). These compounds can be successfully used in the generation of polycrystalline thin film tandem solar cells. For a high efficiency of such devices, the band gap of the top cell should be in the range of 1.5 – 1.8 eV (Coutts et al., 2002). CZT compounds are suitable for this aim due to their band gap.

Among the Cd based materials the most widely studied one is the CZT, particularly convenient for the construction of high-efficient thin film solar cells due to having a high absorption coefficient. It is also convenient for optic band gap for solar cell spectrum and producible by a number of deposition techniques easily (Basol et al, 2000). Different methods have been used to produce CZT films: molecular beam epitaxy (Dinan and Qadri, 1985), liquid phase epitaxy (Pellicary et al., 1988), electro deposition (Basol et al., 1989), close space vapor transport (Gonzales-Hernandes et al., 1991), laser ablation (Aydinly, 1991), thermal vapor (Kim et al., 2004); Phabakar, 2004b); (Rusu, 2006 ; Rusu et al., 2007), metal–organic chemical vapor deposition (MOCVD) (Chu, 1992) and sputtering (Becerril, 2004). The final method has been considered as a flexible process, suitable for the fabrication of both multilayer solar cells and photo detectors. As it is known, there are many papers empirically studied a wide range of compositions of CZT films on glass, but these films were produced by using a few sputtering targets, such as CdTe target and Zn powders or CdTe and ZnTe targets (Sharma et al., 2000). Hence, investigating the structure and structural stability of single target sputtered $Cd_{1-x}Zn_xTe$ films on glass for the entire range of $0 < x < 1$ needs an important scientific interest. Producing CZT alloy with the required lattice parameters is a challenge. These lattice parameters depend on Zn concentration in the compound. CZT may be deposited by Sputtering, Molecular Beam Epitaxial, etc. for solar cell applications (Rohatgi et al., 1991).

CZT has also several properties that make it highly requested for desire applications such as spectroscopy. Its high detection efficiency, high resolution, low cost, and good signal to noise ratio at room temperature make it a product of choice

for many applications. The most important parameter to make radiation detector is the band gap. The wide band gap of CZT has the following characteristics: high band gap energy, high atomic number, good mechanical strength, high resistivity, photosensitivity, and relatively good charge transport properties (Schlesinger et al., 2001; Fiederle et al., 1999; Neumark, 1997). Band gap depends on the Zn concentration in the compound. The band gap changes only a few meV by varying zinc concentration with a few percentages which is significant for idea of the most detector related parameters. Generally the ratio of Zn with respect to Cd in a typical CZT body is less than 10% (Ahmed, 283:2007).

The energy gap of CZT increases with the x value, which makes it harder to produce an electron–hole pair. Hence, the free-carrier concentration of the CZT will diminish with the x value. Thus the intrinsic resistivity of CZT crystal increases monotonously with the x value (Fiederle et al., 1999). However, the higher x value will increase the melting point of CZT. For the growth of CZT crystal with the x value less than 0.20 from the melt, means higher Cd pressure, which will influence the qualities of the CZT crystal (Greenberg, 1999; Vydyanath et al., 1993).

The structural, elastic, electronic and optical properties of CZT mixed crystals have been reported for the present solids which are extremely significant because these perform important roles in determining some material specialties such as interatomic forces, phase transition, transport coefficients and electron–photon interactions. Also, the electronic structure and optical particularities of Cd based compounds are significant for guiding the successful design and fabrication of optoelectronic devices (Polit et al, 2004).

CdTe and CZT have drawn on increasing concerns in the improvement of X-ray and γ -ray detectors (James, and Siffert 2001; Philips, 2006). High detection efficiency, good room temperature performance because of the high atomic number, the high density and the large band gap are guaranteed by CdTe and CZT detectors and are very attractive for X-ray and γ -ray applications. Adversities in manufacturing detector-grade substances and in augmenting chemically pure and structurally excellent crystals are the critical problems of CdTe and CZT detectors. Actually, the great potential of these composites has not been used for many decades owing primarily to the confined trading presence of high-quality crystals (Del Sordo et al., 2009).

$\text{Cd}_{1-x}\text{Zn}_x\text{Te}$ crystals have attracted renovated attention as the most promising material for room-temperature high-performance nuclear detectors (Schlesinger and James, 1995; Schlesinger et al., 2001). The performance of the detectors is strongly contingent on the quality of the CZT crystal. Nevertheless, the growth of high-quality CZT is very hard due to concentration heterogeneity and the native defects during crystallization, which make the as grown crystals inadaptable for pixelized detectors (Li et al., 2004; Chu et al., 2001; Fu et al., 2002). CZT has significant industrial applications such as solar cell, photo detectors, X-ray detector, gamma ray detectors and optoelectronic devices (Butler et al., 1993; Schlesinger et al., 2001). CZT thin film has appropriate band gap to be used in solar cell technology because it has adjustable bandgap from 1.5 to 2.25 eV (Derbin et al., 2001). The matter searched by many recent papers has been focused on the optical properties of amorphous semiconductors. The optical amorphous of semiconductors depends exceedingly on the composition of the compound (Mott, and Davis, 1979; Lecomber, and Mort 1973). The optical properties of substances are connected to their electronic band structure, atomic and electrical structure.

Butler et al. (1993) developed the high x value in CZT crystal for the first time in 1993. Kim et al. (2004) have been investigated electrical and optical properties of polycrystalline CZT thick films grown by thermal evaporation method. The electrical properties of polycrystalline CZT having high resistivity were investigated. They have measured the average drift mobility and mobility lifetime of polycrystalline CZT have been measured. In the comparison of annealed samples at different conditions, the variation of resistivity in the polycrystalline CZT is considered to be related to the fluctuation of carrier concentration.

CZT X-ray and gamma ray detectors have a lot of advantages than the other detectors. Başol et al. (1989) have equipped CZT film by annealing the accumulated elemental layers of Cd, Te and Zn. The exploiting bindings of Electrodeposition and thermal evaporation deposited elemental layers followed by annealing. The figuration of CZT compound was appeared a shift in (111) reflection and linear variation of the lattice parameter with composition (Bruder et al., 1990). Dhare et al. (2003) obtained that when deposited by sublimation from a mixed powder source, it is very difficult to hold much Zn in the film. Thin films of CZT's have been deposited from hydrous solution on substrate by Bansal and Rajarman et al. (Bansal, and Rajaram 2005). Conversely, the deviation of Zn and Te ions is less soluble in

hydrous medium can cause difficulty in controlling the stoichiometry of semiconductor thin films. Chaure et al. (2004) are reported CZT's application electrodeposited using non hydrous bath photovoltaic application.

The CZT thin films with blende type structure has many applications owing of its several properties; for example, the tunability of band gap and lattice parameter with alloy composition, high amount of optical transmittance below the band gap and high optical absorption coefficient above the bandgap. Many scientists have interested these properties of CZT ternary semiconductor material (Chu, 1986; Goela, and Taylor, 1987; Chattopadhyaya et al., 1991; Reno, and Jones, 1992; Rajavel, and Zinck, 1993; Samantha et al., 1994).

In the present study, an attempt was made to see the effect of RF Sputtering temperature and post annealing temperature on determining the microstructural, morphological and optical properties of CZT thin films for different Zn concentrations. Many scientists have testified the improvement of semi-insulating CdTe and CZT after more than 40 years of laboratory exploration. They reported that semiconductor detector technology has many applications at room temperature such as especially industrial monitoring, medical and industrial imaging, calibration, nuclear safeguards, transportation safety and security.

CZT thin films were deposited by RF sputtering technique. Thin films were produced onto the glass substrates from the single CZT target. Following the deposition of films, the effect of annealing between 300 - 450 °C on microstructural, morphological, and optical properties have been investigated.

This thesis consists of five chapters. In first chapter, CdTe/ZnTe and CZT material properties for semiconductor detectors have been introduced. In chapter two, the theoretical background, deposition techniques, structure and characterization techniques for CZT thin films have been presented. In chapter three, the experimental techniques; X-ray diffraction (XRD), Energy Dispersive X-ray (EDX), X-ray photoelectron spectroscopy (XPS), Scanning Electron Microscopy (SEM), and Atomic Force Microscopy (AFM) and detailed explanation of measurements, main stages of characterization of CZT thin films using RF magnetron sputtering techniques for deposition have been given. Chapter four deals with the results and discussions for the deposited films as a consequence of conducted several type of microstructural, morphological and optical characterization measurements. And

finally, in chapter five, the important results obtained for these materials have been underlined.

2. THEORETICAL CONSIDERATIONS

2.1 Introduction

In this chapter, the theoretical basis behind the thin films growth by sputtering technique and microstructural, morphological, and optical characterizations are introduced in details.

2.2 Semiconductor Materials

A group of materials having conductivities are called semiconductors which are between those of metals and insulators. They have two common classifications. These are: 1) The elemental semiconductor materials found in group IV of the periodic table, and 2) the compound semiconductor materials, most of which are formed from special combinations of group III and group V elements. Semiconductors can also be formed from combinations of group II and group VI elements.

The elemental materials are silicon and germanium. They are composed of single species of atoms. Silicon is the most general semiconductor used in integrated circuits. The two-element, or binary compounds such as gallium arsenide or gallium phosphide are formed by combining one group III and one group V element. Gallium arsenide is one of the more common of the compound semiconductors. A three-element (ternary) compound semiconductor is formed a group of III-V elements or II-VI elements such as $\text{Al}_x\text{Ga}_{1-x}\text{As}$ or $\text{Cd}_{1-x}\text{Zn}_x\text{Te}$ (Neamen, 2003).

2.2.1 Structure of II-VI Materials

II-VI semiconductors such as CdTe and ZnTe are comprised of two types of atoms, with each atom being tetragonally bonded to 4 other atoms of the opposite type. The each component atoms are bonded covalently, with some ionic character because of the two types of atoms differing in charge (e. g. Cd^{+2} and Te^{-2}) (Ray B.. 1969). This forms the basis of two crystal structures: zinc blende and wurtzite. These structures have very different symmetries, with zinc blende having a cubic crystal structure, and wurtzite having a hexagonal crystal structure.

The zinc blende crystal structure consists of two inter-penetrating face-centered cubic lattices, with one lattice being composed of the positive ions, and the other composed of the negative ions (Fig. 2.1) (Ray, 1969; Ashcroft and Mermin, 1976). The interatomic distance between adjacent atoms is $\frac{\sqrt{3}}{4}a$, where a is the lattice constant. The lattice constant for bulk CdTe is $a=6.48 \text{ \AA}$, and for ZnTe is $a=6.10 \text{ \AA}$.

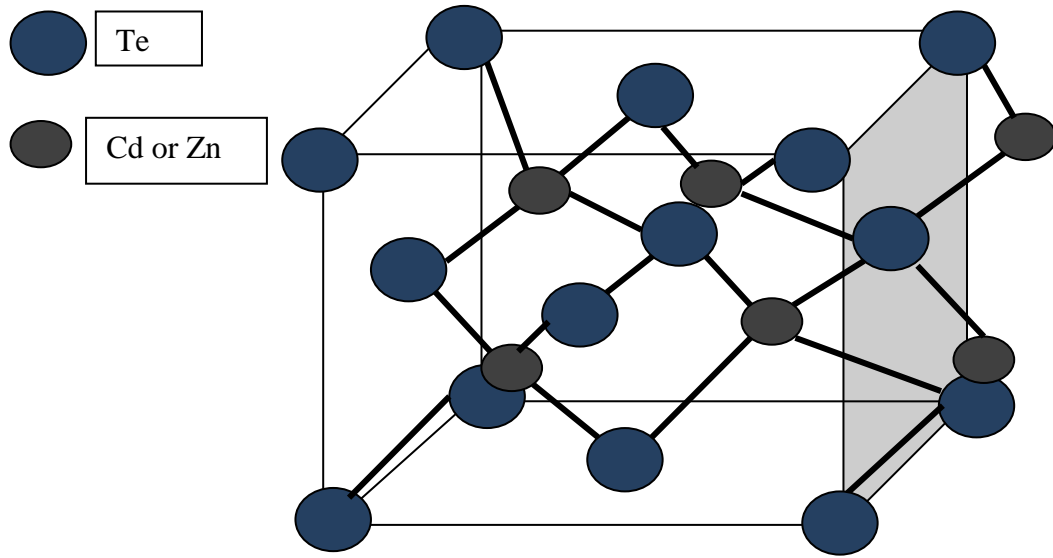


Figure 2.1. Zinc blende crystal structure of CdTe and ZnTe.

The epitaxial growth of CdTe/ZnTe heterostructures (alternating layers of these materials grown on top of each other) will ideally maintain the same crystallographic orientation and lattice structure across the interface so that the boundary does not produce defects that might unexpectedly change the properties of the material. The different materials meet results in a localized strain in interface due to the lattice mismatch between CdTe and ZnTe. For CdTe and ZnTe, the lattice mismatch is 6.2%. This shifts the lattice constant of both materials in an attempt to minimize the interfacial energy. The amount of the shift depends on how much material is on either side of the interface, and how easily these materials tend to deform (Van de Walle, 1989). Since CdTe has a larger lattice constant than that of ZnTe, the structure of CdTe at the interface will be compacted, and ZnTe will be stretched.

CZT crystals possess a building block of two interpenetrating face center cubic (FCC) sub-lattices. The FCC sublattices are apart by one-quarter of a unit cell body diagonal. Cd or Zn nuclei occupy one sub-lattice while Te occupies the other. These lattice nuclei arrangements result in a zinc blende (Zinc Sulfide) crystal

structure (Rudolph, 2003). Cadmium Zinc Telluride atoms are primarily held together by covalent bonds, as are zinc blende structured semiconductors, hence valence band electrons are shared. CZT crystal structure is shown Figure 2.2.

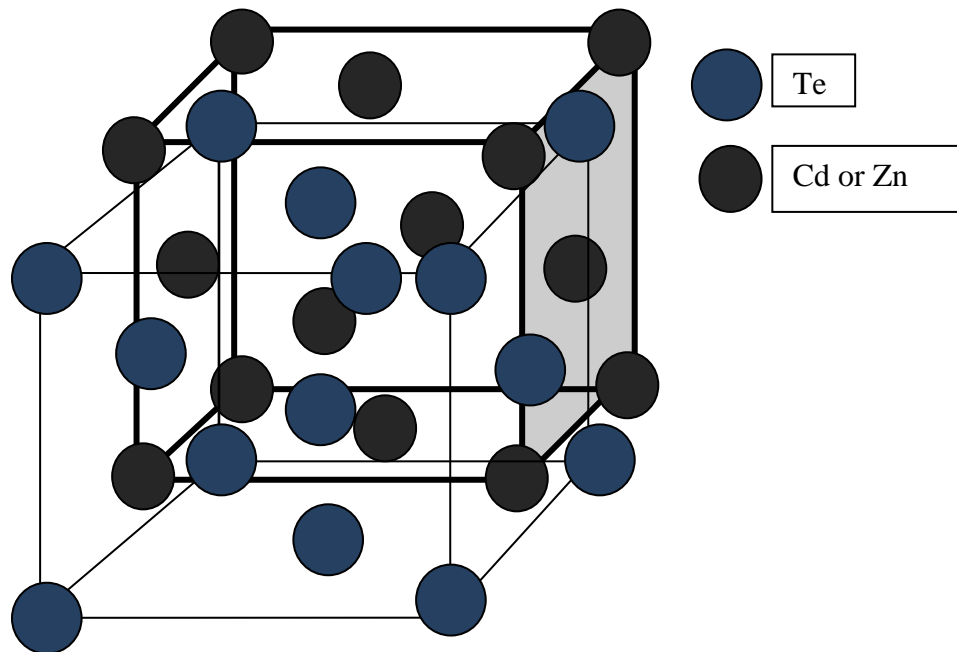


Figure 2.2. Zinc blende crystal structure of CZT.

2.2.2 Band Structure of Semiconductors

It is known from Quantum Physics that electrons in an atom can occupy only discrete energy levels. In fact, this discreteness or quantization is not in any way limited to isolated atoms. For example the covalent bonding between atoms in semiconductors creates allowed discrete energy levels. However these energy levels are lumped together in the so called two bands: valence band and transmission band. Valence band represents a large number of very closely spaced energy levels at lower energies as compared to the transmission band, which contains levels at higher energies. A forbidden gap segregates these two bands: a region in the energy level diagram containing no energy levels. This essentially means that electrons cannot assume any energy that lies in this band. We'll later see that this holds for only ideal semiconductors with no impurities and any practical semiconductor does have at least one energy level in the band gap.

The electrons in the valence band are tightly bound to the atoms and need at least an energy equivalent to the band gap to act to the transmission band. The

transmission band electrons, on the other hand, are very loosely bound and are almost free to move around. These electrons take part in the electrical transmission procedure. In an ideally pure semiconductor, in the ground state, all the electrons would populate the valence band while transmission band would be empty.

Actually this band structure is not typical of just semiconductors. Insulators and conductors also have similar structures. The distinguishing feature between them is the band gap, since it represents the energy barrier that must be overcome by bound electrons to become free and take part in the electrical transmission procedure. Fig. 2.3 compares the three types of solids in terms of energy level diagram. The band gap in insulator and conductors are exactly opposite to each other, being very large for insulators and non-existent for metallic. Semiconductors, on the other hand, have a small band gap, so small that even a small thermal excitation can provide enough energy to electrons in the valence band to leap up to the transmission band.

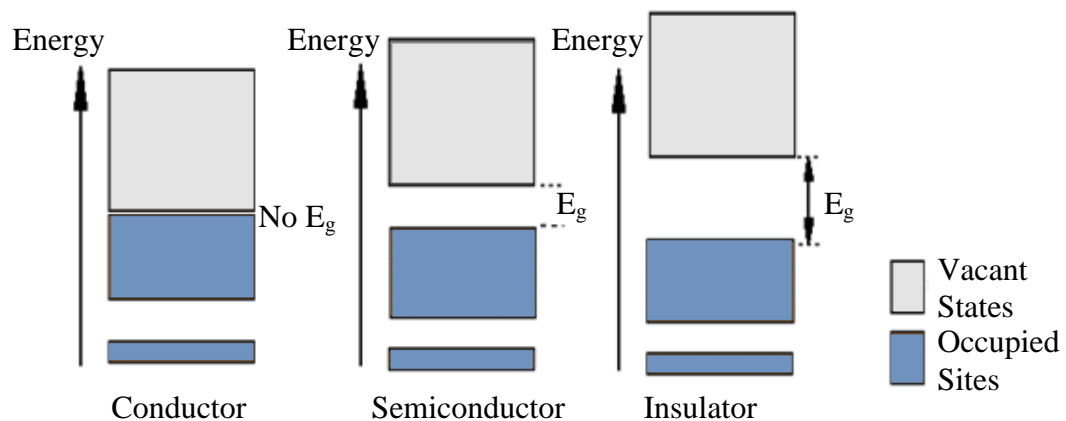


Figure 2.3. The energy band structure diagrams for insulators, semiconductors, and conductors (Ahmed, 2007).

When an electron jumps from the valence band to the transmission band, it leaves a net positive charge behind. This effective positive charge, called a hole, behaves like a real particle and takes part in electrical conduction process. However it should be noted that by movement of a hole we mean the shift of a net positive charge from one site to another due to the movement of an electron. A hole should not be considered a localized positive charge having defined mass (Ahmed, 2007).

2.3 Semiconductor Detectors

In spite of McKay of Bell Laboratories had shown the detection of α particle by semiconductor diodes few years earlier semiconductor detectors came in sight on the setting of Nuclear Physics in about 1960.

Semiconductors incline to be used in applications with the most requiring energy-resolution demands as a branch of radiation-detection substances since they introduce more condensed forms and better energy resolution for γ -ray spectrometry (Venkataraman, and Croft, 2003). The combination of measurements with high readout speed, the direct obtainability of signals in electronic form, the contemporaneous exact measurement of energy, position and their probability of integrating detectors and readout electronics on a general substrate are some of the attainable avails.

Silicon or germanium substances cause perfect energy resolution, however low stopping power for high energy photons characterizes Si, while small band-gap of Ge, it can work only low temperature. Compound semiconductors like GaAs, CdTe, CZT and HgI₂ have been studied with goal of noticing high efficiency detectors (Bertuccio, 2005; Rizzi et al., 2005; Rizzi et al, 2006).

2.4 CdTe and CZT Detectors

CdTe and CZT are commonly derived from elements in groups II to VI of the periodic table. They are so helpful, compared to the elemental semiconductors, Sn-a, carbon, silisyum and germanyum. Most elements in these groups are solvable inside each other, shaping homogeneous solid solutions. These solutions happen when atoms of a special element can substitute a given constituent of a different material at without changing its crystal structure (Owens, and Peacock 2004).

In the 1990's, the notable development in the technique of manufacturing a high quality single crystal of CdTe and the appearance of Cadmium Zinc Telluride (CZT) have dramatically altered the states of high resolution room temperature detectors (Eisen, 1974). CZT ternary semiconductors have been used in wide applications such as in solar cells, Electro optical modulators, X-ray detectors and γ -ray detectors, and other optoelectronic devices. In compound semiconductors, CdTe and CZT are the most hopeful substances for radiation detectors with good energy resolution, high detection efficiency and room temperature procedure

(Schieber, 2000; Iwanzyk et al., 1996; Bencivelli, 1991). These detectors have high resistivity owing to the extensive band gap and also have high photon adsorption efficient since the large atomic number. Nevertheless, electron-hole pairs produced in CdTe and CZT detectors by irradiating with gamma rays are not able to be fully gathered because of the low transport features of carriers. This causes an important deformity of the spectrum. The mobility-lifetime ($\mu\tau$) product of the carriers is parameter utilized in order to define the characters of CdZnTe and CdTe semiconductor detectors (Fourgeres et al., 1999). The mobility can be defined as the rise time of the amplifier when α -rays irradiate the detector. This technique is simple but the surface condition of the detector can be influenced the gotten values, since the mean free path of α -ray in CdTe/CZT is approximately 10 μm (Sato et al., 2001).

CdTe and CZT have attracted interests in the improvement of X-ray and γ -ray detectors (James, and Siffert 2001; Philips, 2006). Producing detector-grade materials and growing chemically pure and structurally excellent crystals are difficult due to the critical problems of CdTe and CZT detectors. Actually, the great potential of these composites has not been used for many decades owing primarily to the confined trading presence of high-quality crystals (Del Sordo et al., 2009).

2.5 Thin Film Growth Techniques

Thin film technology is performing a significant role in evolution of many industries which are microelectronics, optoelectronics, and telecommunication. The microelectronic is still the major thin film science exploited area. But, the applications in other fields such as optical and magnetic devices, electrochemistry, and coating for decoration, solar energy, and data-storage are also developing very quickly. Commonly one of them describes thin films as a liquid or solid linear dimension of which is very small than the other two dimensions (Wagendristel, and Wang, 1994). Thin films have been interest mostly because of their quite difference properties with respect to corresponding bulk material. That is, the bulk material is quite different than thin film due to properties of the same material in the thin film and bulk form. The thickness of layers in thin film can be varied between nanometer and several micrometers depending on the application. Thin films are grown onto a substrate or previously deposited layers to find the properties not achievable by

substrate itself. The features of films are closely related to the thickness and conditions under which they were grown and deposition technique.

Production of a thin film is composed of a few basic stages. The initial stage is the assignment of the substrate onto which the film will be deposited. The following stage is the deposition of material onto the substrate from liquid, vapour or solution.

And, the last stage is the creation of structure of the deposited film depending on the constructed bonds with the deposited material and substrate surface. Attributed these considerations, a few type of thin film growth models have been developed. These are island growth (Volmer, and Weber 1926), layer growth (Frank, and Van der Merwe 1949), and layer + islands (Stranski, and Krastanov 1938) models.

Different methods can be employed for the production of thin films, which are usually categorized under the following headings:

1. Physical vapor deposition (PVD)
 - Evaporation
 - Thermal evaporation
 - Electron-beam evaporation
 - Sputtering
 - Direct current (DC) sputtering
 - DC magnetron sputtering
 - Radio frequency (RF) sputtering
2. Chemical vapor deposition (CVD)
 - Low-pressure CVD (LPCVD)
 - Plasma-Enhanced CVD (PECVD)
 - Atmosphere-pressure CVD (APCVD)
 - Metal-organic CVD (MOCVD)

MOCVD is also known as chemical vapor deposition (CVD), is a chemical process used to produce high-purity, high performance solid materials. The process is often used in the semiconductor industry for producing thin films. CVD process includes a heated substrate onto which a solid material deposited by means of chemical reaction in gas phase. One or more volatile precursors subordinate to the substrate. Often, researcher generated volatile products, which are removed by gas

flow through the reaction chamber. Micro production processes broadly use CVD to deposit materials in different forms, involving monocrystalline, polycrystalline, amorphous, and epitaxial. These materials involve silicon, carbon fiber, filaments, carbon nanotubes, SiO₂, silicon germanium, tungsten, silicon carbide, silicon nitride, silicon oxynitride, titanium nitride, and various high-k dielectrics. The CVD process is also used to produce synthetic diamonds (Schropp et al., 2007).

The PVD methods are offered much more flexibility due to in terms of the material to be deposited and the substrate to be used with respect to CVD techniques. A general process is involved by all PVD methods. This process is the ejection of source particle into vacuum by a number of physical processes that assign the name of method (Moshfegh et al. 2004). The deposition process by PVD techniques involves three major steps (Wagendristel A., and Wang Y., 1994): 1) Taking out of particles from source to be deposited, 2) Transport of taken out species to the substrate, and 3) Accumulation of species on the surface of substrate. The all process is occurring in a vacuum atmosphere to permit the particle journey to the substrate without scattering and reacting with medium particles from source to target as much as probable. The source is placed in a crucible (boat) which is heated with a passing through current a resistive wire wrapped around it.

The thermal evaporation is one of all the known PVD techniques. This technique has the largest background and history. A large number of materials are deposited since it is a quite simple and powerful technique (Moshfegh et al. 2004). Also thermal evaporation is quite simple and cheap than other PVD methods. However, thermal method has not advantages such as accessibility and control of growth rate, ability in deposition of materials with high melting point, high possibility of reaction between the heated crucible and contained source material (contamination), and very poor density and weak hardness in deposited films.

The electron-beam another technique is largely used for evaporation. There is a boat containing source material which is heated by bombarding with high energetic electrons produced by an electron gun. This evaporation method possess three basic growth steps: 1) Heating of filament of electron gun until the electron is taken out, 2) Focusing and directing the produced electron beam to the crucible containing the source material to be deposited by magnetic deflection, and 3) Acceleration of electrons to different energies on the crucible for the evaporation of source material.

Different from thermal evaporation, electron-beam evaporation has some advantages such as the growing high-pure material, evaporation of materials with high melting point, allowing a good control over the growth rate (particularly it is important for the deposition of compounds), and better uniformity in thickness of the deposited films.

The sputtering is a method by which the material is taken out from a surface when high energetic atoms or ions hit (Maissel, and Francombe, 1973). A momentum transfer from the bombarding particles accomplishes the break off the material from the target. A vacuum chamber, a target (cathode) and substrate holder (anode) make up a typical sputtering system which has main stages in a typical sputtering deposition. These are:

- ❖ The applied voltage to the target and substrate accelerates free electrons in chamber.
- ❖ Accelerated free electrons interact with inert gas offered to chamber in elastically and ionize them and create plasma.
- ❖ Produced ions are accelerated and directed to the target material to be deposited.
- ❖ Bombarding the target results in knocking out atoms and transporting them to the substrate as a result of formed low pressure region near substrate.
- ❖ And finally a thin film is growth by the concentration of sputtered atoms on the substrate.

Sputtering yield, which measures the number of atoms knocked out from the target material per incident ion, is the most significant parameter in sputtering deposition method owing to its important role on defining deposition rate.

The deposition of conductors can only performed by DC sputtering. A quick building up of a positive charge is resulted by the incident ion bombardment on target surface. This surface obstructs the impingement of more ions to target. The deposition of nonconductive materials would not take place at these conditions

RF sputtering can be applied for the deposition of insulating. The ions bombards periodically the target in RF sputtering and in a full period cycle of pulse the charge built up on the target is made neutral. The ion bombardment on target surface is depending on frequency of applied RF power. It is probable to deposit different dielectric materials, especially oxides and nitrides by using RF sputtering. RF sputtering of dielectric targets has the basic disadvantage due to poor thermal

conductivity of these materials which are commonly friable. So, bombarding target with high energetic ions creates a heat that produces a large thermal gradient, which results in fracturing the target when sputtered at high power levels (Mattox, 1998).

Magnetron sputtering is another method improved to augment the efficiency of a sputter system by means of the created magnetic field by a permanent magnet which confines the plasma near the target and therefore augments the number of ions for the bombarding the target. In magnetron sputtering, a parallel magnetic field applied to the cathode surface causes electrons close to the target surface to support plasma. This give rise to increase in current density and subsequently sputtering rate (Moshfegh, 2004). The magnetron sputtering technique has basic advantage which is quite intense plasma. This plasma can be produced close to the target at low pressures that accredit ions to accelerate from the plasma to target without loss of energy in connection with inelastic interplays such as charge exchange collisions. This performs it probable to achieve high sputtering rates without applying wide potentials on the target, which is the case for the DC sputtering (Mattox, 1998). The magnetron sputtering technique has disadvantage: plasma is not uniform over the surface of target. So, the patterns formed by magnetron sputtering are not depended on the position of samples relative to target.

If sputtering deposition method compares with other PVD methods, sputtering introduces some advantages such as the ease at deposition of materials having even the highest melting point, a better adherence of films to substrate, a good control on thickness of deposited films, and control of the alloy composition.

2.6 Material Characterization Techniques

2.6.1 Surface Analysis Methods

Scientists obtained knowledge about surface properties of solid state materials with surface analysis techniques. Materials are interacted with their environment by means of their surfaces is obligatory for the improvement of semiconductor technology (Watts, and Wolstenholme, 2003). The surface features are investigated by sensitive characterization techniques such as SEM, TEM (Transmission Electron Microscopy), EDXA, SPM (Scanning Probe Microscopy), AES (Auger Electron Microscopy), XRD, AFM, XPS, Image Analysis, Optical Light

Microscopy, Nano-Materials Analysis and Research, Cryo EM Microscopy, SSIMS Static Secondary Ion Mass Spectrometry (Surface- SIMS), and Vertical Scanning, Phase Shifting Interferometer. By using these devices beneficial information about the surface states, surface composition, thin film microstructure, and morphology can be obtained.

2.6.1.1 X-ray Photoelectron Spectroscopy (XPS)

X-ray photoelectron spectroscopy is known also as electron spectroscopy for chemical analysis (ESCA). XPS was improved by K. Siegbahn and his groups in the mid-1960s. The Nobel Prize was won with this work for Physics in 1981. The phenomenon was constructed on the photoelectric effect which briefed by Einstein in 1905. The notion of the photon was used to identify removing of electrons from a surface when the photons collide upon it (Peter et al., 1996). A schematic illustration of XPS system is shown in Figure 2.4.

The knowledge about the elements available, their chemical state and their distribution is involved by XPS spectrum of a sample. Whole of these parameters can be obtained from a spectrum basically but the certainty of quantification trusts widely to the process of spectral analysis. The spectrum has to be unstitched in its components before quantification if peaks originating from types in a sample add on. The usual proceeding contains subtraction of a Shirley-type background from the whole spectrum and posterior fitting of the resulting background corrected spectrum with a set of peaks (Sykes D., 2013).

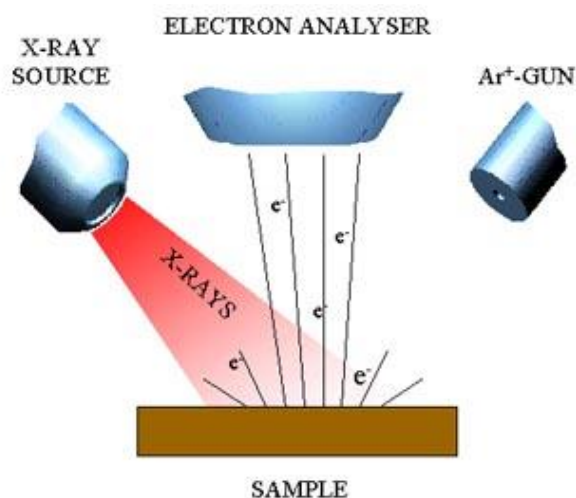


Figure 2.4. Schematic diagram of XPS method.

XPS is a surface sensitive process, a depth profile of the sample in terms of XPS quantities can be obtained by combining a sequence of ion gun etch cycles. The cycles are interleaved with XPS measurements from the current surface. An ion gun is used to etch the material for a period of time before being shut off whilst XPS spectra are obtained. A novel surface is exposed by each ion gun etch cycle and the means of analyzing the composition of these surfaces is provided by the XPS spectra.

2.6.1.2 Energy Dispersive Spectroscopy (EDS-EDX)

EDS or EDX is an analytical technique used for the elemental analysis or chemical characterization of a sample for regions as small as 0.1 μm at low voltage, even smaller for elements of high atomic number. The depth of analysis also can be as little as 0.1 μm or, again, much less for elements of high atomic number. The beam voltage and the sample composition are functions for these two parameters. A beam of electrons bombards the sample in this process.

EDS can detect all elements from atomic number 4 (Be) to 92 (U), although not all instruments are equipped for 'light' elements ($Z < 10$). The identification of the lines in the spectrum is involved by qualitative analysis (determination of the concentrations of the elements offered). This analysis is exactly straightforward due to the simplicity of X-ray spectra. The measuring line intensities are entailed by qualitative analysis for each element in the sample and for the same elements in calibration Standards of known composition (Russ, J. C., 1984; Goldstein J. I., et al. 2003; Reimer L., 1985).

A high radiation ionizes X rays; characteristic X rays are emitted by the atoms in a material. The elements in an EDX unit are the basis of high energy radiation, a solid state detector and signal processing electronics. A series of peaks is concluded by the resulting from X ray spectrum. The type and related amount of each element is represented in the sample by these peaks (Wachs I.E., and Fitzpatrick L.E., 1992). EDS System is shown in Figure 2.5 which includes a sensitive X-ray detector, liquid nitrogen for cooling, and analyzes energy spectra.

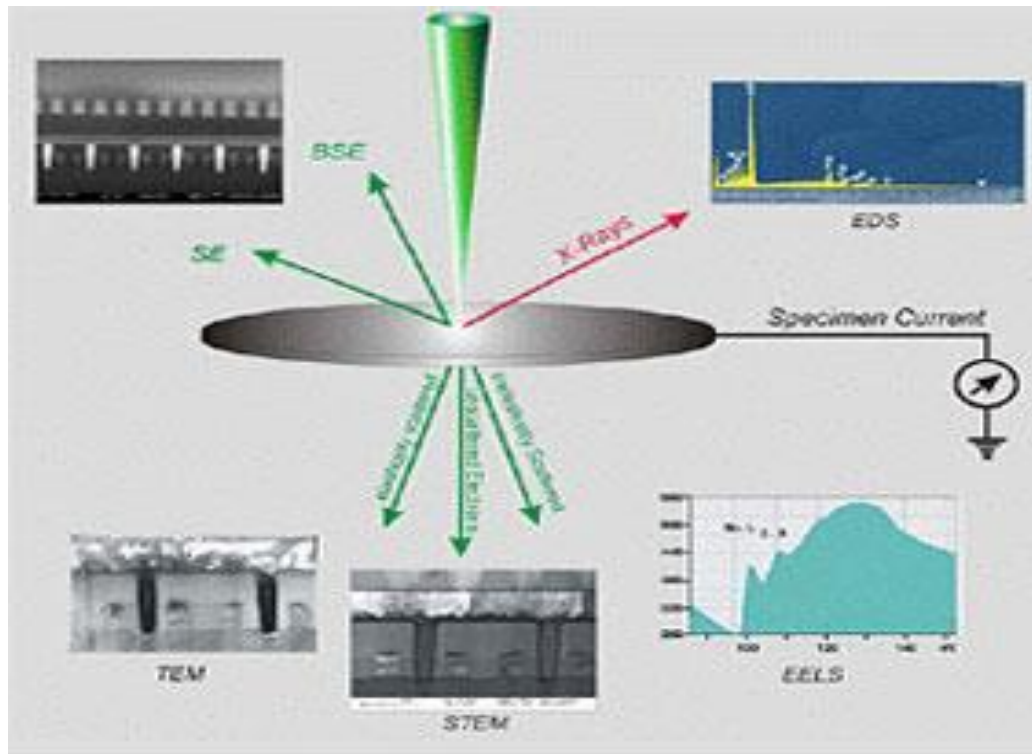


Figure 2.5. Schematic diagram of EDX-EDS system.

2.6.2 Microscopy Techniques

A significant role in many respects in characterization of semiconductors is demonstrated by microscopy techniques. The most broadly used microscopy techniques are optical microscopy, electron microscopy, and scanning probe microscopy. The optical microscopy offers important advantages than other microscopy techniques such as versatility in examination, ease of sample preparation, no vacuum requirement and sample charging problems (Yacobi B. G., 2002). The mechanically scan able probes are used by Scanning probe microscopy (SPM) for the characterization of materials in place of excitation probes like a photon beam and electron or ion beams used in other techniques. High quality surface images of materials are provided on the atomic scale by this technique as a result of interaction between the mechanically moved a fine probe and a sample.

Binnig et al. (1986) invented scanning force microscope (SFM) or AFM in 1986. It is similar to other scanning probe microscopes; the AFM is scanned with a sharp probe over the surface of a sample and measures the alterations in force between the probe tip and the sample.

The most usually used electron microscopy techniques are the SEM and TEM that provide much precious knowledge relative to the compositional, structural and defects in the structure of materials. A detailed theoretical background about the basic principles and applications of SEM is introduced in the following subsection.

2.6.2.1 Scanning Electron Microscopy (SEM)

SEM is one of the most largely used surface characterization techniques. The surface of materials is analyzed by SEM. Secondary electron imaging is most generally used because the low energy electrons transport knowledge occurring only from the surface of materials (Ohring M., 2002). A characteristic SEM system is composed of an electron gun, sample chamber, several types of detectors for different applications, and monitoring system. The accelerated high energetic electrons bombard the sample; a series of interaction with the nuclei and electrons of the sample is happened. The change in direction of incident electrons (scattering) and gradual loss of energy of electrons is caused owing to this interaction. Scattering can be both elastic and inelastic. These result in deviation of incoming electrons by nuclei of atoms called backscattered electrons and production of various signals such as emitting secondary electrons, electron-hole pairs, Auger electrons and characteristic X-rays, respectively. The interaction of electron-sample basis produced secondary electrons, back scattered electrons, and characteristic X-rays supply surface morphology, composition contrast, and elemental analysis, respectively (Yacobi B. G., 2002).

SEM has more advantages with respect to over traditional microscope (light microscope). These are; the SEM has a large depth of field, which permits more samples to be in focus at one time. Also it has much higher resolution due to those closely spaced samples that can be grown at much higher levels.

2.6.2.2 Atomic Force Microscopy (AFM)

AFM is a surface characterization technique which gives information about the structure of the sample's surface. It is interacted the structure of the sample's surface with a very sharp tip and the sample to probe. A sharp tip is located at the end of a cantilever which is held over the sample. The cantilever is detected as the tip

moves along the surface of a sample, or a sample is moved under the tip (Eaton P., and West P., 2010). The surface sample is scanned by the sharp probe so AFM get images showing the arrangement of individual atoms in a sample, or to see the structure of individual molecules. An AFM can be used in all fields of science as example chemistry, physics, material science, nanotechnology, astronomy biology medicine and more. The AFM is very interesting technique that measure surface structure with high resolution and accuracy (Sullivan et al. 2005; Schimmel et al., 1999; Sugimoto et al., 2007; Tromas et al., 2005). Various ‘spectroscopic’ modes can be work by AFM. The modes measure other properties of the sample at the nanometer scale. The AFM is different than other microscopes which are image by focusing light or electrons on a surface, such as an optical or electron microscope. The sample’s surface is physically felt with a sharp probe and a map height of the sample’s surface is created. Advantages of this technique are; 1) It produces true, 3D surface images; 2) it does not require special sample behaviors that can result in the sample's destruction or alteration; and 3) it does not require a vacuum environment in order to operate. Figure 2.6 shows an illustration of an AFM.

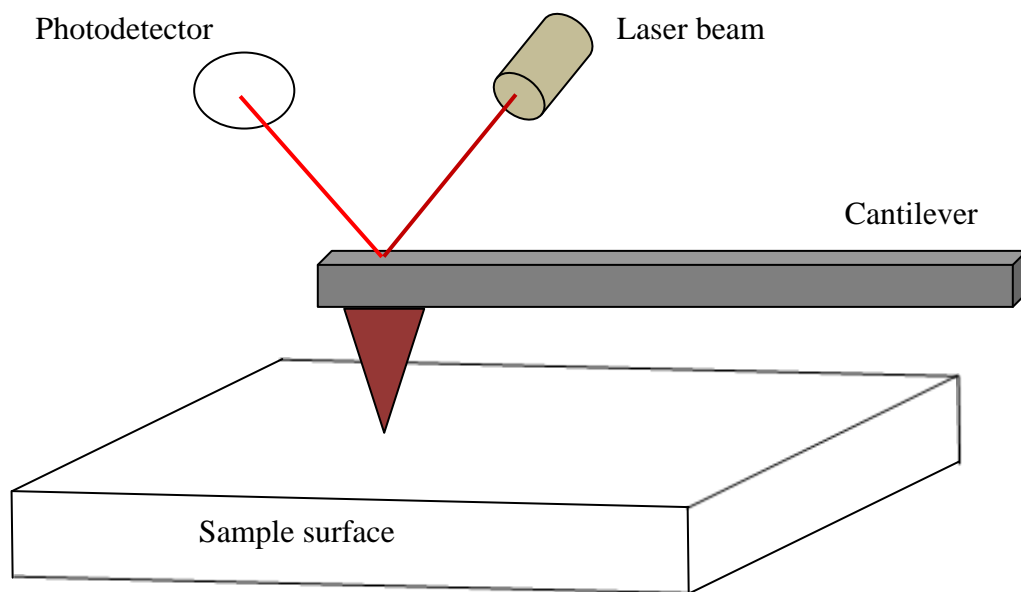


Figure 2.6. Illustration of an AFM (LuttgeInna et al.).

2.6.3 Structural Characterization

Several analytical techniques such as X-ray diffraction, neutron diffraction analysis, electron microscopy and electron diffraction can perform the determination of structural properties of solid state materials. These techniques allow to find lattice parameters, recognize the phases exist in the structure, show crystalline state (crystalline, polycrystalline or amorphous), determine defects and stress present in the structure. Previously referred parameters are obtained by X ray diffraction.

2.6.3.1 X-ray Diffraction Technique

X-rays are electromagnetic waves having wavelength about 1 \AA (10^{-10} m) which is about the same size as an atom. They can identified the structural parameters when interacted with a solid state material in several ways these are; absorbed, emitted, reflected, or transmitted. When X-rays interacts with a material owning an ordered structure (crystalline phase), a diffraction pattern is shaped. It is the fingerprint of a substance and gives precious knowledge about the structure of a material. XRD is established on constitutional interference of monochromatic X-rays and a crystalline sample. The constitutional interference is the consequence of strengthening of reflection of X-rays from the periodically dispersed parallel planes consisting of the structure of a material. The h, k, and l indices represent the orientation and inter-distance of parallel planes. These are Miller indices which determine unit cell of crystalline sample (Cullity, 1978). The unit cell is the smallest volume which is repeated periodically in three dimensions. It constructs whole crystal structure. Three axes (a, b, and c) and angles (α , β , and γ) perform the determination of unit cell. The smallest volume element permits to explain seven unit cells corresponding to the known seven crystal system. These systems are given table 2.1 (Suryanarayana, and Norton, 1998).

Table 2.1. Crystal Systems

System	Crystal System	Angels
Triclinic	$a \neq b \neq c$	$\alpha \neq \beta \neq \gamma \neq 90^\circ$
Monoclinic	$a \neq b \neq c$	$\alpha = \beta = 90^\circ, \gamma \neq 90^\circ$
Orthorhombic	$a \neq b \neq c$	$\alpha = \beta = \gamma = 90^\circ$
Tetragonal	$a = b \neq c$	$\alpha = \beta = \gamma = 90^\circ$
Hexagonal	$a = b \neq c$	$\alpha = \beta = 90^\circ, \gamma = 120^\circ$
Trigonal	$a = b = c$	$\alpha = \beta = \gamma \neq 90^\circ$
Cubic	$a = b = c$	$\alpha = \beta = \gamma = 90^\circ$

When X rays sent on crystalline material, diffraction observes several conditions. The conditions should be with the diffraction.

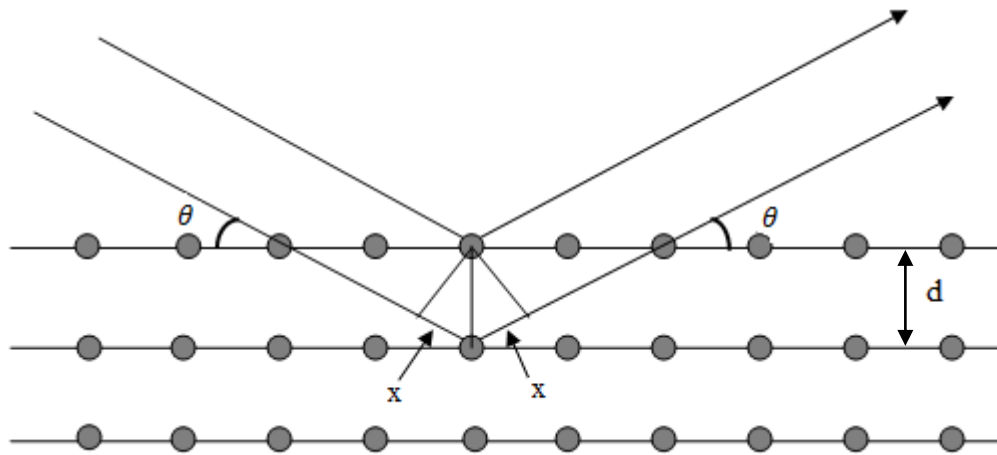


Figure 2.7. X-rays Diffraction from parallel planes.

There are several conditions; First conditions is that the angle between the incident beams and reflecting planes should be equal to that of diffracted beam and reflecting planes, the other condition is about the incident and reflected waves from planes ought to be in phase and the difference in path length must be an integral number of wavelengths. Bragg's Law expresses these conditions:

$$n\lambda = 2d\sin\theta \quad (2.1)$$

where n , λ , d , and θ are the order of diffracted beam, wavelength of the incident X-ray, inter-planar distance of parallel planes, and Bragg's angle, respectively.

2.6.4 Optical Characterization

An interaction with light in some ways can be involved in by semiconductors and result in editing of various methods as an example reflection, transmission, absorption, and scattering. Many optical devices are planned for recognizing the optical features of semiconductors. Thin film deposition method is the example of the corresponding characterization during generation method which is permitted by contactless and non-destructive optical characterization techniques (Yacobi B. G., 2002). The main optical characterization techniques are optical microscopy, optical absorption, photoluminescence, Raman spectroscopy, and optical modulation techniques.

2.6.4.1 Optical Absorption

Optical absorption and transmission are the best measurement techniques for determination the band structure of materials. When the atoms of the material uses the electromagnetic waves dropped onto the material, the energy loss is taken place as a consequence of interaction of the electrical charges inside a material. The energy loss defines as absorption. Any material with t thickness interacts with an electromagnetic wave, at the absorption is given as follows.

$$I = I_0 e^{-\alpha t} \quad (2.2)$$

where I , I_0 , t , and α are the transmitted light intensity, incident light intensity, the thickness of the specimen, and the absorption constant respectively. α depends on the wavelength of the electromagnetic wave, density of the material and the forbidden energy range of the material, and is obtained by the following equations.

$$A = \log_{10}(I_0/I) \quad (2.3)$$

$$\alpha = 2.303 \frac{A}{t} \quad (2.4)$$

Where A is the absorbance dependence on α , wavelength of the electromagnetic wave, density of material and band gap of the material. The optical absorption process is the most helpful process for researching the band structure of semiconductor with comparing other process. This process can find the knowledge about band type and forbidden energy range (Cullity, 1978).

The absorption method might be accomplished with some mechanisms; these are band to band, intercondition band, intervalence band, donor to conduction band, acceptor to conduction band, valence to donor, acceptor to condition band, and donor to acceptor transitions that conduce to the total absorption coefficient. A photon moves an electron from the valance band to the conduction band in the main absorption method. Both momentum and energy are preserved in this method. When the minimum of the conduction band and the maximum of the valance band occur at the same value of the wave vector k , transitions are direct, and the material is referred to as a direct gap semiconductor. Also by the time when the minimum of the conduction band and the maximum of the valance band occur at the different value of the wave vector k , transitions are indirect and the material is referred to as indirect-gap semiconductor. Figure 2.5 shows the schematic diagram of the direct and indirect bandgap of semiconductor.

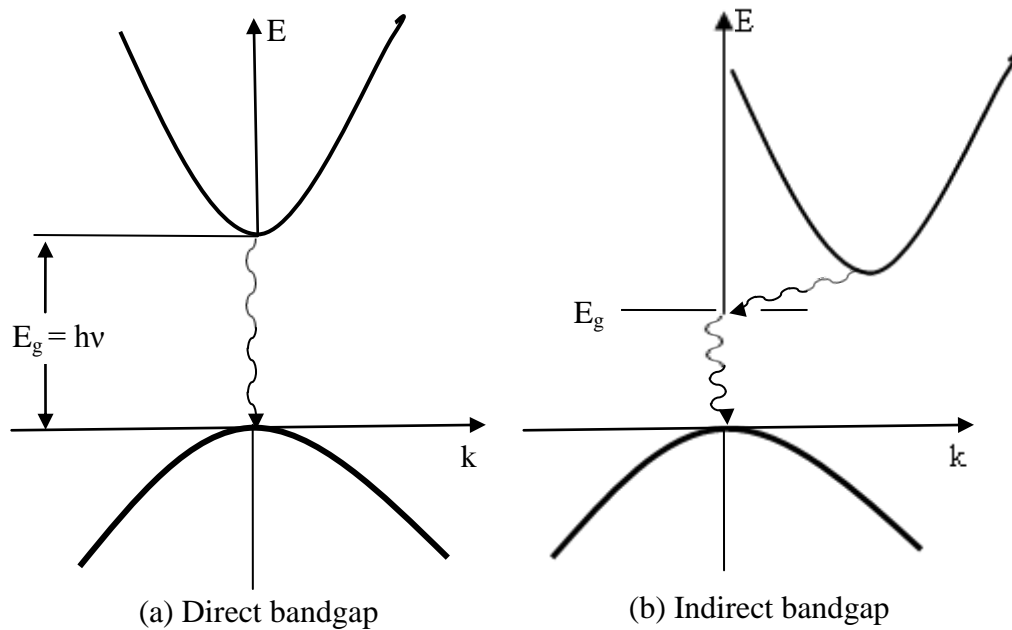


Figure 2.8. A schematic diagram of the direct and indirect bandgap of semiconductor (Costa, and Cartaxo, 2010).

The following formula demonstrates how α can be calculated through the transmission (T) and reflection (R) (Yacobi B. G., 2002).

$$T = \frac{(1-R)^2 e^{-\alpha t}}{(1-R^2) e^{-2\alpha t}} \quad (2.5)$$

3. MATERIALS AND METHODS

3.1 Introduction

In this chapter, the details of deposition of CZT thin films, microstructural, morphological and optical characterization measurements and analysis of empirical consequences are presented.

The basic impartial of this chapter is to provide the main knowledge about the deposition method of thin films and definition of experiment setups used for the investigation of microstructural, morphological and optical properties of the deposited thin films. The sections in this chapter are organized as follows. Firstly, the deposition method of thin films is offered by RF sputtering technique. This is followed by a brief introduction of basic microstructural, morphological and optical characterization systems and measurement steps.

3.2 Deposition of Thin films

3.2.1 Substrate Preparation

The deposition of CZT thin films was achieved by using RF sputtering techniques. Glass materials were used as substrates in deposition of thin films. It is known that glass material is suitable in large quantities at low cost and satisfy many physical properties (sufficient mechanical support, convenient thermal expansion coefficient for good match to II-VII compounds, sufficient surface smoothness, thermal endurance up to 550 °C without softening so much, and satisfying a good insulating) (Luque, and Hegedus, 2005). However, in this study, to carry out the preparation of CZT thin films at higher annealing temperature was required. Having obtained the substrates with desired forms, the cleaning method was operated since the clearness of the substrate has a significant influence on deposition of high quality thin films. The film growth can be disrupted by contaminants (dust and other organic materials) and led to poor quality results. As different cleaning method is necessary each material, the cleaning of glass substrates was carried out by following several

cleaning stages private to this material to remove the contaminations on the surface onto which the film will be deposited. The basic cleaning stages can be briefed as follow: Initially, to take out protein and oil molecules substrates were held in a hydrous chemical detergent solution with distilled water; then, substrates in same solution were held at temperature of about 100 °C in an ultrasonic bath for 10 minute to ease the realizing of solved contaminations. Secondly, the substrates were rinsed with hot distilled water to remove the possible left detergent contaminations remained from the former cleaning stage. Then, in order to eliminate organic contaminants substrates were dipped in a boiling diluted H₂O₂ solution approximately for 15 minute and afterward the same solution were place into ultrasonic cleaner for the same period of time. At last, substrates displaced from this solution were rinsed with hot distilled water and kept in pure methanol to keep ready for use. And, before placing them into the holder for the deposition method, blowing pressured N₂ gas dried the substrates received from the methanol.

The each sample of the CZT thin films grown at various sputtering temperature, 200°C, 300°C, 400°C, were divided into five pieces in order to apply different annealing processes. The one piece of the each sample was held as-grown. The two pieces of the same sample were separately annealed at 300°C and 450°C temperature, respectively.

3.2.2 Growth of CZT Thin Films by Sputtering Technique

In this thesis, CZT thin films were deposited by using RF Sputtering system technique. Sputtering technique is the best technique used for thin film deposition and etching procedure.

CZT films were deposited on glass substrates with different sputtering temperatures as 200, 300, and 400°C. The RF power used in the deposition procedure was 40 W. The basis pressure of the sputtering chamber was 1.5×10^{-6} Torr and it was held at 5×10^{-3} Torr throughout sputtering under Argon gas. A single 4 inch diameter CZT (99.99%) target was used. The deposited films annealed at temperatures of 300 and 400°C for 1 h under N₂ and mixed N₂H₂ ambient at atmospheric pressure. Growth rates were held at 0.3 Å/s throughout the deposition. The thicknesses of thin films were measured at about 200 nm. The sputtering system was used in this work is given in Figure. 3.1.

Vakum controller	Temperature controllers
Thickness monitor	Ar Flowmeter
DC Generator	
Infikon RF Generator	Match Box
Control Panel	

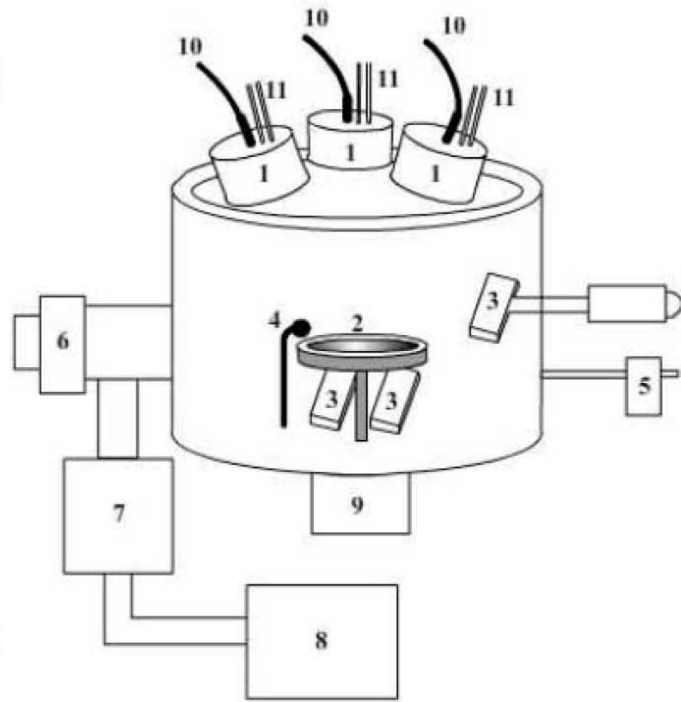


Figure 3.1. Sputtering system used for deposition of CZT thin films. The devices of the sputtering system are: 1. Magnetron heads, 2. Substrate stage, 3. Heating elements (halogen lamps), 4. Thickness measuring crystal, 5. Ar gas flow control unit, 6. Vacuum valves, 7. Turbo molecular pump, 8. Roughing pump, 9. Substrate holder rotating arrangement, 10. RF/ DC magnetron connections, 11. Water Cooling System, and 12. System control unit (Kaleli, 2010).

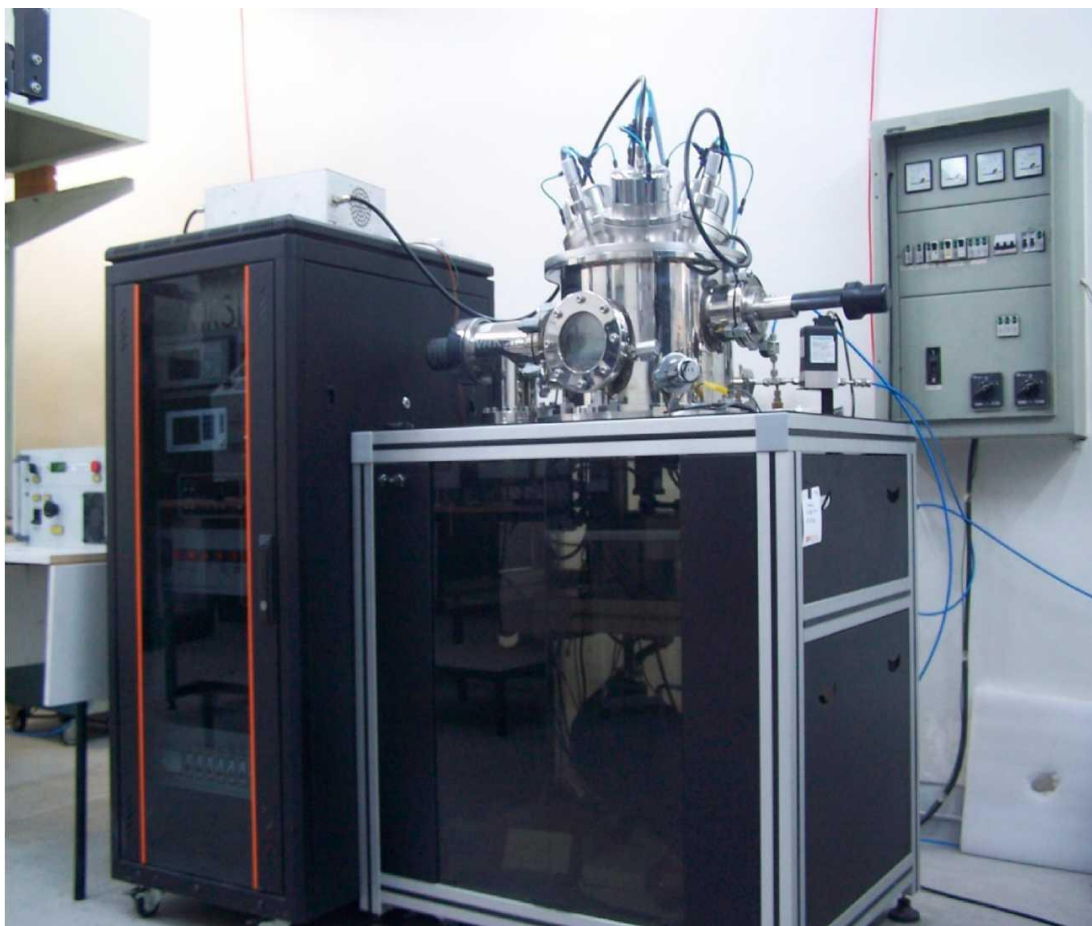


Figure 3.2. Three magnetron DC/RF sputtering system in Physics Department in Middle East Technical University.

3.3 Structural, Compositional and Surface Characterization

3.3.1 X-Ray Diffraction (XRD)

XRD is an influential technique used to characterize the structure of crystalline materials. Knowledge about features like crystallographic chemical composition and physical properties of thin films can be found from XRD analysis. XRD is used for measuring the average distance between layers, defining the orientation of a single crystal or grain, obtaining the crystal structure of an unknown material and measuring the size shape and internal stress of small crystalline regions (Ashcroft, and Mermin, 1976).

The structural features of deposited CZT thin films were studied by a Rigaku Miniflex XRD system fitted with $\text{CuK}\alpha$ X ray source. XRD patterns were gotten from 10° to 60° angles with a speed $2^\circ/\text{min}$ for all deposited thin films. XRD spectra

obtained thin films were confronted with database including XRD patterns of known material structures provided by JCPDS (Joint Committee on Powder Diffraction Standards) which supplies a database of powder diffraction patterns including the d-spacing (related to angle of diffraction) and related intensities of visible diffraction peaks, provide a database consists of XRD spectra of organic and inorganic materials. Valuable information about the structure of CZT thin films was obtained with the analysis of XRD patterns. The photo of X-ray diffraction system is shown in Figure 3.3.



Figure 3.3. Rigaku MultiFlex X-Ray Diffractometer in Physics Department at Abant Izzet Baysal University.

3.3.2 Energy Dispersive X-ray Analysis (EDXA) Measurements

EDXA (EDS or EDX) is mentioned in theoretical consideration part, it is an authoritative technique to decide the chemical composition of materials on the micro and nano-scale. In this technique, with help of identification of emitted X-rays from the interaction of bombarded electrons and the analyzed material, the amount and spatial dispersion of elements ranging from the Boron to Uranium can be measured. EDXA is mostly used as an accessory component of SEM system. EDXA equipped SEM can supply precious knowledge about the quantitative elemental analysis, sample surface morphology, and many other features. Following to the deposition, the surface morphology and composition of CZT thin films were studied by using a

SEM equipped with EDXA system in Laboratory of Physics Department at Abant Izzet Baysal University. The measurements were managed at various acceleration energies ranging from the 6 kV to 30 kV depending on the goal of study.

3.3.3 Scanning Electron Microscopy (SEM)

SEM is broadly used to characterize surface of CZT thin films. The information originating only from the surface of the sample is carried with low energy electrons. A bias voltage is applied to a detector for attracting the low energy secondary electrons distributing from the sample. A scintillator converts the detected energies into photons before entering a photomultiplier tube. These photons are ultimately converted back into electrical signals by photomultiplier tube so that they may be exhibited on a screen, generating an image of the sample's morphology.

The contrast between regions of high and low intensity is shown by a SEM image, corresponding to regions where the secondary electrons could arrive the detector (bright areas), or were blocked (dark areas). Because brighter areas correspond to regions of the sample created of heavier elements, and darker regions correspond to lighter elements (Ghosh et al., 2012). Figure 3.5 gives SEM system. After the deposition the composition and the surface morphology of CZT thin films were researched exploiting a FEI quanta 400 FEG model SEM accoutered with EDX system in Laboratory of Physics Department at Abant Izzet Baysal University.



Figure 3.4. Scanning Electron Microscopy in Physics Department at Abant Izzet Baysal University.

3.3.4 Atomic Force Microscopy (AFM)

Atomic Force Microscopy has several advantages comparing with traditional microscopy methods. The measurements can be made in 3D, x, y, and z (normal to the pattern surface) by AFM, so allowing the introduction of 3D images of a pattern surface and also the pattern can be probed. AFM can also run by measuring force from the probe to the pattern. The probe is a 3-6 nm tall pyramid with 15-40 nm and radius. Although the sideways resolution of AFM is low (~30 nm) owing to the convolution, the vertical resolution is able to be up to 0.1 nm. This specialty of AFM supplies a great advantage over any microscope. With good patterns which are clean, without immoderately large surface features, resolution in the x-y plane ranges between 0.1-1.0 nm and in the z direction is 0.01 nm (atomic resolution). In this study used Atomic force is in the central laboratory of METU for image and examines the CZT thin films.

3.3.5 X-ray Photoelectron Spectroscopy (XPS) Measurements

XPS measurement provides detailed information about the surface composition, the identification of surface or near surface chemical state of elements (chemical bonding states) and detection of contaminants. An XPS system actually is composed of a high vacuum chamber, a lens system collecting the photo generated electrons, an X-ray source (usually $MgK\alpha$), a spectrometer including electron energy analyzer and detector, and a displaying system to show the signal versus kinetic or binding energy spectra.

XPS measurements for the deposited CZT thin films were achieved by using a UNISPECS ESCA system in Central Laboratory of Middle East Technical University as shown in Fig. 3.5. XPS survey spectra obtained, after following to complex and longtime taking fitting analysis stages. These stages are: background elimination, designing convenient fitted functions, preservation of right intensity ratio of spin-orbit doublets for p, d, and f photoelectron lines, and calibration of binding energies. They give detailed knowledge about the composition and bonding nature of constituent elements present at surface/near surface of CZT thin films.

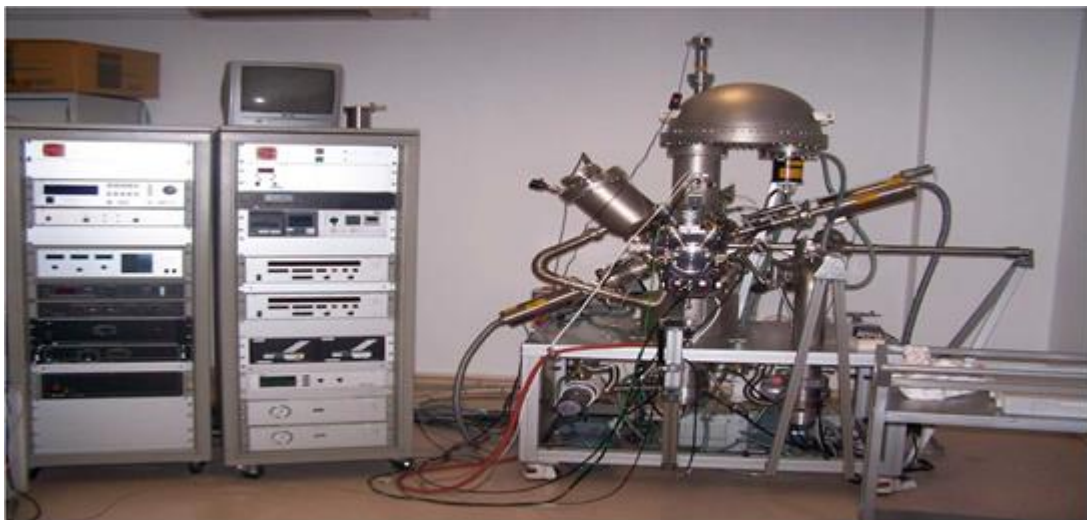


Figure 3.5. XPS System in Central Laboratory of Middle East Technical University.

3.4 Optical Analysis

3.4.1 Absorption and Transmission Measurements

Optical features of semiconductor study's main characterization instruments are the transmission and absorption. Optical absorption coefficient, optical bandgap, and optical constants particularly refractive index and extinction coefficient can be computed from transmission and absorption. Transmission and absorption can be measured with a photo spectrometer which is an optic system.

In this study for the optical characterization, normal incidence reflectance R and transmittance T were decided in the wavelength range of 400–1000 nm using Shimadzu UV-360 spectrometer at room temperature. In the range of strong absorption of the radiation, the absorption coefficient has been computed from the relation $\alpha = (1/t) \ln(100/T)$. A plot of $(\alpha h\nu)^{1/2}$ vs. $h\nu$ for the films of different composition is approximately linear indicating the direct bandgap nature of the films (Ismail et al., 2009). Where h is Planck constant and ν is frequency of incident light respectively.

4. RESULTS AND DISCUSSIONS

4.1 Introduction

The aim of the work is to characterize the structural and optical properties of CZT thin films by using AFM, EDX, SEM and XPS measurements. The CZT thin films were deposited on glass by using a single CZT sputtering target. The effects of RF Sputtering temperature (T_s) and annealing temperature (T_a) on the deposition of the CZT films were investigated.

4.2 Characterization of CZT Thin Films Deposited by Sputtering Technique

4.2.1 Structural Analysis

CZT thin films were characterized by XRD technique and the spectra were resolved to get knowledge about different crystallographic appearances involving crystallinity, size evolution, a_x , and x of the films. The empirical a_x for CZT thin films is able to be acquired from the Bragg's relation ($2d_{hkl}\sin\theta = n\lambda$), by taking θ values from the XRD spectra, where n , λ , d , and θ are the order of diffracted beam, wavelength of the incident X-ray, inter-planar spacing of parallel planes, and Bragg's angle, respectively. The characteristic diffraction of all samples both for as-deposited and annealed CZT thin films at various temperatures are exhibited in spectra given in Figures 4.1-4.6. It is observed that the deposition conditions play a significant role in defining their structure. As the deposition temperature increases, the peak intensity also increases. The X-ray diffraction patterns of the CZT thin films is revealed that polycrystalline nature is predominant (111) orientation of the cubic phase. The other diffraction peaks were corresponding to the (220), (311), (400), (331), (422) and (333) orientations viewed with enlarge in Zn content in the CZT films.

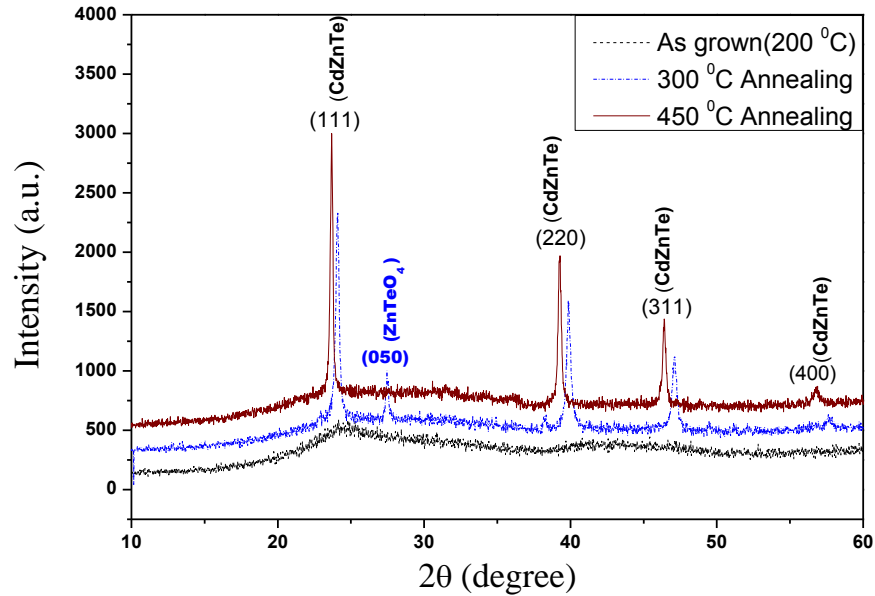


Figure 4.1. XRD spectra of CZT thin films grown at 200°C (as-grown) and annealed at 300°C and 450°C under N₂ gases, respectively.

The sample of the CZT thin films grown at 200°C sputtering temperature were divided to five pieces in order to apply different annealing processes. The first piece of the sample was kept as-grown. The two pieces of the same sample were separately annealed under N₂ ambient at 300°C and 450°C temperature, respectively. The XRD spectra for first three samples were compared as given in Figure 4.1. It is observed that annealing temperature increases the crystallinity as expected.

The last two pieces of the sample were annealed at 300°C and 450°C under N₂H₂ ambient, and XRD measurements were performed as given in Figure 4.2. The crystallization behavior of the XRD measurements was similar to that of the samples annealed under N₂ ambient.

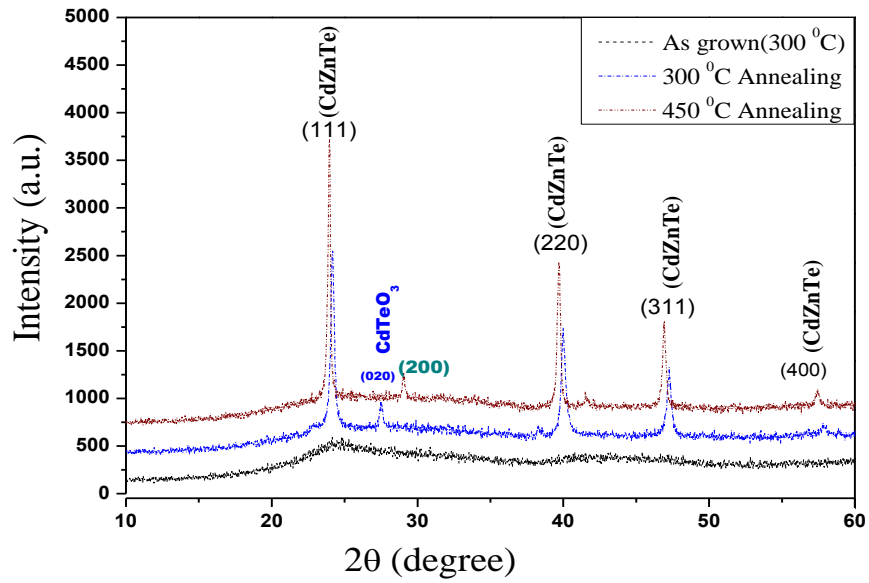


Figure 4.2. XRD spectra of CZT thin films grown at 200°C (as-grown) and annealed at 300°C and 450°C under N_2H_2 gases, respectively.

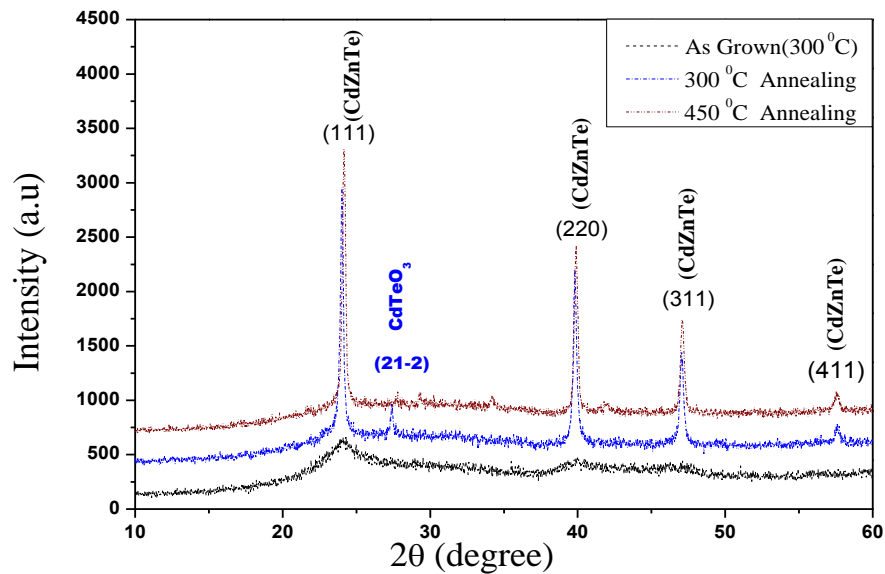


Figure 4.3. XRD spectra of CZT thin films grown at 300°C (as-grown) and annealed at 300°C and 450°C under N_2 gases, respectively.

The sample of the CZT thin films grown at 300°C sputtering temperature were divided to five pieces in order to apply different annealing processes. The first piece of the sample was kept as-grown. The two pieces of the same sample were separately annealed under N_2 at 300°C and 450°C temperature, respectively. The XRD spectra for first three samples were compared as given in Figure 4.3. It is observed that annealing temperature increases the crystallinity as expected.

The last two pieces of the sample were annealed at 300°C and 450°C under N_2H_2 ambient, and XRD measurements were performed as given in Figure 4.4. The crystallization behavior of the XRD measurements was similar to that of the samples annealed under N_2H_2 ambient.

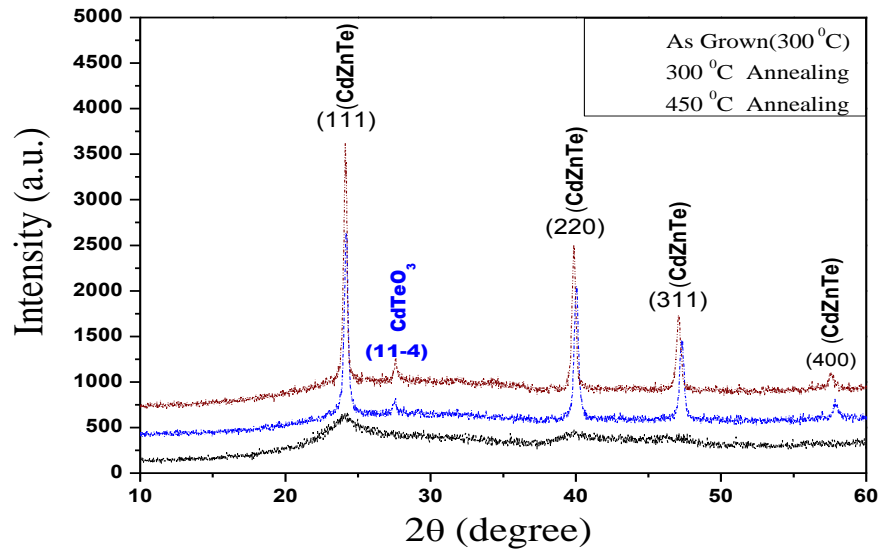


Figure 4.4. XRD spectra of CZT thin films grown at 300°C (as-grown) and annealed at 300°C and 450°C under N_2H_2 gases, respectively.

The sample of the CZT thin films grown at 400°C sputtering temperature were divided to five pieces in order to apply different annealing processes. The first piece of the sample was kept as-grown. The two pieces of the same sample were separately annealed under N_2 at 300°C and 450°C temperature, respectively. The XRD spectra for first three samples were compared as given in Figure 4.5.

The last two pieces of the sample were annealed at 300°C and 450°C under N_2H_2 ambient, and XRD measurements were performed as given in Figure 4.6. The crystallization behavior of the XRD measurements was similar to that of the samples annealed under N_2 ambient.

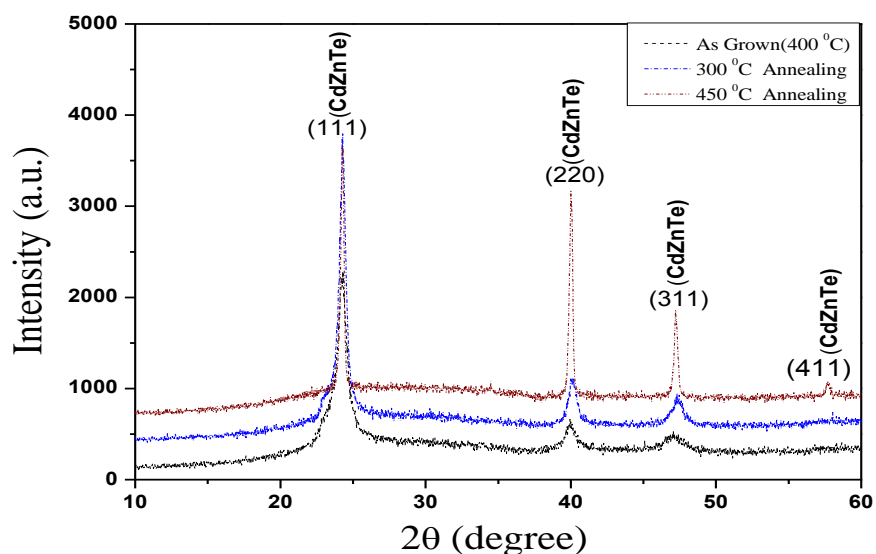


Figure 4.5. XRD spectra of CZT thin films grown at 400°C (as-grown) and annealed at 300°C and 450°C under N₂ gases, respectively.

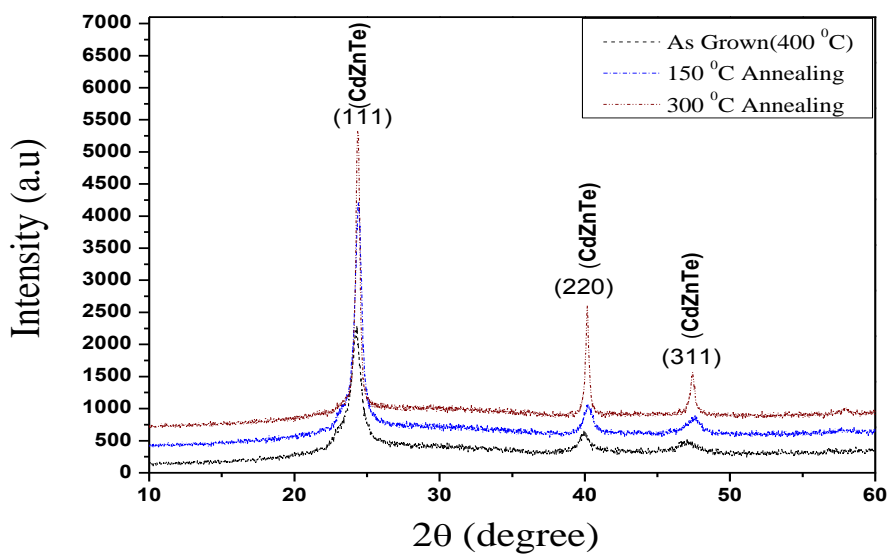


Figure 4.6. XRD spectra of CZT thin films grown at 400°C (as-grown) and annealed at 300°C and 450°C under N₂H₂ gases, respectively.

Three primary diffraction peaks come into view at $\sim 24^\circ$, $\sim 40^\circ$, and $\sim 47^\circ$ which change with x value. They have been recognized corresponding to the (111), (220) and (311) diffraction peaks of CZT. The XRD samples were offset to exhibit the diffraction peaks clearly. All patterns even the as-deposited one demonstrate polycrystalline structure and mostly preferential [111] orientation. The empirical lattice constant of the CZT can be estimated from characteristic (111) peak, placed

from that's of CdTe (23.77°) to ZnTe (25.30°) peaks. Therefore, we expect that correspondence a_x places from that's of CdTe (6.4810Å) [JCPDS file No. 15-0770] to ZnTe (6.1026Å) [JCPDS file No. 15-0746].

Bragg's law is derived as

$$2d_{hkl}\sin\theta = n\lambda, \quad (4.1)$$

where

$$d_{hkl} = \frac{a}{\sqrt{h^2+k^2+l^2}}. \quad (4.2)$$

When d is put in the Braggs law:

$$\frac{2a\sin\theta}{\sqrt{h^2+k^2+l^2}} = n\lambda. \quad (4.3)$$

Then, if $\sin\theta$ left alone on the left side:

$$2a\sin\theta = \lambda * \sqrt{h^2 + k^2 + l^2}. \quad (4.4)$$

Finally:

$$a = \frac{\lambda}{2\sin\theta} * \sqrt{h^2 + k^2 + l^2}. \quad (4.5)$$

From Eq. (4.5), it can found a is equal to the a_x which is used in Vegard's law to find x that the value of Zn in the compound. The average value of “ x ” observed d -values three XRD peaks using the following formula (Vegard's law):

$$a(\text{Cd}_{1-x}\text{Zn}_x\text{Te}) = (1 - x) * a_{\text{CdTe}} + x * a_{\text{ZnTe}} \quad (4.6)$$

from the Vegard's law

$$x = \frac{a_{\text{CdTe}} - a_x}{a_{\text{CdTe}} - a_{\text{ZnTe}}}. \quad (4.7)$$

where $a_{\text{CdTe}} = 6.4810 \text{ \AA}$ and $a_{\text{ZnTe}} = 6.1026 \text{ \AA}$. As an example, x can be found from the 200°C sputtering temperature, and 300°C annealing. For the first peak $2\theta = 24.06^\circ$, $\theta = 12.03^\circ$, λ is a constant which is equal 2.37 \AA and $a = d_x = 6.4923 \text{ \AA}$ and Miller indices (111) for the first peak which can be found from the XRD data base analysis program. All of the other Miller indices and their compounds were found from ICDD XRD data base program that given in Table 4.1. These θ , λ and Miller indices values were put in Eq. (4.5) and a values were calculated.

$$a = \frac{2.37}{2 \sin(12.03)} \sqrt{1^2 + 1^2 + 1^2}. \quad (4.8)$$

From vegard's law

$$x = \frac{6.4810 \text{ \AA} - 6.4923 \text{ \AA}}{6.4810 \text{ \AA} - 6.1026 \text{ \AA}} = 0.235574. \quad (4.9)$$

It is evident that the changes the atomic ratio of Cd: Zn; Te are affected in the sputtering temperatures leading to shifts in the peak position of the samples in the XRD spectra. At higher temperature, Zn concentrations increase with increasing in T_s . Zn has higher thermal energy to incorporation with CdTe and also diffusion of Zn into the enhancement of the material composition with temperature, therefore, rise in the Zn concentrations at higher T_s the improvement in thermal energy and diffusion of the Zn at higher T_s may attribute to rise in the Zn concentrations. In addition, some minor impurity peaks assigned to CdTeO_3 could be observed in the structure. This is due both to the relatively lower amount of zinc in the respective pattern and the relationship of CdTe for oxygen in absence of Zn. However, it is possible to get pure CZT film with heat treatment at higher sputtering temperatures. The strongest intensity of (111) peak is obtained for the sample deposited at 400°C , confirming that it has the best crystallinity and the largest grain size among the other samples.

Table 4.1.a) The x and calculated E_g values by using different deposition and annealing temperature under N_2 gases.

Sputtering Temperature ($^{\circ}C$)	Annealing Temperature ($^{\circ}C$)	Peak Peak	2θ	$a=a_x$	x values	E_g Calculated from $(1.510+0.606*x^2+0.139*x^2)$ (Cavacoli et al., 2008)	E_g Calculated from $(1.5045+0.631*x+0.128*x^2)$ (Gaduputi, 2004)
200	As grown	1. Peak	24.38	6.36	0.32	1.72	1.72
		2. Peak	40.38	6.31	0.46	1.82	1.82
		3. Peak	47.788	0	0	1.51	1.51
	300	1. Peak	24.06	6.37	0.30	1.7	1.7
		2. Peak	39.84	6.37	0.29	1.7	1.7
		3. Peak	47.08	6.37	0.28	1.69	1.69
	450	1. Peak	23.746	6.43	0.14	1.59	1.59
		2. Peak	39.24	6.41	0.18	1.62	1.62
		3. Peak	46.38	6.42	0.17	1.62	1.62
300	As grown	1. Peak	24.16	6.37	0.30	1.7	1.7
		2. Peak	39.68	6.35	0.35	1.74	1.74
		3. Peak	0	0	0	1.51	1.5
	300	1. Peak	24	6.37	0.31	1.71	1.71
		2. Peak	39.78	6.37	0.31	1.71	1.71
		3. Peak	47.02	6.37	0.30	1.7	1.7
	450	1. Peak	24.14	6.36	0.31	1.68	1.68
		2. Peak	39.86	6.39	0.24	1.66	1.66
		3. Peak	47.06	6.39	0.23	1.66	1.66

Table 4.1.b) This table is continuation of table 4.1.a.

Sputtering Temperature ($^{\circ}C$)	Annealing Temperature ($^{\circ}C$)	Peak	2θ	$a=a_x$	x values	E_g Calculated from $(1.510+0.606*x^2+0.139*x^2)$ (Cavacoli et al., 2008)	E_g Calculated from $(1.5045+0.631*x+0.128*x^2)$ (Gaduputi, 2004)
400	As grown	1. Peak	24.24	6.35	0.35	1.74	1.74
		2. Peak	39.94	6.37	0.28	1.69	1.69
		3. Peak	47.02	6.4	0.22	1.65	1.65
	300	1. Peak	24.3	6.31	0.46	1.81	1.82
		2. Peak	40.1	6.34	0.39	1.76	1.77
		3. Peak	47.36	6.33	0.40	1.78	1.78
	450	1. Peak	24.26	6.31	0.45	1.79	1.8
		2. Peak	40	6.34	0.36	1.75	1.75
		3. Peak	47.22	6.35	0.34	1.73	1.73

From the characteristic (111) peak using a Scherrer's equation calculates the average grain size of the fabricated films,

$$P = \frac{0.9\lambda}{\beta \cos(\theta)} \quad , \quad (4.10)$$

where β is the full width at half maximum (FWHM) of the peak corresponding to (*hkl*) plane, λ (= 1.54 Å) the wavelength of radiation used in XRD study, and θ the Bragg angle at peak position. Using the Eq. (4.10), the average crystallite size for (111) plane was calculated to be 6.5 nm, 18.5 nm and 49 nm for 200°C, 300°C and 400°C sputtering temperatures, respectively. The grain sizes of the patterns augmented and FWHM diminished while T_s was augmenting. It can be attributed that the crystallization degree was enhanced with the T_s . In other words, higher T_s enhanced the mobility of the deposited atoms leading to coalition of smaller grains (Malkas et al., 2014).

FWHM and grain size values are shown for CZT films deposited at various sputtering and annealing temperatures under N_2 and N_2H_2 in Tables 4.2 and 4.3, respectively. From XRD spectra it is clear that the intensity of (111) peak increases with increasing annealing temperature from 150 to 450 °C at 400 sputtering temperature, thus, is indicating a better crystallinity. That is, FWHM for the (111) is decreasing with increasing annealing temperature as seen Tables 4.2 and 4.3. Based on (111) peaks, the grain size of the films annealed at 150, 300 and 450 °C were calculated using the Scherrer's formula (Eqn. 4.10). It was found that the grain size increased. For example, at 400 °C sputtering temperature it increases from 13.7 to 49.2 nm with increasing annealing temperature from 150 to 450 °C under N_2 in Table 4.2. Also it increases from 12.8 to 25.8 nm at 400 °C sputtering temperature with increasing annealing temperature from 150 to 450 °C under N_2H_2 in Table 4.3.

Table 4.2. FWHM values and grain sizes for CZT films deposited at various sputtering and annealing temperatures under N_2 .

Sputtering Temperature (°C)	Annealing Temperature (°C)	FWHM	2θ	Grain Size (nm)
200	300	1.264	24.079	6.1
	450	1.224	23.677	6.5
300	300	0.542	24.014	14.9
	450	0.438	24.157	18.5
400	150	0.93	24.195	13.7
	300	0.446	24.289	18.2
	450	0.165	24.279	49.2

Table 4.3. FWHM values and grain sizes for CZT films deposited at various sputtering and annealing temperatures under N₂H₂.

Sputtering Temperature (°C)	Annealing Temperature (°C)	FWHM	2θ	Grain Size (nm)
200	300	0.27	24.172	30.1
	450	0.205	23.940	39.22
300	300	0.301	24.187	26.9
	450	0.268	24.128	30.4
400	150	0.635	24.213	12.8
	300	0.483	24.403	16.8
	450	0.315	24.369	25.8

Moreover, the diffraction peaks are tinnier and intense showing developed crystallinity of the alloy by augmenting annealing temperature up to 450°C. The coalescing between the grains guiding to the formation of larger grains were enhanced. As the annealing temperature increases, the peak intensity also increases as seen in Figures 4.1-4.6. This result shows that annealing procedure is to supply the movement freedom of the Cd, Zn and Te atoms to form the crystalline structure. One can conclude that, the entire inclusions of the Zn atoms in the CdTe lattice and the precipitation in crystalline form of the residual free Te atoms are determined the heat treatment of such samples. It can be seen that, with the increase of RF sputtering temperature from these Figures, the crystallinity is also increasing.

4.2.2 Surface Morphology

4.2.2.1 SEM Measurements

An electron microscope was used to produce a magnified image of the samples. The scanning of the sample with a focused electron beam and detecting the secondary or backscattered electrons produce the image in SEM (Schroder, 2006). SEM measurements have been performed to acquire knowledge about surface morphology and elemental compound of the CZT thin films which is obtained by EDX in SEM system. As it is shown in the Figures 4.7-4.15, uniformity of sample surface increases after the post-annealing procedure. Throughout the surface, there are accumulations which are large randomly distributed before the annealing procedure and they are observed through images. Those accumulations cause incomplete solid reaction as the thermal energy that is derivated from driving force

does not exist or insufficient. The accumulations nearly disappeared and ended in a smoother, thicker and more uniformed shape thanks to the thermal energy caused by the post-annealing procedure.

Figure 4.7 shows the SEM images of CZT thin films which deposited at the sputtering temperature of 200°C 1 μ m, and 5 μ m respectively. Also Figure 8a-8c shows SEM images of the sample deposited at sputtering temperature of 200°C and 300°C annealed 400 nm, 1 μ m and 5 μ m respectively, with increasing the temperature. SEM image getting larger grain size whose means sample crystallinity is increasing with temperature. The SEM images of the samples deposited at sputtering temperature of 200°C and annealed at 450°C are shown 1 μ m-5 μ m in Figure 4.9 respectively. It may be seen that from the Figure 4.9 with the augmentation of the annealing temperature, after a definite point is evaporated Te, so the hill and the gaps can be seen in the SEM images.

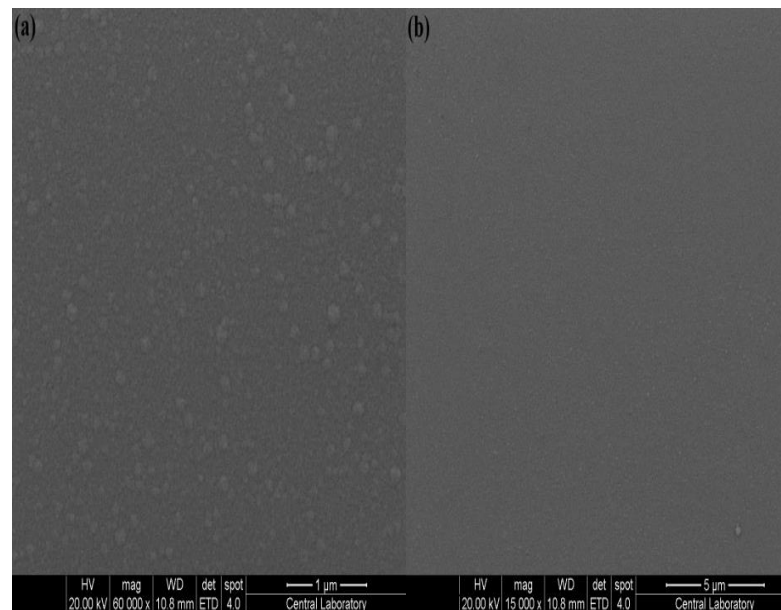


Figure 4.7. SEM image of CZT thin films at the sputtering temperature of 200°C (as-grown) (a) 1 μ m and (b) 5 μ m respectively.

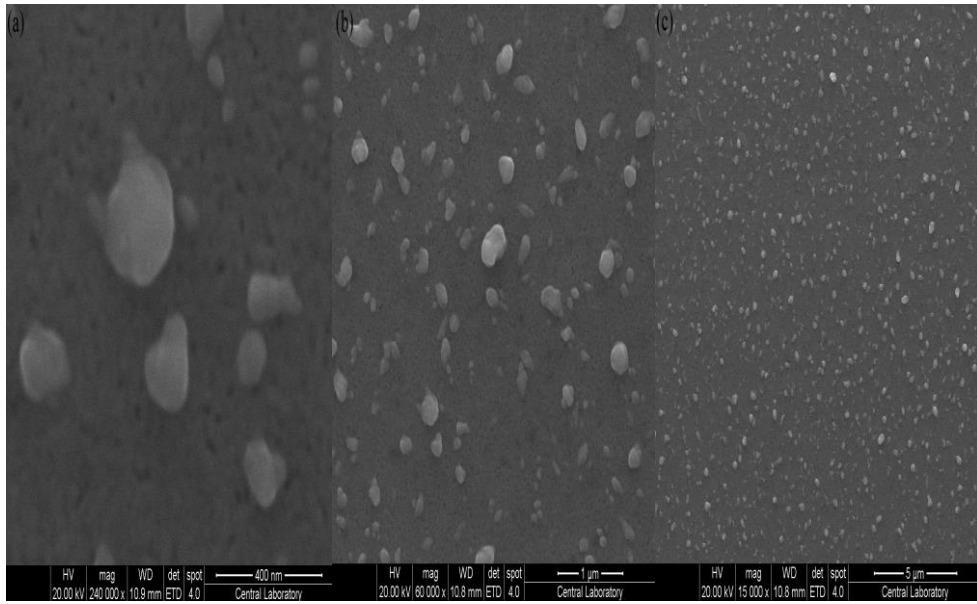


Figure 4.8. SEM image of CZT thin films deposited at $T_s=200^\circ\text{C}$ and at $T_a=300^\circ\text{C}$, (a) 400 nm (b) 1 μm (c) 5 μm respectively.

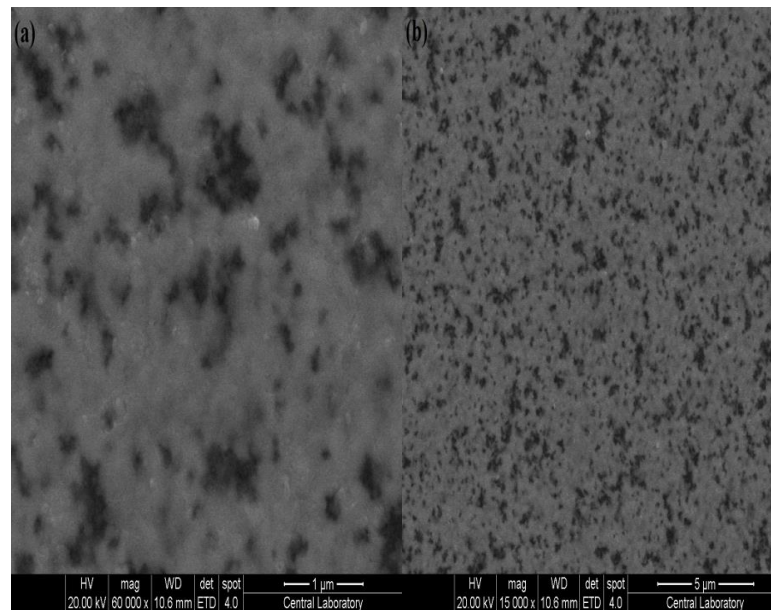


Figure 4.9. SEM image of CZT thin films deposited at $T_s=200^\circ\text{C}$ and at $T_a=450^\circ\text{C}$ (a) 1 μm and (b) 5 μm respectively.

The SEM image of CZT thin films deposited at 300°C (as-grown) is shown in Figure 4.10, images 500 nm, 5 μm , and 1 μm respectively. It seems that, Figure 4.10c has an ordered structure than those of given in Figure 4.10a and Figure 4.10b. Figure 4.11 shows the SEM image of CZT thin films deposited at sputtering temperature of 300°C and at $T_a=300^\circ\text{C}$. Figure 4.11b has an ordered structure than Figure 4.11a. SEM image of at 300°C the sputtering temperature and annealed at 450°C images are

exhibited in Figure 4.12. It is observed from Figure 10-12, that the granular structure became more prominent with rise in the annealing temperatures.

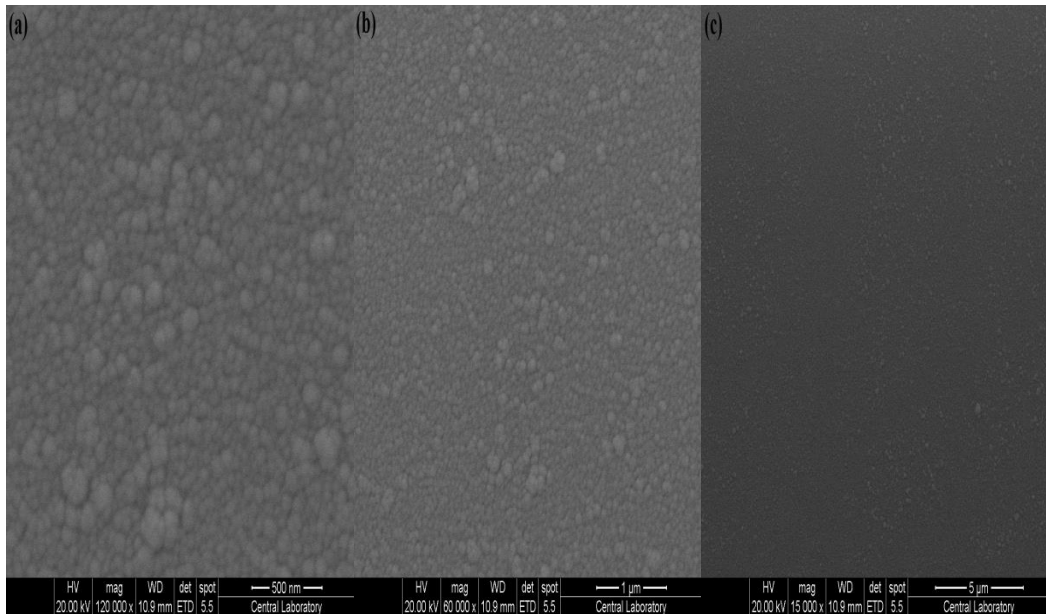


Figure 4.10. SEM image of CZT thin films at $T_s=300^\circ\text{C}$ (as-grown) (a) 500 nm, (b) 1 μm , and (c) 5 μm respectively.

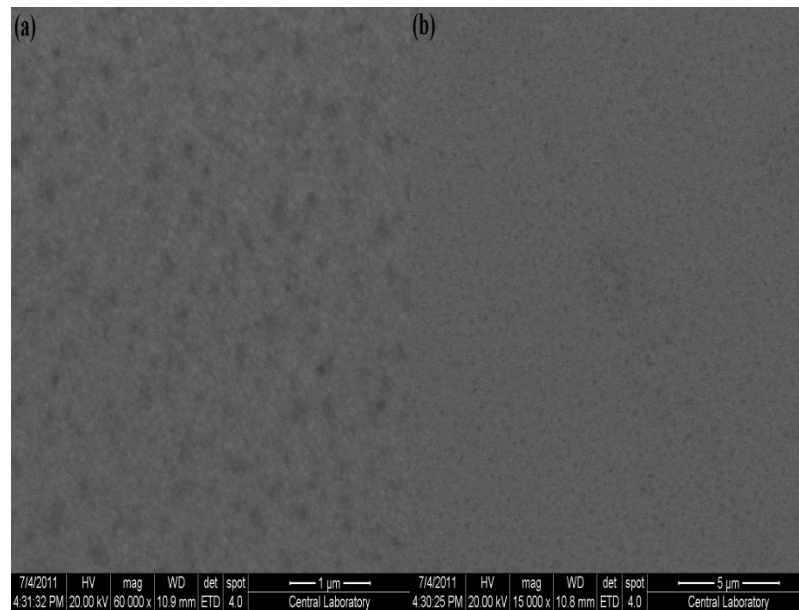


Figure 4.11. SEM image of CZT thin films deposited at $T_s=300^\circ\text{C}$ and at $T_a=300^\circ\text{C}$ images (a) 1 μm , and (b) 5 μm respectively.

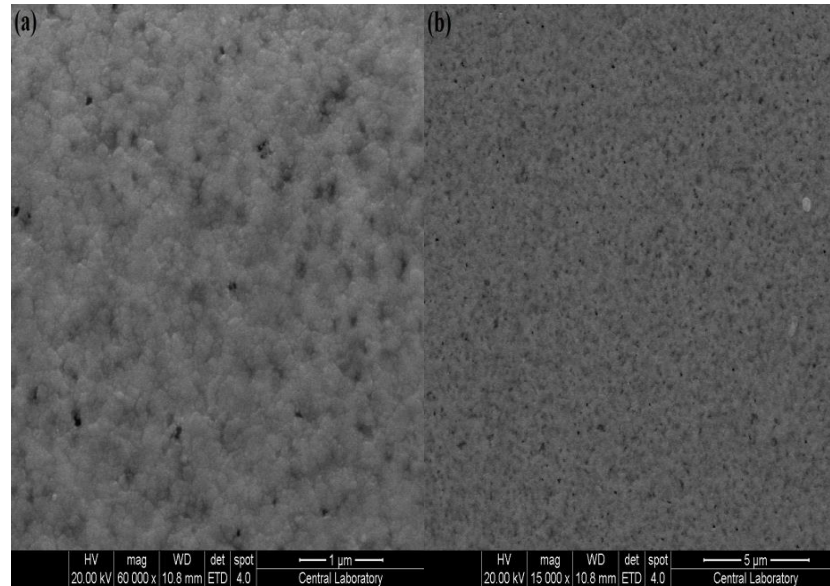


Figure 4.12. SEM image of CZT thin films deposited at $T_s=300^\circ\text{C}$ and at $T_a=450^\circ\text{C}$ images (a) $1\ \mu\text{m}$, and (b) $5\ \mu\text{m}$ respectively.

Figures 4.13-4.15 show SEM images deposited at 400°C (as grown), annealed at 300°C , and 450°C respectively. In proportion to the as-deposited pattern in which regions with light gray set off match to the rough surfaces present in Figure 4.13(a). The pattern annealed at 300°C has a very uniform and condensed morphology and especially images confirm the improvement of crystallinity in Figure 4.14(c). Figures 4.14(c) and 4.15(a) confront the SEM images of CZT thin films annealed at 300°C and 450°C . While two patterns possess a very close-packed nano grains, in the pattern annealed at 450°C regions with dark gray set off match to hole-like properties has been observed. These properties with diameters smaller than $50\ \text{nm}$ discernible as dark spots in Figure 4.15(b) are different from very large dark properties with sizes about $10\ \mu\text{m}$ in Figure 4.15(d). They were addressed as Te and inclusions and their role has been under discussion because the introduction of the CZT detectors as a room-temperature X- and γ -ray detector. Te precipitate is a result of the retrograde solid solubility of tellurium cooling to room temperature, involving a nucleation procedure. Otherwise, Te inclusions in CdTe or CZT crystals originate at the growth interface. Te-rich droplets are trapped at the boundary layer of the interface as a result of morphological instability of the liquid–solid interface.

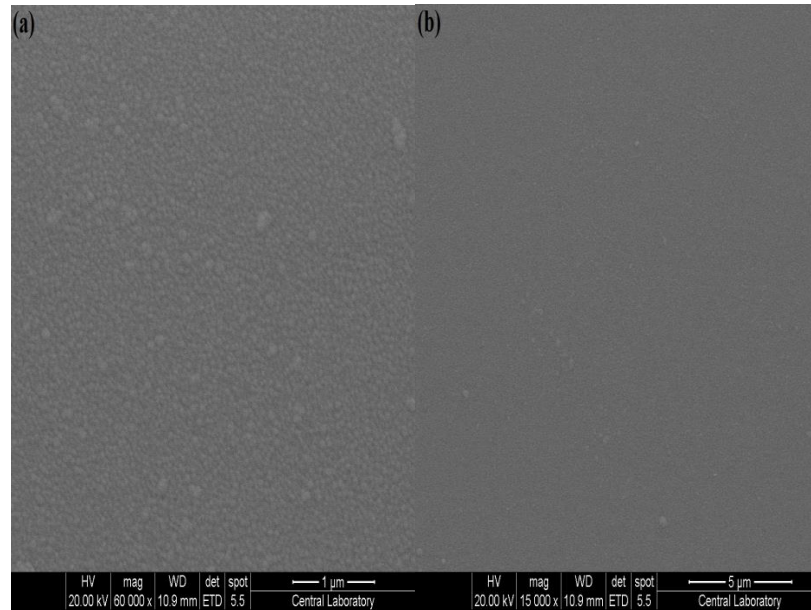


Figure 4.13. SEM image of CZT thin films at $T_s=400^\circ\text{C}$ (as-grown) (a) 1 μm , and (b) 5 μm respectively.

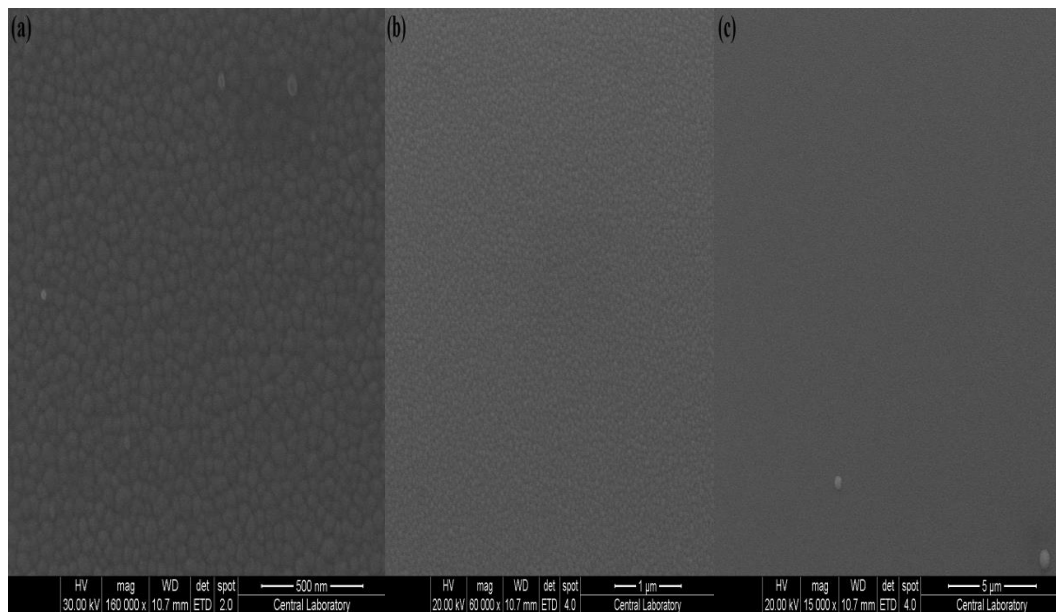


Figure 4.14. SEM image of CZT thin films at $T_s=400^\circ\text{C}$ (as-grown) at $T_a=300^\circ\text{C}$ (a) 500 nm, (b) 1 μm , and (c) 5 μm respectively.

In Figures 4.9(a), 4.12(a) and 4.15(b) show the surface morphology evolution of the heat-treated of films. It is seen that the deposited thin films is exhibited different nanostructure. The surface is smoothed by the enhancement of surface diffusion of CZT atoms and the grain sizes of CZT films increase with sputtering temperature. Due to the poor crystallinity of the film at low sputtering temperature

could hardly discerned CZT grains. Fig 4.15(b) can be discerned coalition of nano grains to elliptical clusters at higher temperatures.

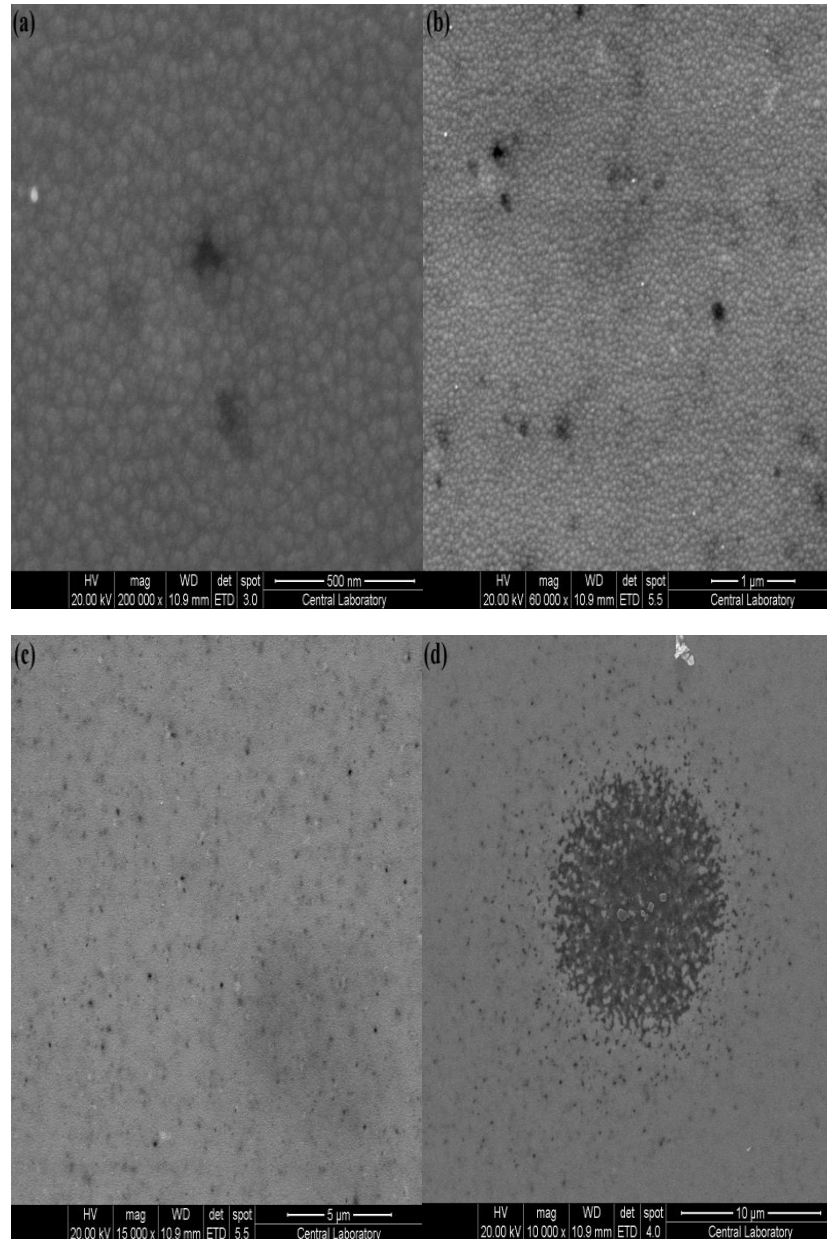


Figure 4.15. SEM image of CZT thin films at $T_s=400^\circ\text{C}$ (as-grown) and at $T_a=450^\circ\text{C}$ images (a) 500 nm, (b) 1 μm , (c) 5 μm , and (d) 10 μm respectively.

The XRD results also support the obtained SEM measurements. All this results indicates the deposited and annealed films uniformly and crystallinity enhance with higher deposition and annealing temperatures.

4.2.2.2 AFM Measurements

AFM measurements have been executed to investigate the surface of the $\text{Cd}_{1-x}\text{Zn}_x\text{Te}$ alloys and evolution by annealing behaviors in details. AFM can be used to study a wide variety of samples that are plastic, metal, glass, semiconductor, and biological samples such as the walls of cells and bacteria.

In this study, AFM is used for imaging CZT thin films deposited at 200-300-400°C RF sputtering temperature. Firstly, some of them were annealed from 300 to 450°C temperature, secondly; their images were analyzed with high-resolution. The red, black, and yellow regions remark Cd ion, Zn ion, and Te ion concentrations in order of in images.

The empirically specified two dimensional high resolution and three dimensional low resolution which are 0.5 μm -0.5 μm , 1.00 μm -1.00 μm and 5.00 μm -5.00 μm . Surface morphology of CZT thin films as displayed by AFM were shown. AFM images of the samples as-deposited on glass substrates are shown in Figures 4.16, and 4.17. The imaged area was 0.5*0.5 μm , 1.0*1.0 μm and 0.5*0.5 μm Granule, Pyramidal, Compact, Cavitations free growth of grain size 0-1 μm crystallites may be viewed obviously across the surface from the figures. The surface morphology of $\text{Cd}_{1-x}\text{Zn}_x\text{Te}$ films was obtained to be dependent on the concentration of Zn ions in the electroplating bath. Pyramidal grain growth with compact, void free and nearly uniform morphology was watched for all $\text{Cd}_{1-x}\text{Zn}_x\text{Te}$ films.

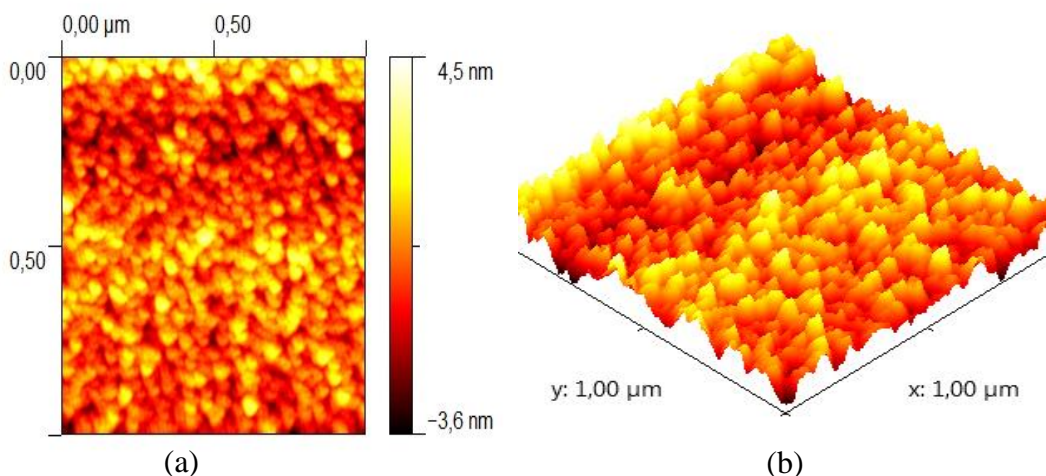


Figure 4.16. AFM images of CZT thin films as-grown on glass substrates (a) - 3.6;+4.5 nm in two dimensions, (b) 1 μm x 1 μm in three dimensions.

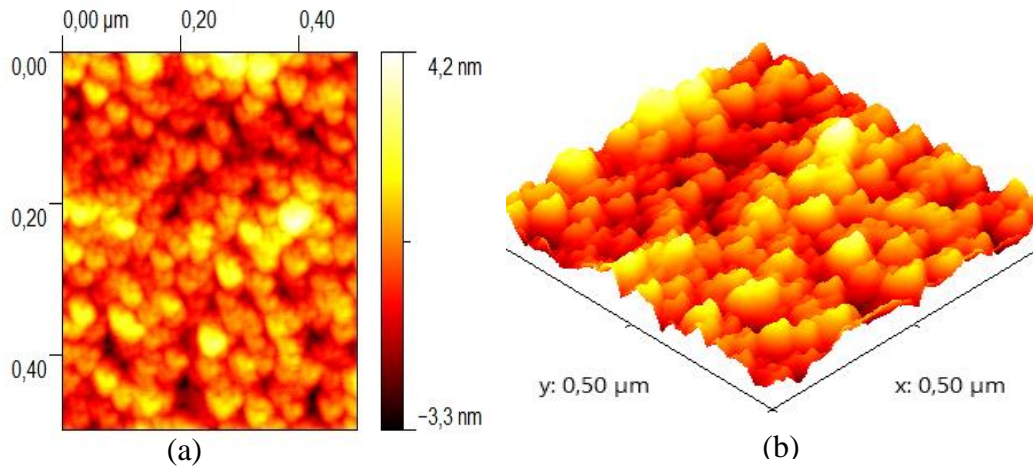


Figure 4.17. AFM images of CZT thin films as-grown on glass substrates (a) - 3.3;+4.2 nm in two dimensions, (b) 0.5 μm x 0.5 μm in three dimensions.

The surface morphology of as-deposited CZT films is shown in Figures 4.16-4.17. As seen from these figures, grain boundaries are not clear on the surface of the films, which is likely due to the existence of non-crystalline or amorphous portion. The surface forms a hillock structure.

The typical surface morphology of the CZT thin films show at $T_s=200^\circ\text{C}$ (as grown) in Figures 4.18-4.20. Also grain boundaries are not clear for these films. The Zn concentration increases with annealing temperature as seen from Figures 4.21-4.23 (at 300°C annealing temperature) and Figures 4.24-4.25 (at 450°C annealing temperature) with dark regions.

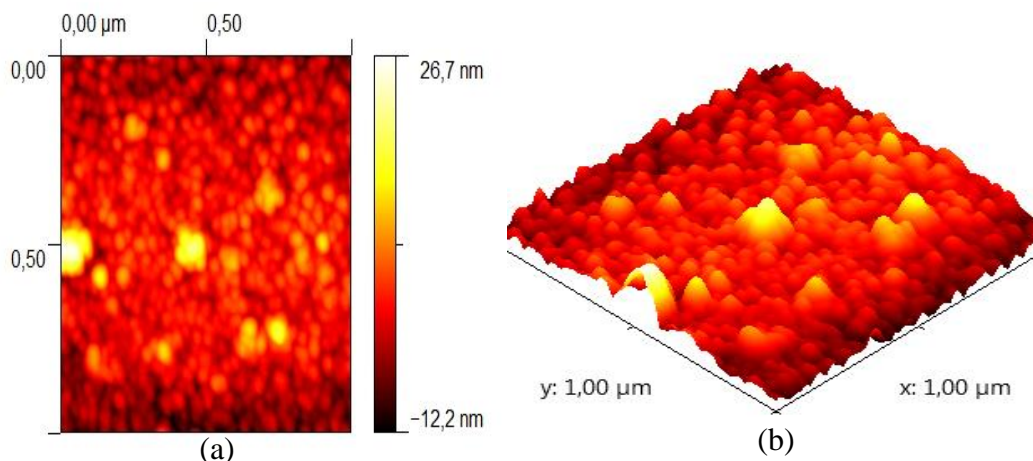


Figure 4.18. AFM images of CZT thin films deposited at $T_s=200^\circ\text{C}$ (as grown) on glass (a) -12.2;+26.7 nm in two dimensions, (b) 1 μm x 1 μm in three dimensions.

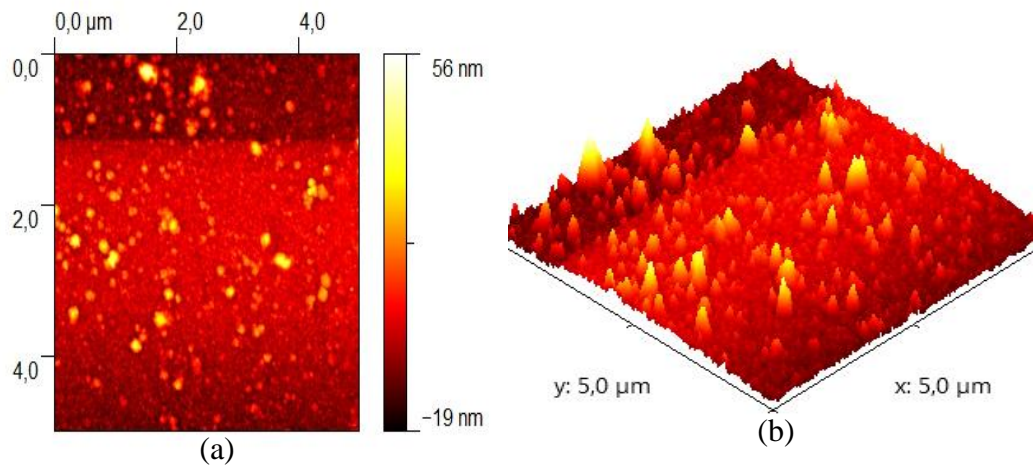


Figure 4.19. AFM images of CZT thin films deposited at $T_s=200^\circ\text{C}$ (as grown) on glass (a) -19;+56 nm in two dimensions, (b) $5\ \mu\text{m} \times 5\ \mu\text{m}$ in three dimensions.

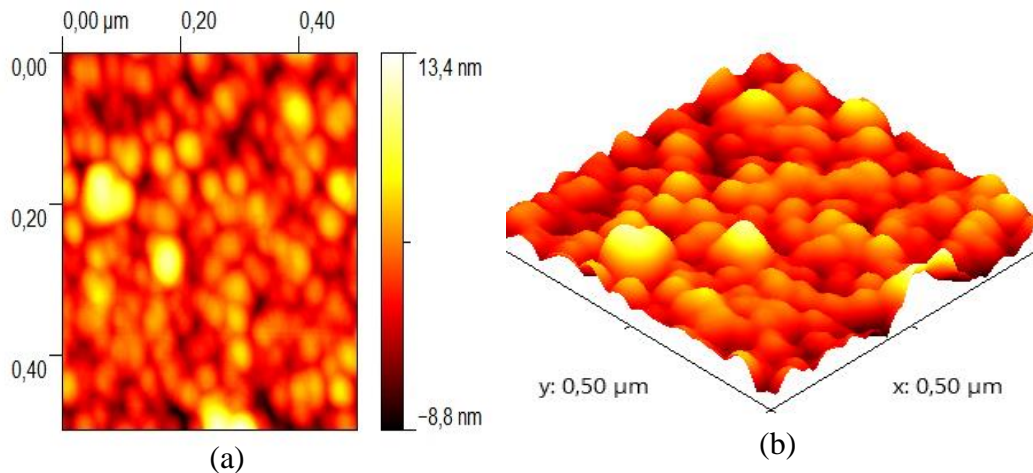


Figure 4.20. AFM images CZT thin films deposited at $T_s=200^\circ\text{C}$ (as grown) on glass (a) -8.8;+13.4 nm in two dimensions, (b) $0.50\ \mu\text{m} \times 0.50\ \mu\text{m}$ in three dimensions.

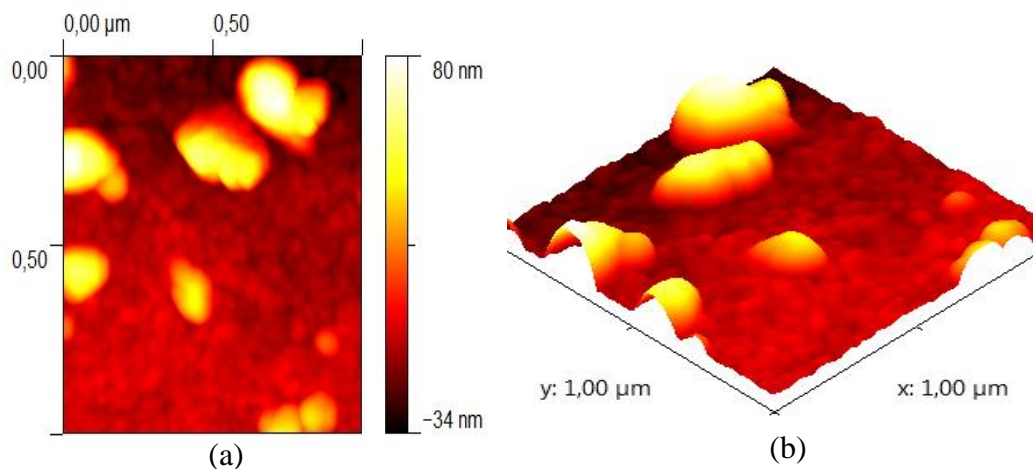


Figure 4.21. AFM images of CZT thin films deposited at $T_s=200^\circ\text{C}$ and at $T_a=300^\circ\text{C}$ on glass (a) -34;+80 nm in two dimensions, (b) $1\ \mu\text{m} \times 1\ \mu\text{m}$ in three dimensions.

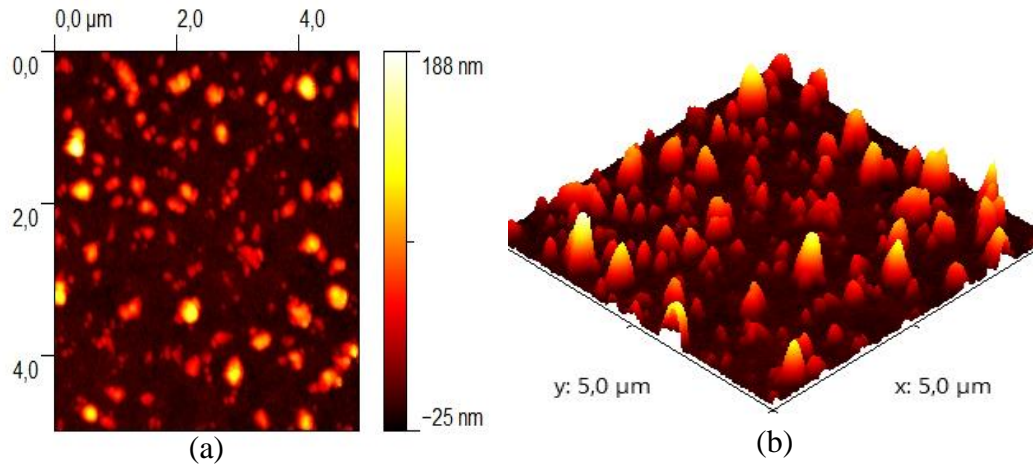


Figure 4.22. AFM images of CZT thin films deposited at $T_s=200^\circ\text{C}$ and at $T_a=300^\circ\text{C}$ on glass (a) -25;+188 nm in two dimensions, (b) $5\ \mu\text{m} \times 5\ \mu\text{m}$ in three dimensions.

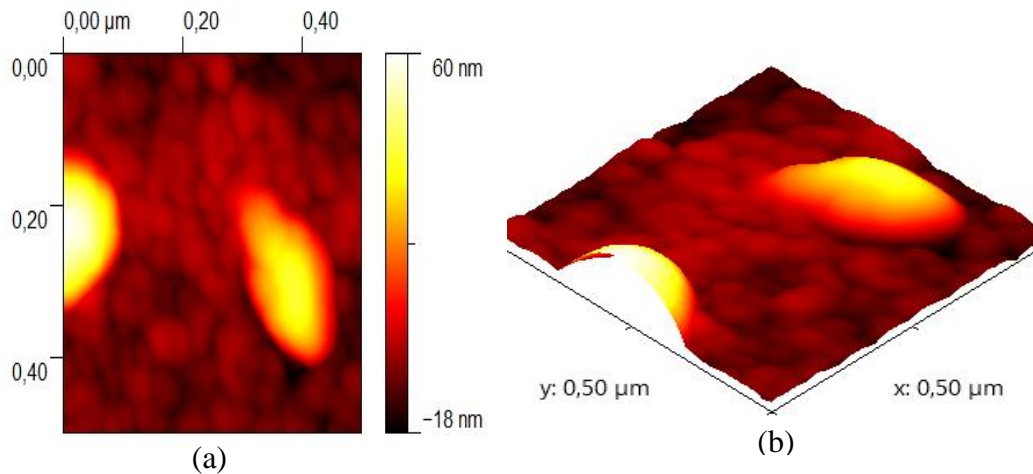


Figure 4.23. AFM images of CZT thin films deposited at $T_s=200^\circ\text{C}$ and at $T_a=300^\circ\text{C}$ on glass (a) -18;+60 nm in two dimensions, (b) $0.50\ \mu\text{m} \times 0.50\ \mu\text{m}$ in three dimensions.

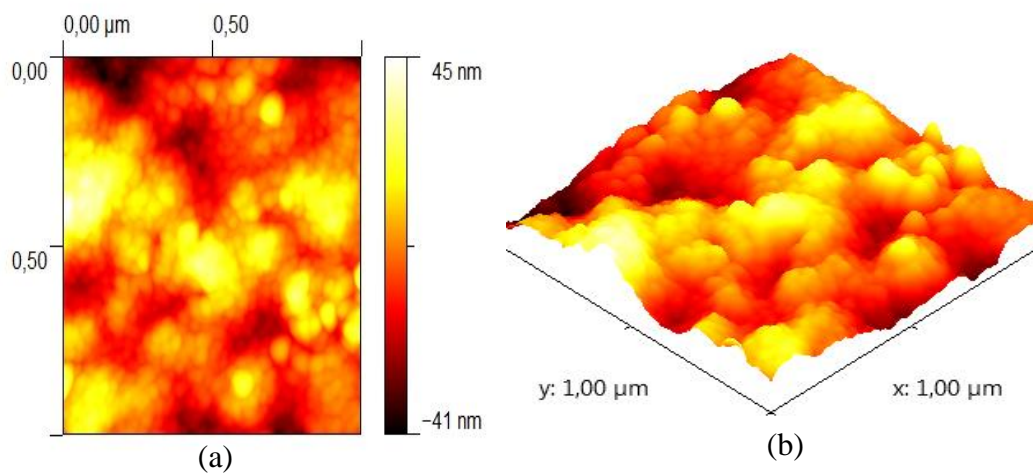


Figure 4.24. AFM images of CZT thin films deposited at $T_s=200^\circ\text{C}$ and at $T_a=450^\circ\text{C}$ on glass (a) -41;+45 nm in two dimensions, (b) $1\ \mu\text{m} \times 1\ \mu\text{m}$ in three dimensions.

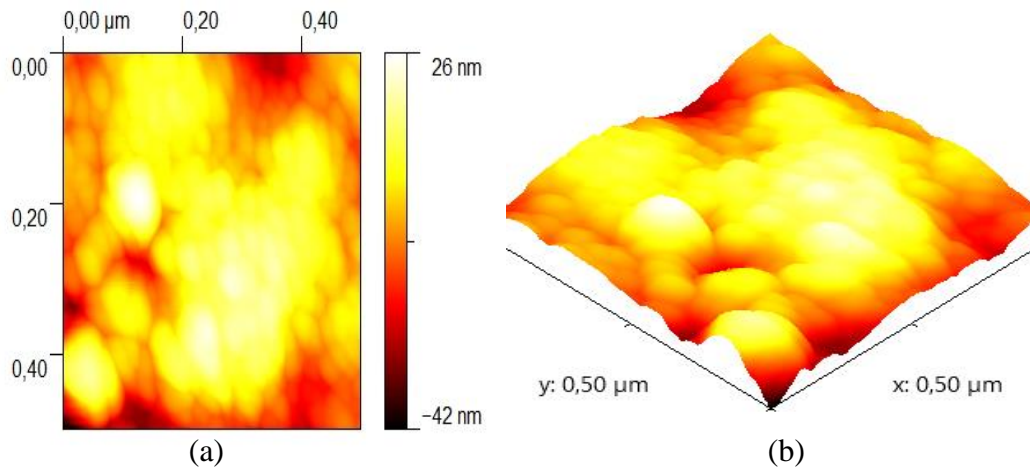


Figure 4.25. AFM images CZT thin films deposited at $T_s=200^\circ\text{C}$ and at $T_a=450^\circ\text{C}$ on glass (a) -42;+26 nm in two dimensions, (b) $0.50\ \mu\text{m} \times 0.50\ \mu\text{m}$ in three dimensions.

Figures 4.26-4.27 show the two and three dimensional AFM images of the sample deposited at 300°C . The surface is more uniform compared with as-deposited sample in Figures 4.16-4.17. It can be observed that the surface uniformity is getting worse in Figures 4.28-4.30 with increasing annealing temperature (at 300°C). On the otherhand, the surface uniformity of the films $T_s=300^\circ\text{C}$ and at $T_a=450^\circ\text{C}$ in Figures 4.31-4.33 is better.

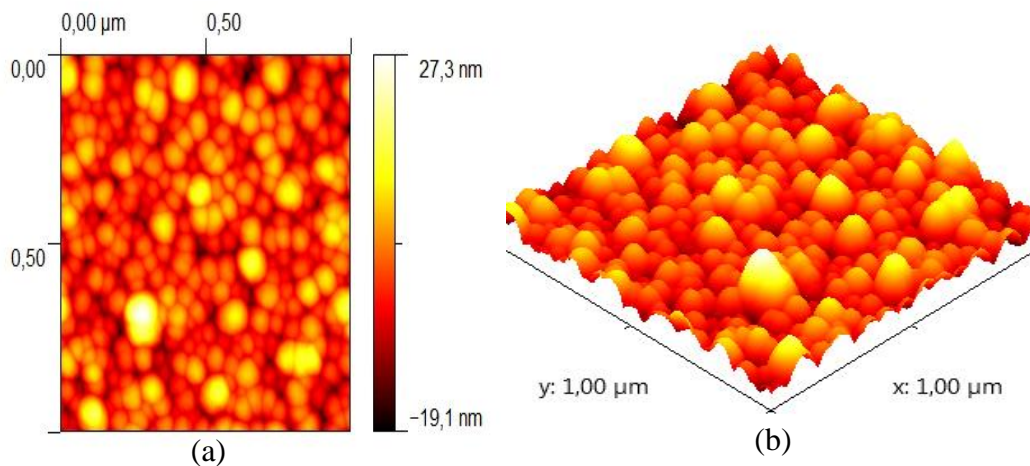


Figure 4.26. AFM images of CZT thin films deposited at $T_s=300^\circ\text{C}$ (as grown) on glass (a) -19.1;+27.3 nm in two dimensions, (b) $1\ \mu\text{m} \times 1\ \mu\text{m}$ in three dimensions.

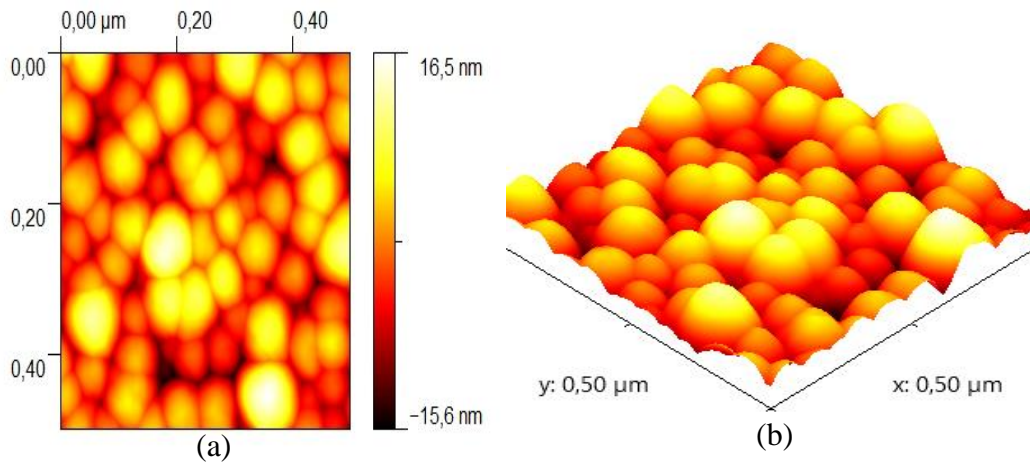


Figure 4.27. AFM images of CZT thin films deposited at $T_s=300^\circ\text{C}$ (as grown) on glass (a) -15.6;+16.5 nm in two dimensions, (b) $0.50\ \mu\text{m} \times 0.50\ \mu\text{m}$ in three dimensions.

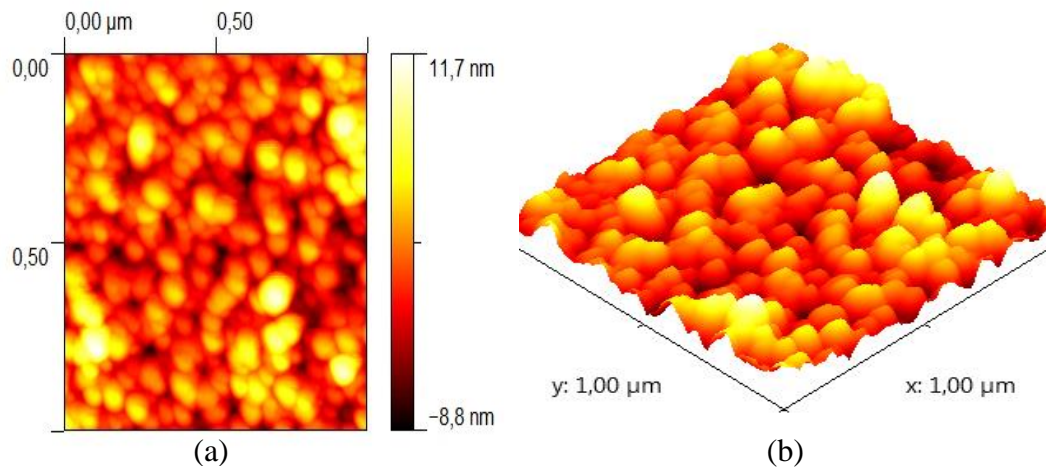


Figure 4.28. AFM images of CZT thin films deposited at $T_s=300^\circ\text{C}$ and at $T_a=300^\circ\text{C}$ on glass (a) -8.8;+11.7 nm in two dimensions, (b) $1\ \mu\text{m} \times 1\ \mu\text{m}$ in three dimensions.

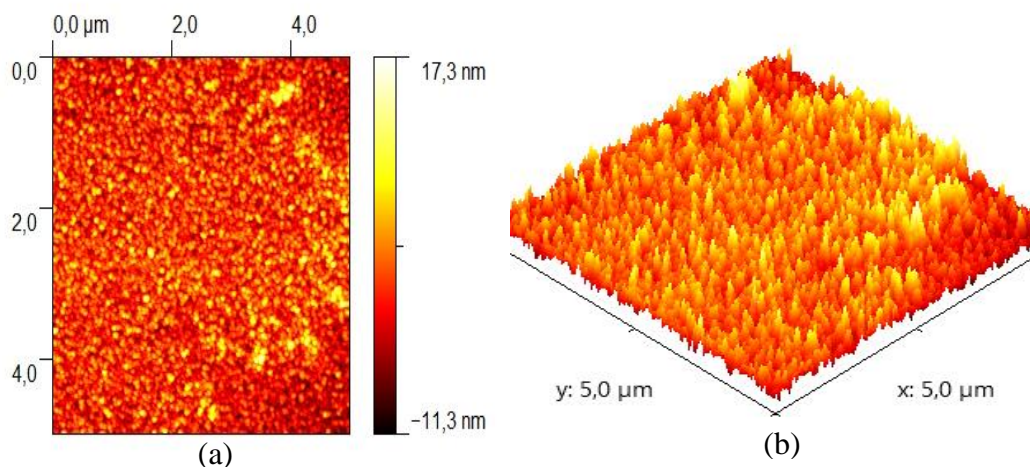


Figure 4.29. AFM images of CZT thin films deposited at $T_s=300^\circ\text{C}$ and at 300°C on glass (a) -11.3;+17.3 nm in two dimensions, (b) $5\ \mu\text{m} \times 5\ \mu\text{m}$ in three dimensions.

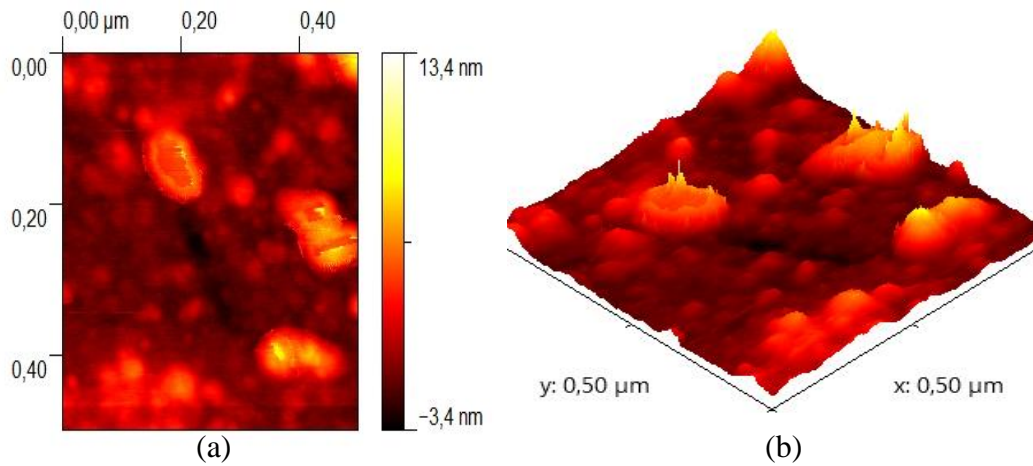


Figure 4.30. AFM images of CZT thin films deposited at $T_s=300^\circ\text{C}$ and at $T_a=300^\circ\text{C}$ on glass (a) -8.4;+8.6 nm in two dimensions, (b) $0.50\ \mu\text{m} \times 0.50\ \mu\text{m}$ in three dimensions.

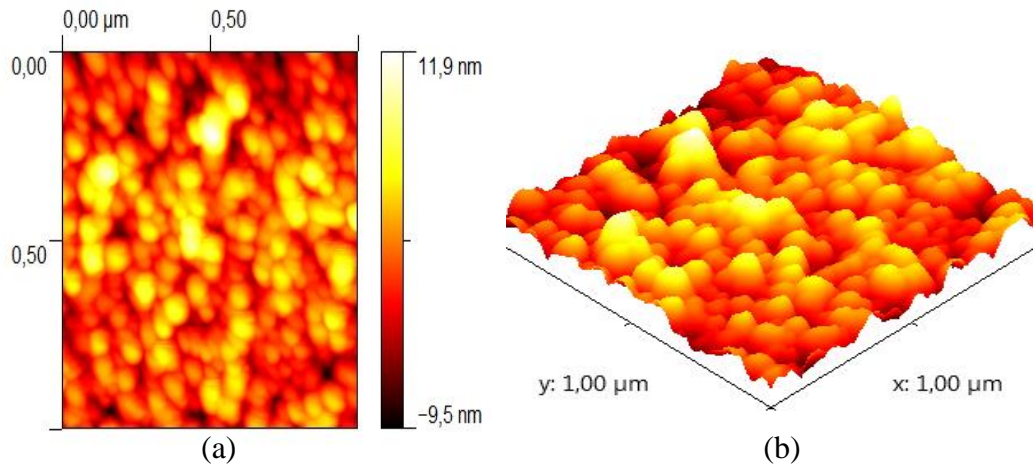


Figure 4.31. AFM images of CZT thin films deposited at $T_s=300^\circ\text{C}$ and at $T_a=450^\circ\text{C}$ on glass (a) -9.5;+11.9 nm in two dimensions, (b) $1\ \mu\text{m} \times 1\ \mu\text{m}$ in three dimensions.

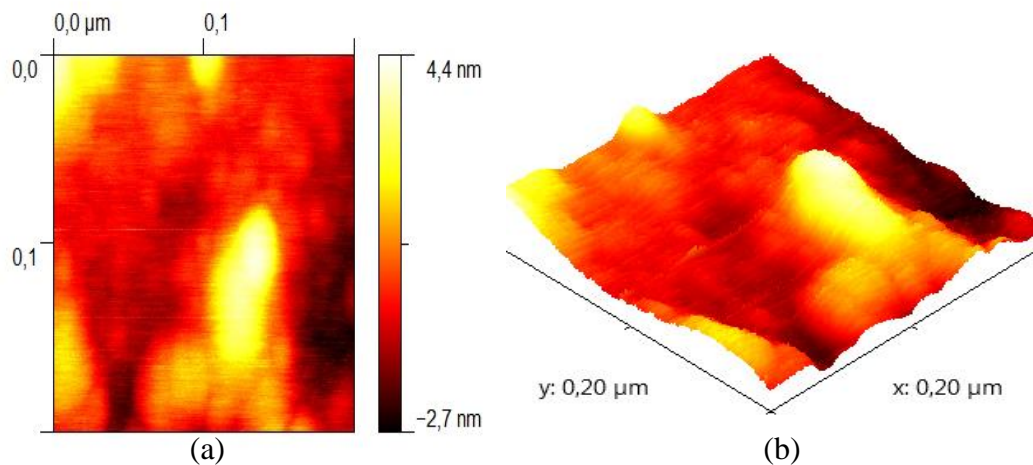


Figure 4.32. AFM images of CZT thin films deposited at $T_s=300^\circ\text{C}$ and at $T_a=450^\circ\text{C}$ on glass (a) -2.7;+4.4 nm in two dimensions, (b) $0.20\ \mu\text{m} \times 0.20\ \mu\text{m}$ in three dimensions.

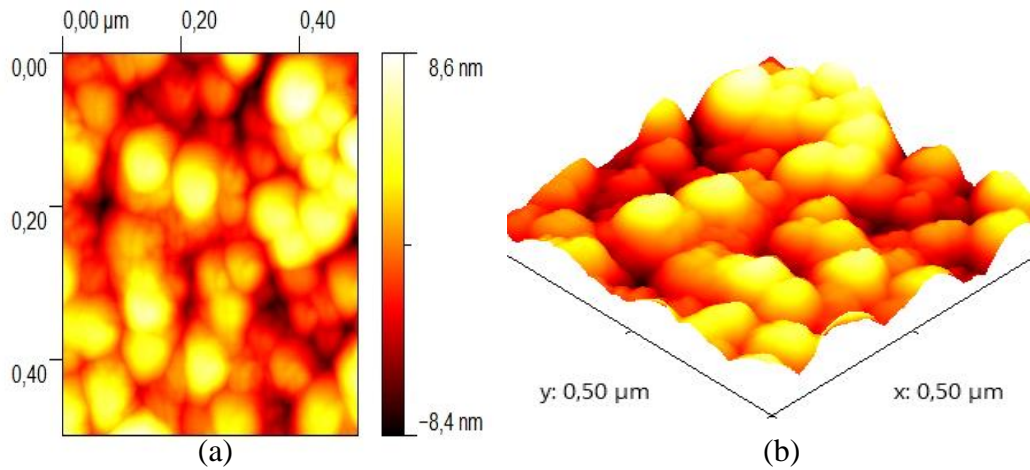


Figure 4.33. AFM images of CZT thin films deposited at $T_s=300^\circ\text{C}$ and at $T_a=450^\circ\text{C}$ on glass (a) -3.4;+13.4 nm in two dimensions, (b) $0.50\ \mu\text{m} \times 0.50\ \mu\text{m}$ in three dimensions.

The images of CZT thin films deposited at $T_s=400^\circ\text{C}$ (as grown) in Figures 4.34-4.35 have better surface uniformity than as-grown and at sputtering temperature of 300°C . So, the uniformity is becoming better with compared to Figures 4.26-4.27. However, the surface of sample forms a hillock structure and maximum heights.

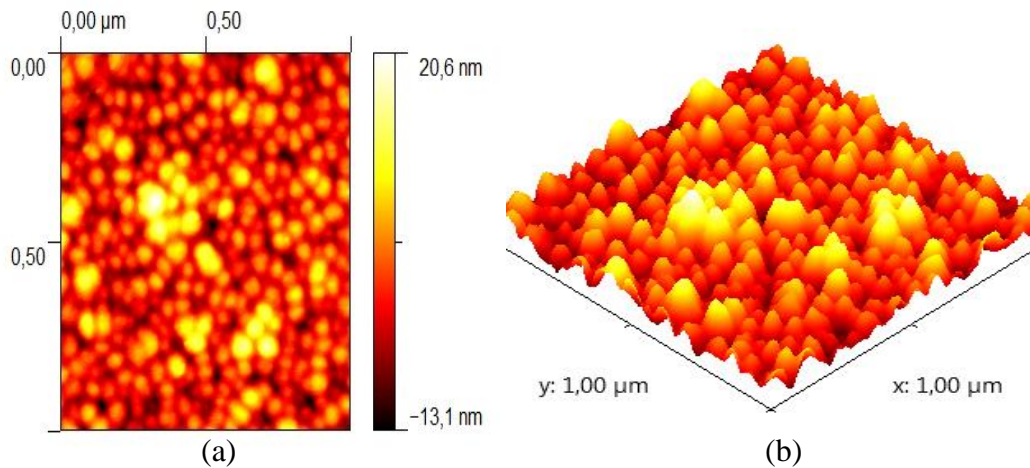


Figure 4.34. AFM images of CZT thin films deposited at $T_s=400^\circ\text{C}$ (as grown) on glass (a) -13.1;+20.6 nm in two dimensions, (b) $1\ \mu\text{m} * 1\ \mu\text{m}$ in three dimensions.

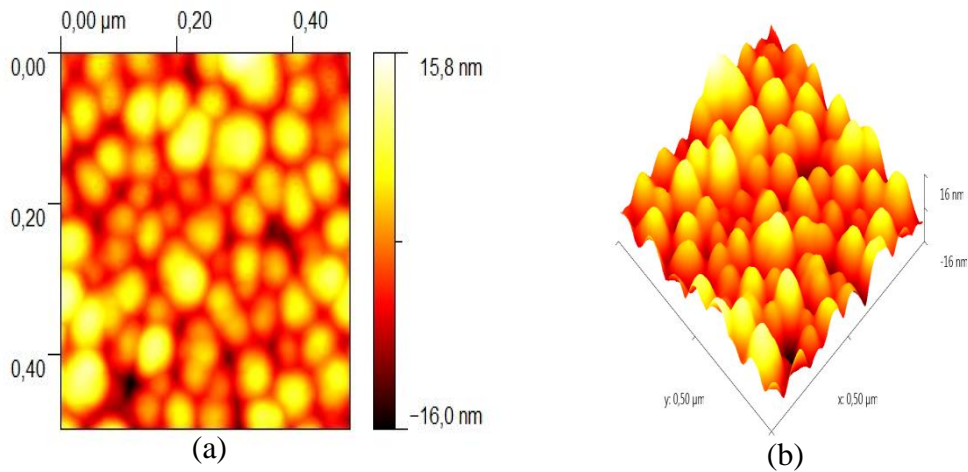


Figure 4.35. AFM images of CZT thin films deposited at $T_s=400^\circ\text{C}$ (as grown) on glass (a) -16;+15.8 nm in two dimensions, (b) $0.50\ \mu\text{m} \times 0.50\ \mu\text{m}$ in three dimensions.

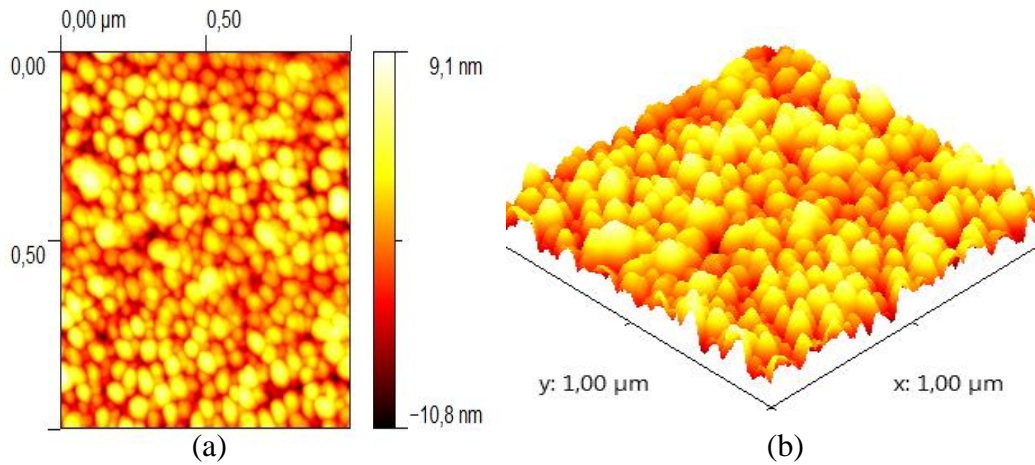


Figure 4.36. AFM images of CZT thin films deposited at $T_s=400^\circ\text{C}$ and at $T_a=300^\circ\text{C}$ on glass (a) -10.8;+9.1 nm in two dimensions, (b) $1\ \mu\text{m} \times 1\ \mu\text{m}$ in three dimensions.

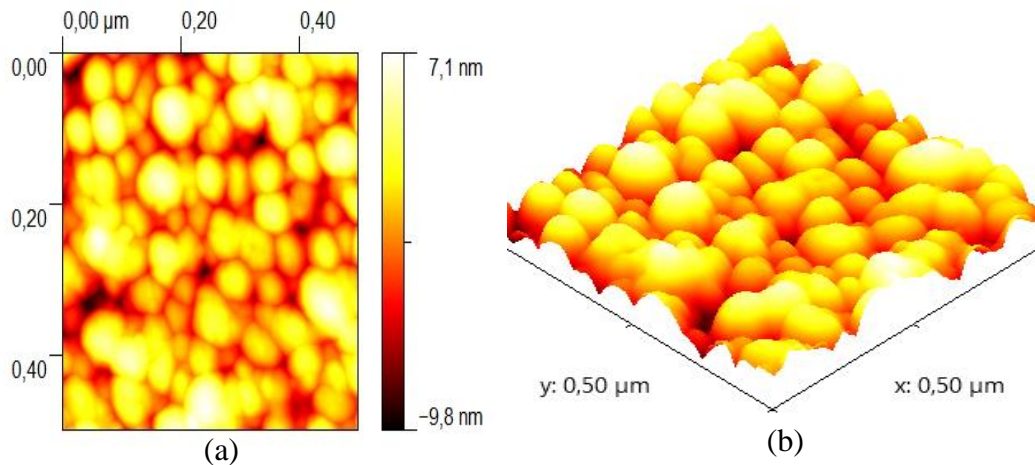


Figure 4.37. AFM images of CZT thin films deposited at $T_s=400^\circ\text{C}$ and at $T_a=300^\circ\text{C}$ on glass (a) -9.8;+7.1 nm in two dimensions, (b) $0.50\ \mu\text{m} \times 0.50\ \mu\text{m}$ in three dimensions.

Figures 4.38-4.40 demonstrate AFM images of CZT thin films deposited at 400°C and annealed at 450°C on glass. It can be seen from Figures 4.38-4.40 that the surface uniformity is getting the best with increasing at T_a .

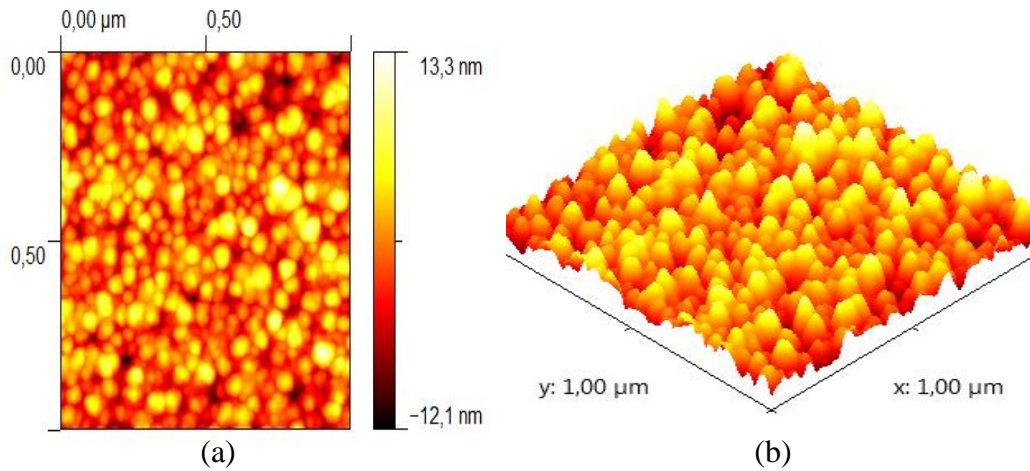


Figure 4.38. AFM images of CZT thin films deposited at $T_s=400^\circ\text{C}$ and at $T_a=450^\circ\text{C}$ on glass (a) image -12.1;+13.3 nm in two dimensions, (b) image of sample with 1 μm x 1 μm in three dimensions.

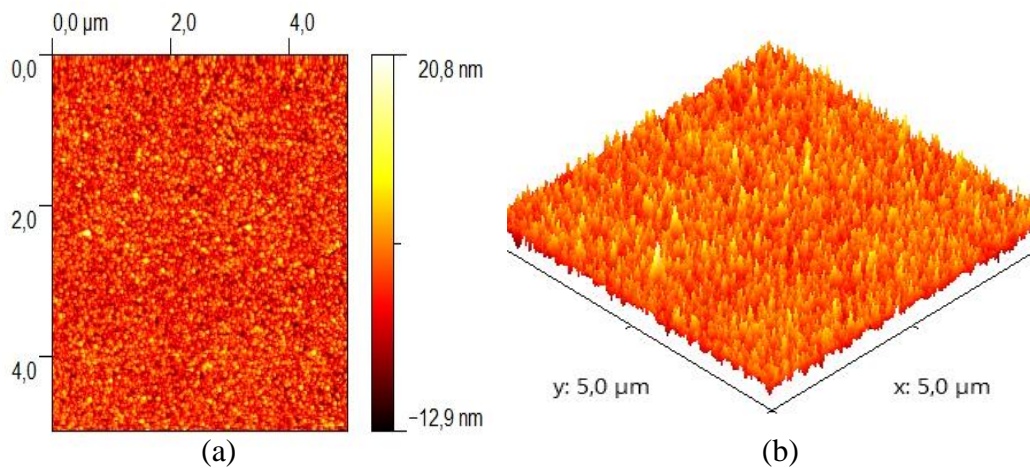


Figure 4.39. AFM images of CZT thin films deposited at $T_s=400^\circ\text{C}$ and at $T_a=450^\circ\text{C}$ 450°C on glass (a) -12.9;+20.8 nm in two dimensions, (b) 5 μm x 5 μm in three dimensions.

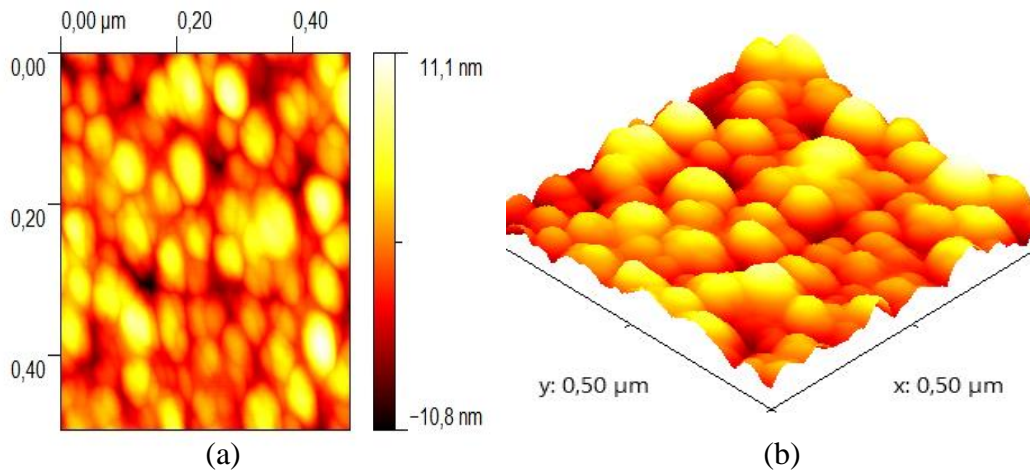


Figure 4.40. AFM images of CZT thin films deposited at $T_s=400^\circ\text{C}$ and at $T_a=450^\circ\text{C}$ on glass (a) $-10.8; +11.1$ nm in two dimensions, (b) $0.50\ \mu\text{m} \times 0.50\ \mu\text{m}$ in three dimensions.

For the general view of the obtained AFM measurements, it is observed that the grain boundaries are not clear on the surface of the film deposited at 200°C as seen from the micrographs. As the sputtering temperature increases, elliptical grains with defined boundaries are exhibited the CZT films and this films are uniform. In addition, the AFM measurements of the films determined different parameters like grain size, root-mean-square (RMS) roughness, skewness and kurtosis are given in Table 4.4. The RMS roughness of sample is decreasing with increasing at sputtering temperature. Therefore, the surfaces are getting dense and smooth at higher sputtering temperature. The grain size of the fabricated films found to be greater than calculated ones by Scherrer method. This ambiguity can be ascribed to the fact that AFM measurements result from coalition of the particles while an average crystallite size is given XRD. Nevertheless, from two different methods enhance with sputtering temperature was obtained the distribution of the grain size. Therefore, all the obtained results are in agreement with each other.

Skewness and kurtosis are important parameters to investigate surface height symmetry of the fabricated films. Skewness is non-dimensional quantity to specify the symmetry of the variation of a surface about its mean plane which is characteristically appreciated in terms of positive or negative skewness. The suggested skewness is zero for ideal film structure, showing that distribution of data around the mean data plane. The positive values of skewness means surface is consisted of sharp spike, while negative values representing small dip pit surface

morphology. On the other hand, kurtosis is also a zero dimensional quantity used to appreciate the form of surface about a central mean. Gaussian distribution is expected to have a kurtosis of 3.0. Less kurtosis values than 3 from Table 4.4 indicates that surface has a well spread out distribution while surface is centrally distributed kurtosis value is greater than 3. As in Table 4.4, skewness values are positive and all kurtosis values are very close to 3 for samples under study. However, among all samples, the surface of the sample deposited at 400°C was found to be centrally distributed and consisted with sharp peaks, shows to have the convenient characteristics for technological applications.

Table 4.4. Some parameters of CZT films deposited at various sputtering temperatures.

Ts (°C)	Lattice constant of CTZ (Å)	Zn Concentration Value XRD (x)	Grain Size- XRD (nm)	Grain Size- AFM (nm)	RMS Roughness (nm)	Skewness	Kurtosis
200 °C	6.43	0.14	6.5	11.15	10.9	0.108	2.72
300 °C	6.36	0.31	18.5	28.43	3.14	0.427	3.15
400 °C	6.31	0.45	49	56.68	3.05	0.112	2.97

The surface is more uniform and the surface RMS has decreased remarkably at annealed samples compared with as-deposited patterns. The grains are more closed packed, and their size distribution has been reduced at sputtering temperature of 400°C at annealed 300°C. The number of hole like properties has been diminished and their peak valley distance and depth diminished as well as might be seen by post deposition annealing at 300°C. Conversely, for the pattern annealed at 450°C, even though most part of the surface is like to at 300°C. Moreover the grain boundaries are not conspicuous as that of the pattern annealed at 300°C. The number and depth of the hole like properties have been enlarged. Hence, the film deposited at sputtering temperature of 400°C and next annealed at 450°C has a surface with good uniformity and remarkably low RMS roughness value. These features would be a well candidate for further film preparation in tools for solar cells and γ -ray detectors.

4.2.3 Chemical Composition Analysis

The EDX or EDS measurements are investigated the chemical composition of source and deposited CZT thin films. Figures 4.41-4.50 show the all obtained results.

Typical EDS spectra were obtained from samples grown at 0-400°C sputtering temperatures and annealed at 0, 300, and 450°C temperatures. In this study, another method which is used to investigate band gap of CZT thin films is the EDX. Firstly, atomic weight of Cd and Zn in the CZT composition is found from the obtained EDS measurements and then x value were calculated.

The EDX is measured the composition at depth functioned at acceleration energy by since the incident electron-beam energy is depended on the range of electron penetration. An electron beam with relatively 20 kV was chosen for the deep layers. The sputtering temperature is varied from 200 to 400°C. It was also observed that there is an atomic percentage of irregular Zn increased at 200°C sputtering temperatures with increasing of annealing temperature when the annealing temperature varies from 0 to 450°C. However, at 300°C, RF sputtering temperature when annealing temperature is increased the atomic percentage of Zn decreases. The increase of annealing temperature to 400°C RF sputtering temperature was also improved with atomic percentage of Zn. The change of the temperature RF sputtering and annealing is changed with the atomic percentages of Cd and Te as seen in the table 4.5. Therefore, the compositional changes obtained from Vegard's law in the CZT are supported by EDX measurements. Additionally, the changes in the peak boarding and crystallite size may also be a result of compositional changes on the ternary alloying. The other obtained impurity atoms i.e. Au, Pd, and Mg could be come from the sample holder or inert environment of the EDX devices and samples surfaces localized by experimental conditions.

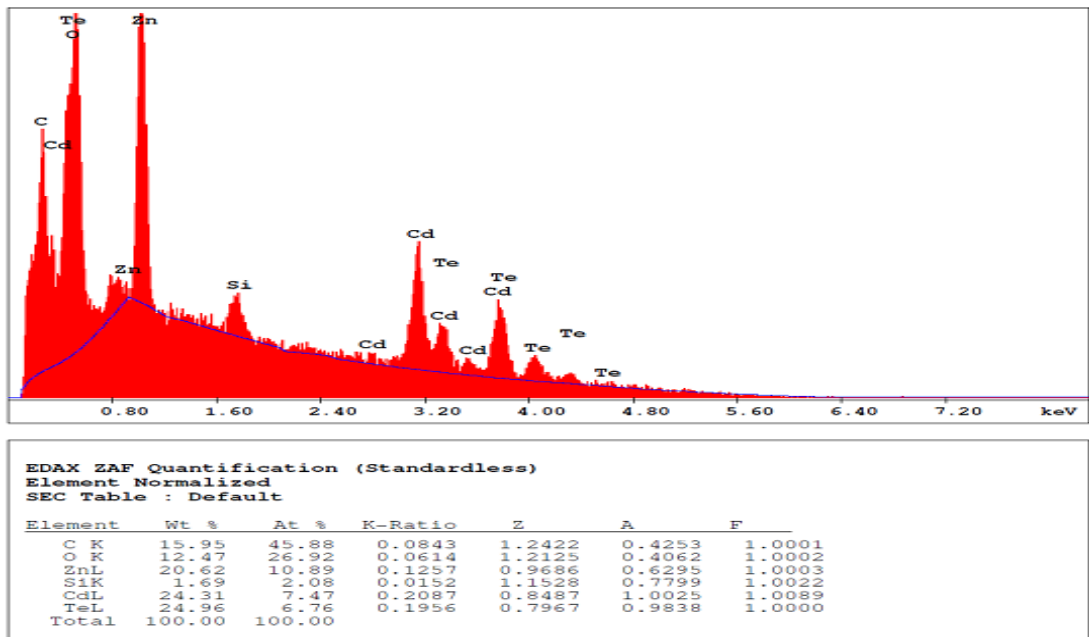


Figure 4.41. EDX spectra of CZT thin films as grown.

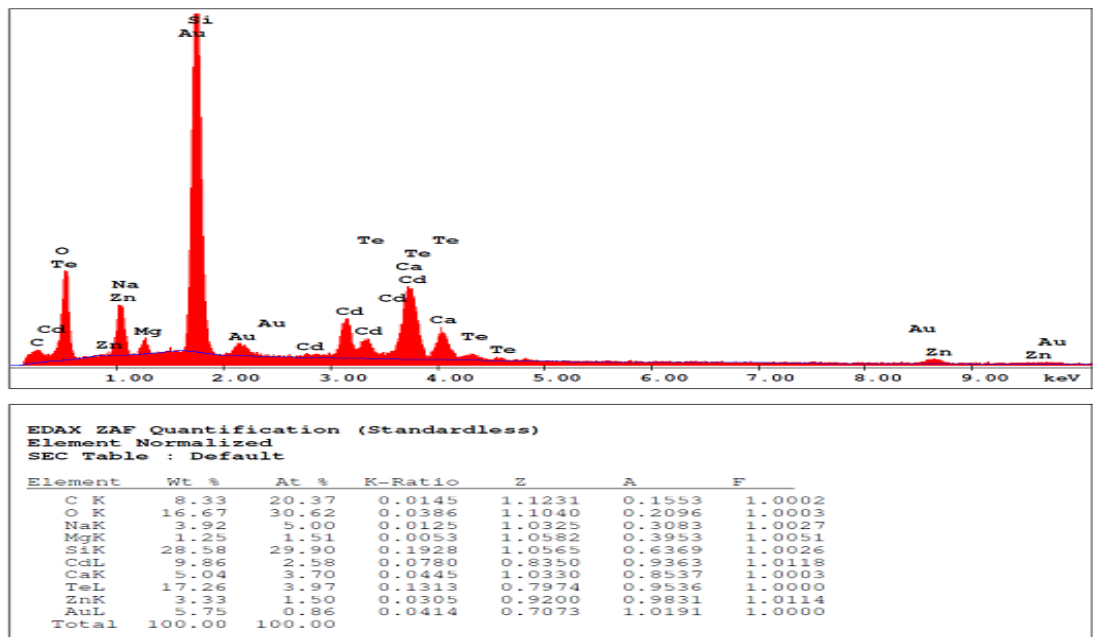


Figure 4.42. EDX spectra of CZT thin films with $T_s=200^\circ\text{C}$ (as-grown).

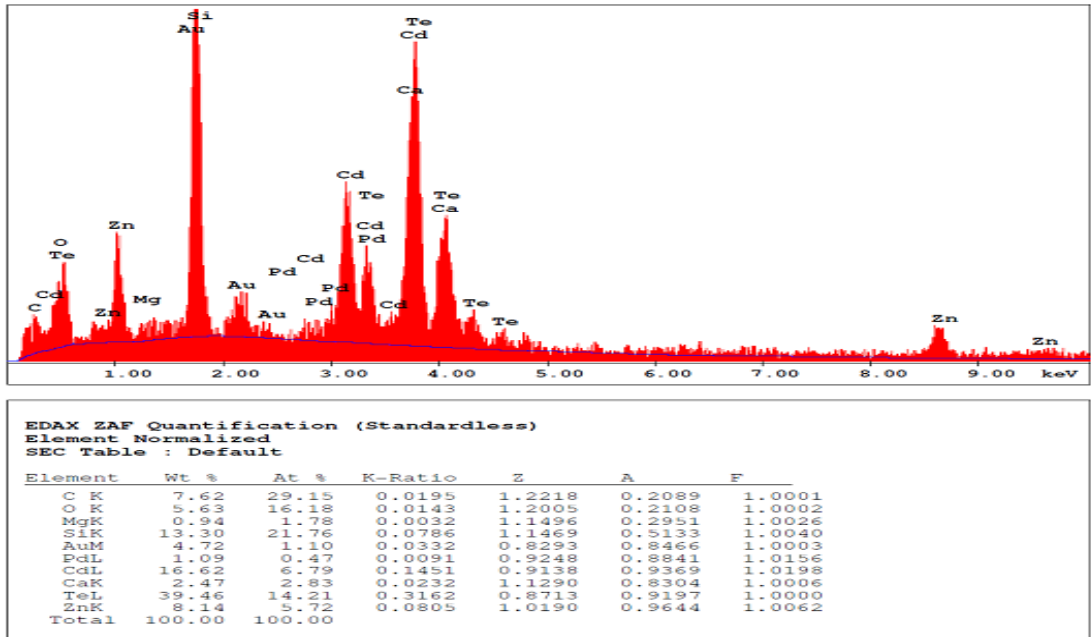


Figure 4.43. EDX spectra of CZT thin films with $T_s=200^\circ\text{C}$ and $T_a=300^\circ\text{C}$.

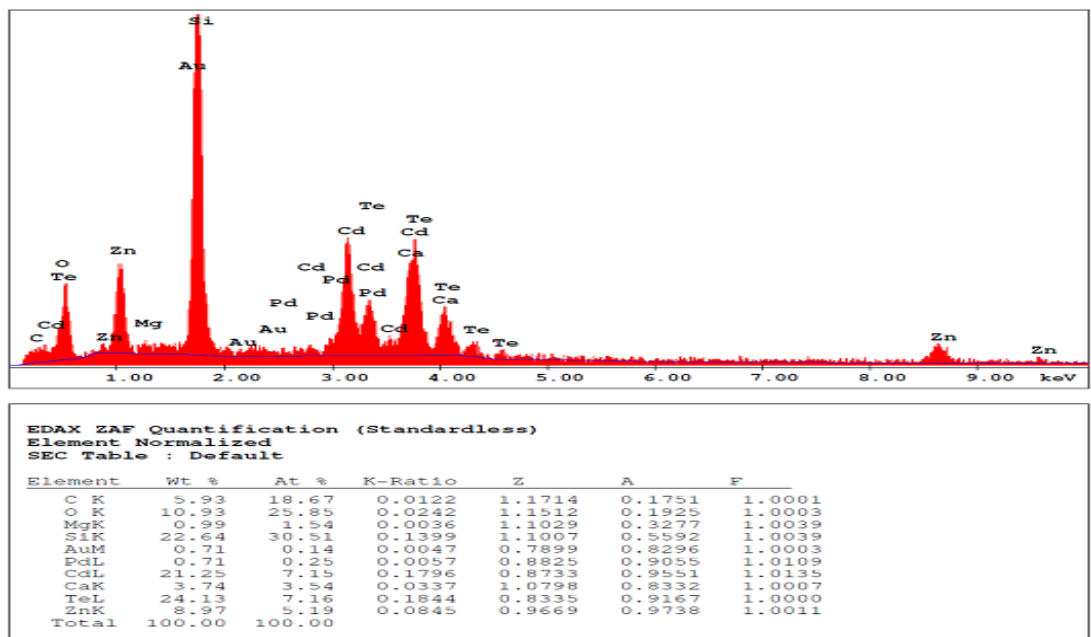


Figure 4.44. EDX spectra of CZT thin films with $T_s=200^\circ\text{C}$ and $T_a=450^\circ\text{C}$.

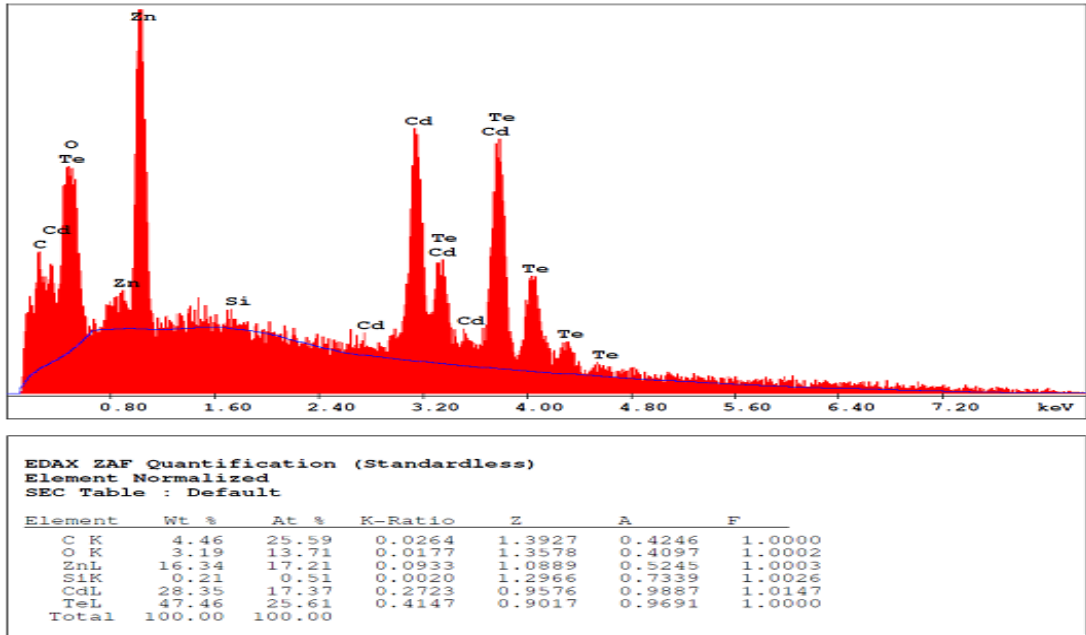


Figure 4.45. EDX spectra of CZT thin films with $T_s=300^\circ\text{C}$ (as-grown).

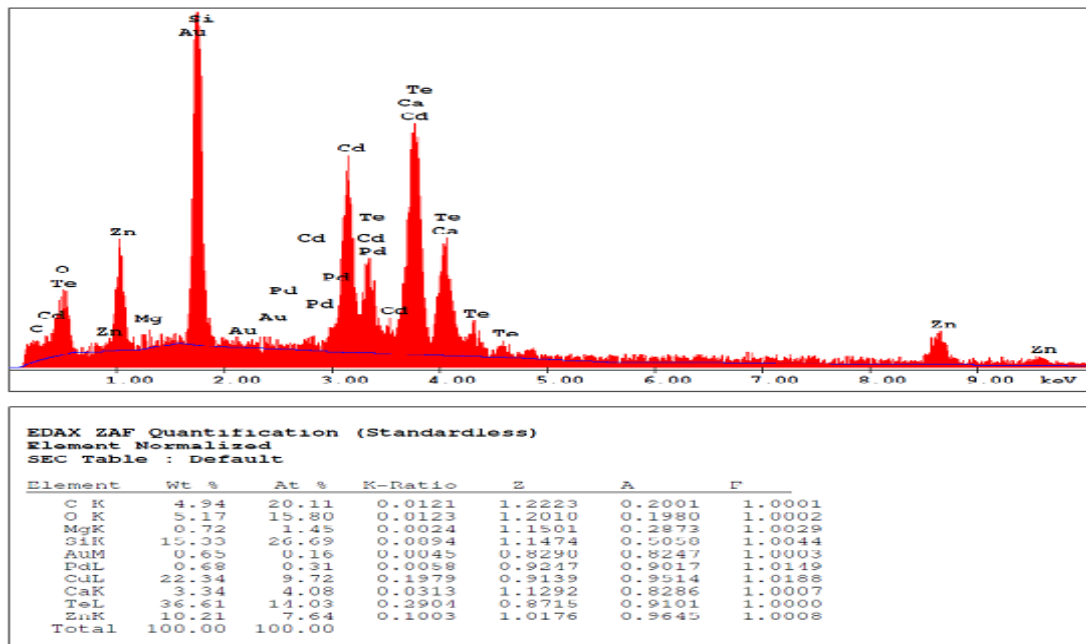


Figure 4.46. EDX spectra of CZT thin films with $T_s=300^\circ\text{C}$ and $T_a=300^\circ\text{C}$.

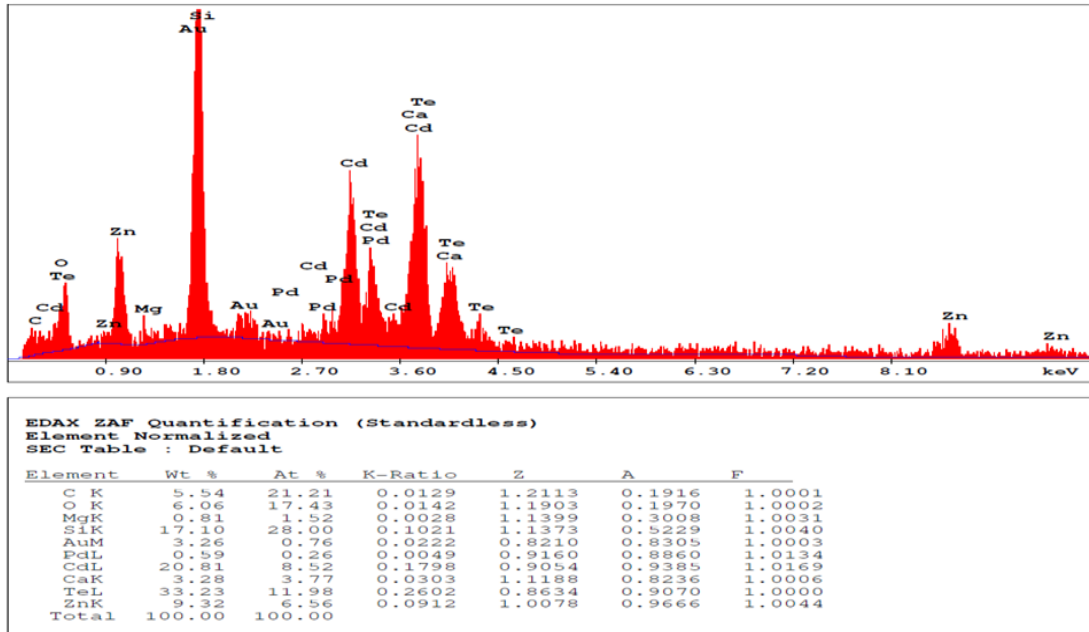


Figure 4.47. EDX spectra of CZT thin films with $T_s=300^\circ\text{C}$ and $T_a=450^\circ\text{C}$.

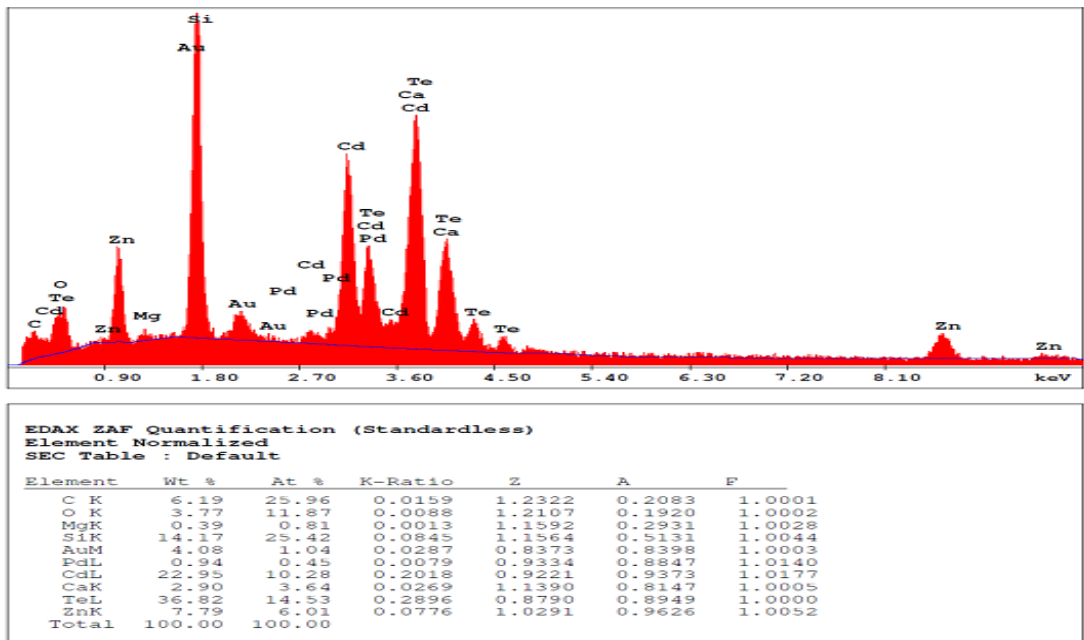


Figure 4.48. EDX spectra of CZT thin films with $T_s=400^\circ\text{C}$ (as-grown).

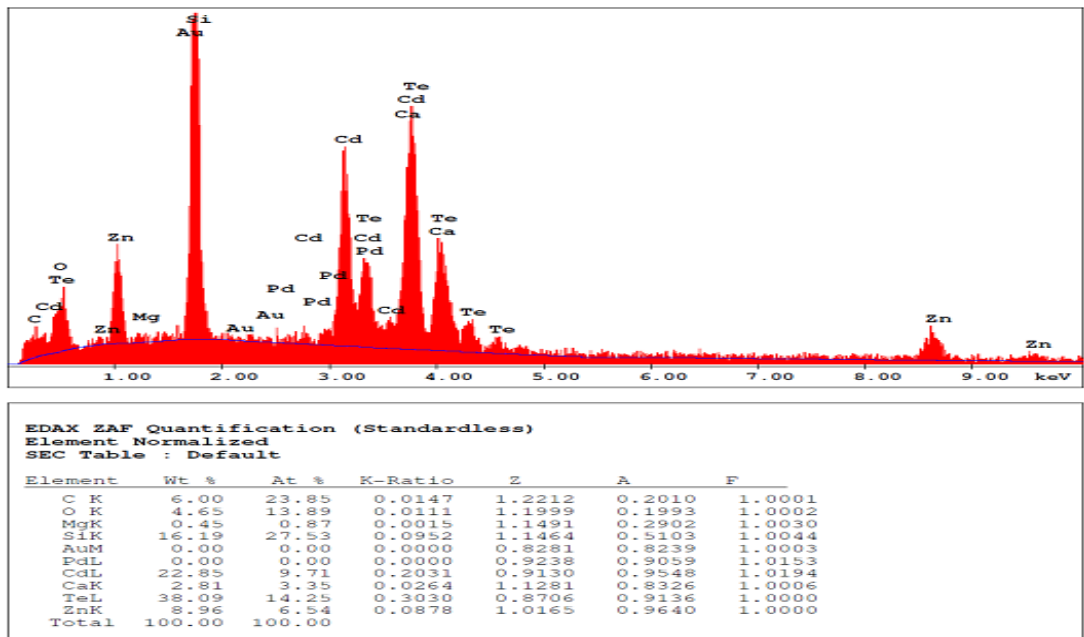


Figure 4.49. EDX spectra of CZT thin films with $T_s=400^\circ\text{C}$ and $T_a=300^\circ\text{C}$.

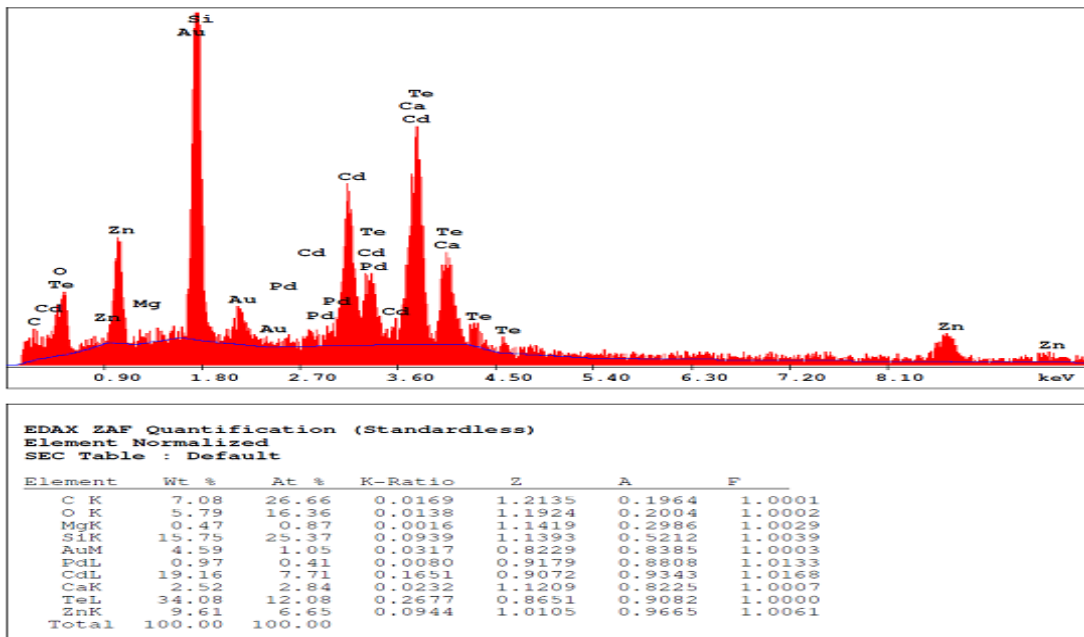


Figure 4.50. EDX spectra CZT thin films with $T_s=400^\circ\text{C}$ and $T_a=450^\circ\text{C}$.

Table 4.5. Atomic percentage (% value) of Cd; Zn; Te; in the compound found from EDX.

RF sputtering temperature °C	Annealing temperature °C	% value of Cd from EDX	% value of Zn from EDX	% value of Te from EDX	Summation of %Cd;Zn;Te in the compound
200	0	9.86	3.33	17.26	30.45
200	300	16.62	8.14	39.46	64.22
200	450	21.25	8.97	24.13	54.35
300	0	28.35	16.34	47.46	92.15
300	300	22.34	10.21	34.08	66.63
300	450	20.81	9.32	33.23	63.36
400	0	22.95	7.79	36.82	60.56
400	300	22.85	8.96	8.96	69.90
400	450	19.16	9.61	34.08	62.85

In order to calculate the x value the atomic weight percentage of Zn and Cd in the compound was investigated from the obtained EDS figures. The Table 4.5 gives all of these results. x can be calculated with the help of the following formula from each EDS measurements.

$$x = \frac{Zn}{Zn+Cd} \quad (4.11)$$

From Fig. 4.41. without any thermal process (as grown)

$$x = \frac{\text{Atomic Weight of Zn}}{\text{Atomic Weight of Zn} + \text{Atomic Weight of Cd}} = \frac{10.89}{10.89+7.47} = 0.593, \quad (4.12)$$

x can be computed from the other Figures then all of the x values can be found in the same way in the table 4.6. The summation of atomic percentage of Cd, Zn can see from the Figs. 4.41-4.40, Te was not 100%. Their rates are average 50-60% the others are Si(silicon), Mg,(magnesium), C(carbon), O(oxygen), and Na(sodium).

Table 4.6. x value calculation performs according to EDX measurements from the atomic weight of Cd and Zn.

RF sputtering temperature °C	Annealing temperature °C	Atomic Weight of Zn (%)	Atomic Weight of Cd (%)	x value from EDX $\left(x = \frac{Zn}{Zn+Cd}\right)$
200	0	1.50	2.58	0.433
200	300	5.72	6.79	0.445
200	450	5.19	7.15	0.495
300	0	17.21	17.37	0.498
300	300	7.64	9.72	0.432
300	450	6.56	5.52	0.492
400	0	6.01	10.28	0.423
400	300	6.54	9.71	0.398
400	450	6.65	7.71	0.463

When the EDS results are compared with those of obtained from XRD measurements, the x values acquired from the XRD analysis are smaller than those of EDS measurements. There are two fundamental factors which are responsible for this consequence. First one is related to the micro strains or local strains on the nano grains which consequences in the shift of XRD diffraction peaks causing different x values. Another factor is related to the formation of other zinc containing phases such as ZnO besides CZT phase. For instance, as grown samples by XRD data the value x between 0.3 and 0.45 have been obtained. On the other hand by EDS measurements are from 0.39 to 0.5. This homogeneity data concordance between XRD and EDS measurements would be same because the applied higher sputtering temperature. The augmentation of the kinetic energy of the sputtered particles can be lead to by this temperature. Then particles are able to immigrate to more appropriate lattice sites and assay their genuine band direction and length to acquire optimum bonding to the adjacent ones which are useful for nucleation and growth, and as a result increased crystallinity.

4.2.4 Compositional Analysis

XPS is used to observe the varieties in chemical compound and probable oxidation of each element on the surface and underlying layers, and to recognize the varieties in the stoichiometry of as deposited and annealed patterns. XPS depth profiling method have been analyzed the chemical bonding state and elemental composition of CZT films subjected to different sputtering temperature and similar post deposition annealing temperature of as grown, at 300 and 450°C. That is to say this technique accredited us to define films' the stoichiometry. Additionally the XPS spectra obtained at the first surfaces of the pattern is clearly shown Cd, Zn and Te. The typical peaks of absorbents are O and C owing to the hydrocarbons. The presence of oxides and contamination routinely scanned to establish the O1s and C1s.

The oxygen on surface corresponds to a surface influence since it seems that there is not existence of oxygen in the bulk. The tellurium is oxidized at the surface. That is the reason why the oxygen exists in the surface for all fabricated samples. It also observed that in the deeper levels, the concentration of oxygen decrease due to decline in the diffusion of oxygen into bulk structure of the CZT. In all states

studied XPS spectra of the films of different compositions deposited at various temperatures denoted the binding energies of the Cd(3d5/2 and 3d3/2), Zn(2p) and Te(3d5/2 and 3d3/2) levels. Figures 4.51-4.54 show XPS spectra of CZT thin film deposited on glass at 200°C and annealed at as grown for 25 cycle under 2500 volt. Figures 4.52, 4.53 and 4.54 show Cd, Zn and Te alloy which can be found on the glass homogeneously up to certain depth. The binding energies of the Te(3d5/2 and 3d3/2) levels in Figure 4.52 were shown at 572 and 582.6 eV respectively. The 3d peaks of both Cd and Te are doublets reflecting the 3d5/2 and 3d3/2 spin orbit splitting. It has been exhibited that the splitting seen in the 3d peak of tellurium is owing to the existence of extreme tellurium. The binding energy of Zn2p3/2 was observed 1021.4 eV in Figure 4.53. From Figure 4.54 Cd(3d5/2 and 3d3/2) observed at 404.5 and 411.2 eV were associated with the peak energy levels respectively. Also the binding energy of Zn(2p3/2) was observed 1021.4 eV. As can be seen, the integrated intensity of all elements is almost the same and does not change by Ar sputtering for the as grown sample. Therefore it is implying that distribution of the atoms on the surface and underlying layers is homogeneous.

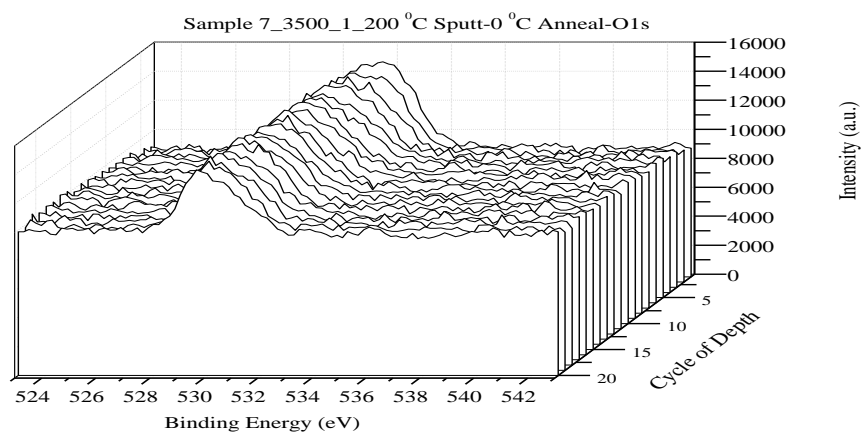


Figure 4.51. XPS spectra of O1s level in the CZT film deposited on glass at $T_s=200^\circ\text{C}$ (as grown) for 25 spectra.

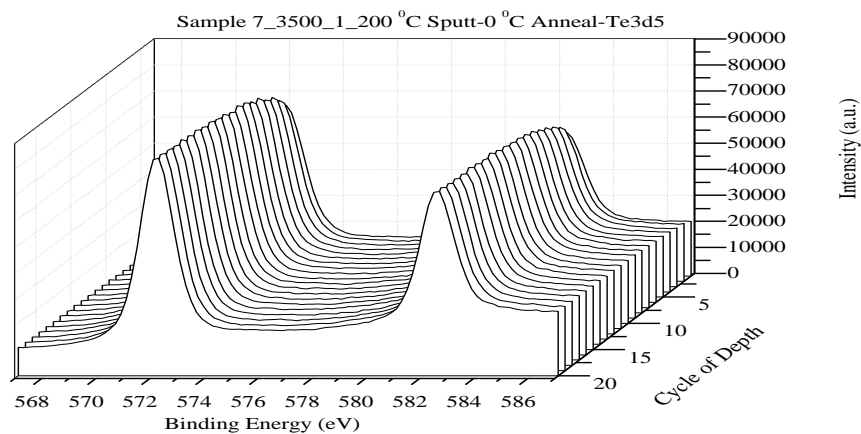


Figure 4.52. XPS spectra of Te3d5 level in the CZT film deposited on glass at $T_s=200^\circ\text{C}$ (as grown) for 25 spectra.

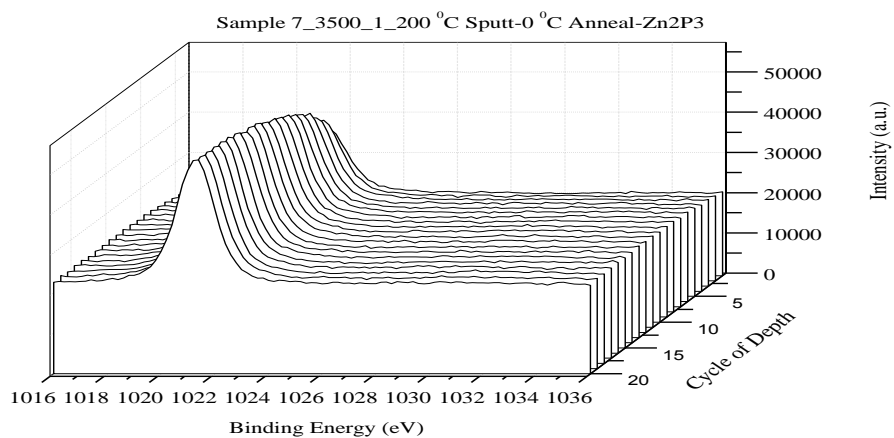


Figure 4.53. XPS spectra of Zn2p3 level in the CZT film deposited on glass at $T_s=200^\circ\text{C}$ (as grown) for 25 spectra.

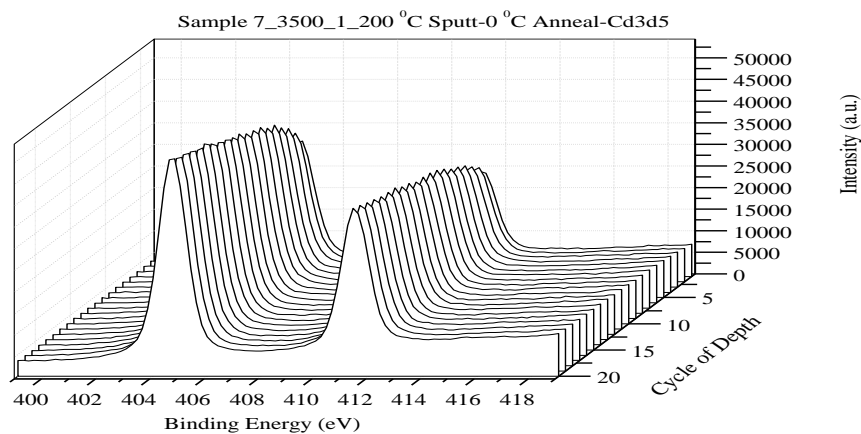


Figure 4.54. XPS spectra of Cd3d5 level in the CZT film deposited on glass at $T_s=200^\circ\text{C}$ (as grown) for 25 spectra.

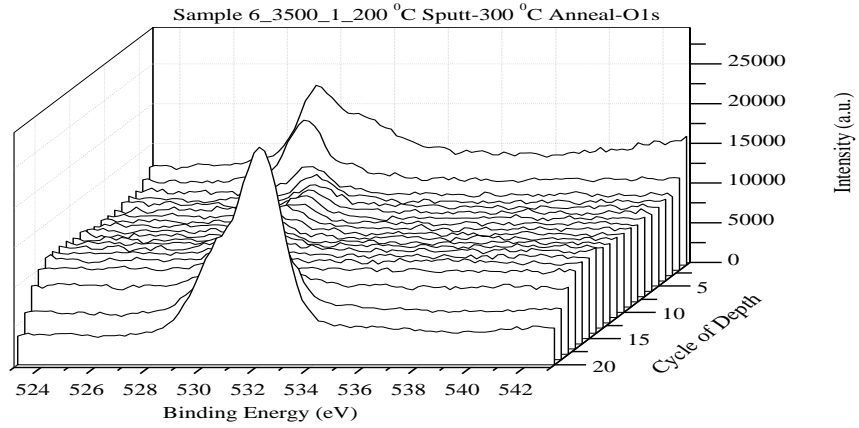


Figure 4.55. XPS spectra of O1s level in the CZT film deposited on glass at $T_s=200^\circ\text{C}$ and at $T_a=300^\circ\text{C}$ for 25 spectra.

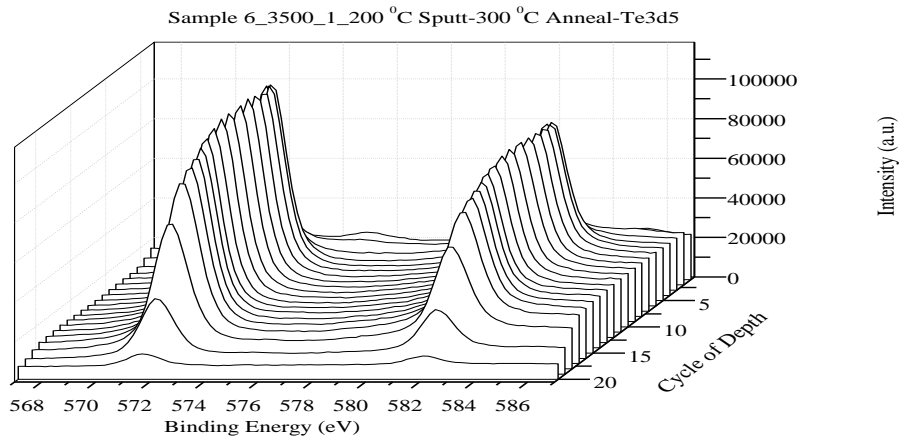


Figure 4.56. XPS spectra of Te3d5 level in the CZT film deposited on glass at $T_s=200^\circ\text{C}$ and at $T_a=300^\circ\text{C}$ for 25 spectra.

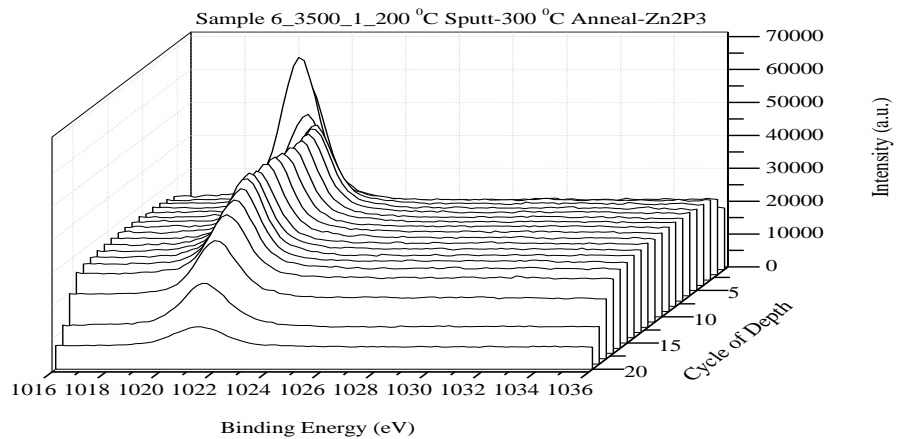


Figure 4.57. XPS spectra of Zn2p3 level respectively, in the CZT film deposited on glass at $T_s=200^\circ\text{C}$ and at $T_a=300^\circ\text{C}$ for 25 spectra.

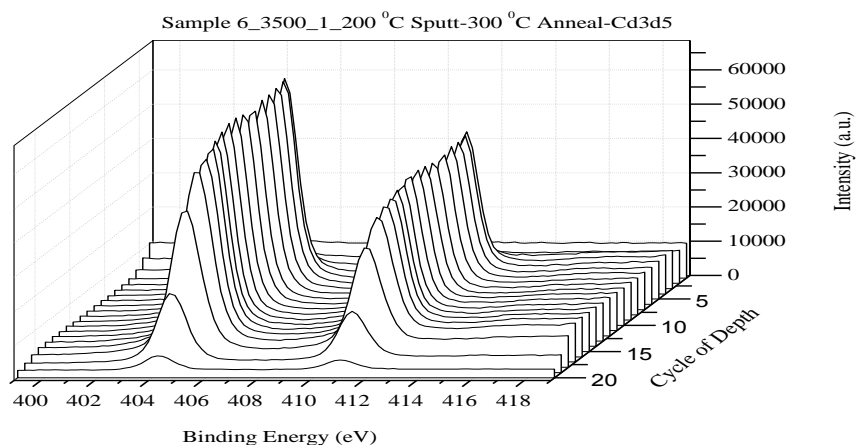


Figure 4.58. XPS spectra of Cd3d5 level in the CZT film deposited on glass at $T_s=200^\circ\text{C}$ and at $T_a=300^\circ\text{C}$ for 25 spectra.

The 25 spectra of XPS are shown in Figures 4.55-4.58 deposited on glass at 200°C and annealed at 300°C under 3500 volt. It has been observed in Figure 4.55 that the O concentration is high at the just surface and interface of the films. The oxidation at higher temperature of Te for surface and the glass wafers (SiO_2) are the basic reasons of this results observed in Figure 4.55. On the other hands, the Zn, Cd and Te concentration is almost remain constant up to certain deep. It seems that approximately the 20th cycle the CZT layer totally removed from the surface, hence the all film elements' concentration (Cd, Zn, Te) sharply decrease. The unacceptable rise in the O concertation after 20th cycle also supports this discussion. Briefly, the elemental distribution of the atoms on the film annealed at 300°C structure is also homogeneous.

Figures 4.59-4.70 show XPS spectra of CZT film deposited on glass at 400°C and annealed at as grown, 300°C , and 450°C respectively. Similar results obtained from previous XPS analysis were obtained for deposited thin films. The films homogeneity is good for all thin films annealed at various temperatures. The average integrated intensities of Zn, obtained from various annealing temperature for 450°C films, is slightly enhance with annealing temperatures. This behavior indicates that Zn concentration on the film composition increase with annealing temperatures. These results are in harmony with other results obtained from XRD and EDX.

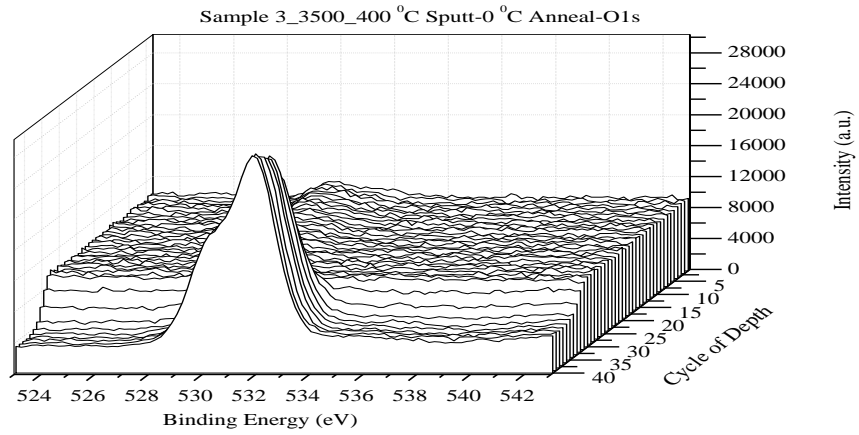


Figure 4.59. XPS spectra of O1s level in the CZT film deposited on glass at $T_s=400^\circ\text{C}$ (as grown) for 25 spectra.

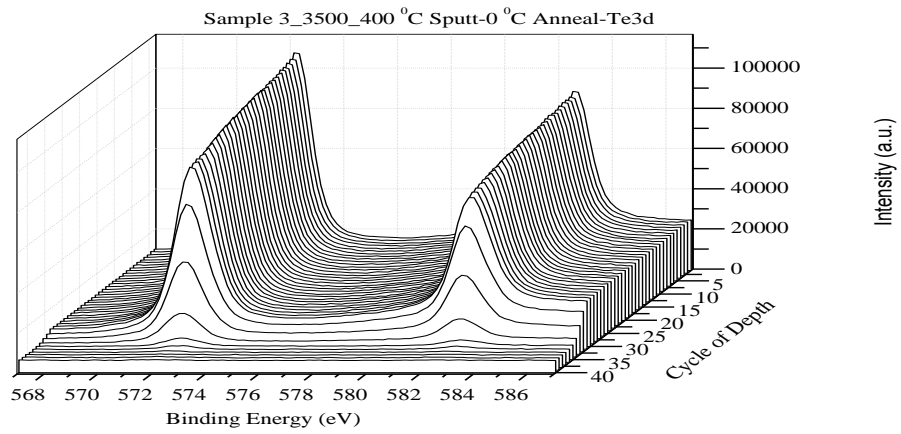


Figure 4.60. XPS spectra of Te3d5 level in the CZT film deposited on glass at $T_s=400^\circ\text{C}$ and as grown for 25 spectra.

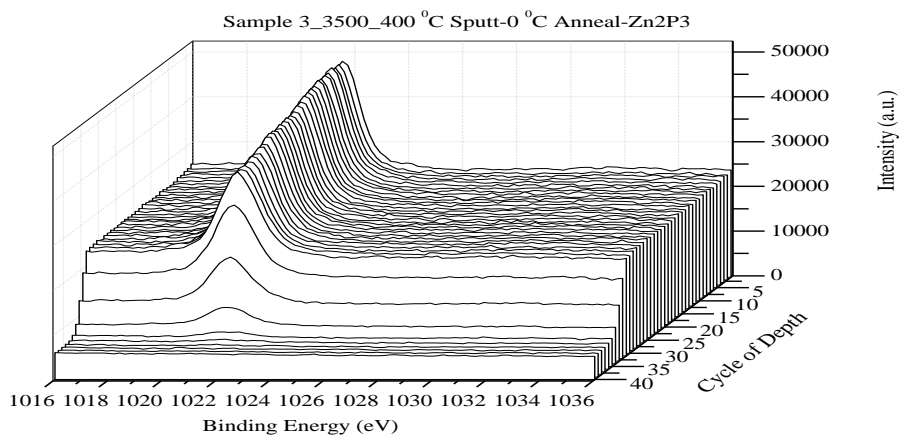


Figure 4.61. XPS spectra of Zn2p3 level in the CZT film deposited on glass at $T_s=400^\circ\text{C}$ (as grown) for 25 spectra.

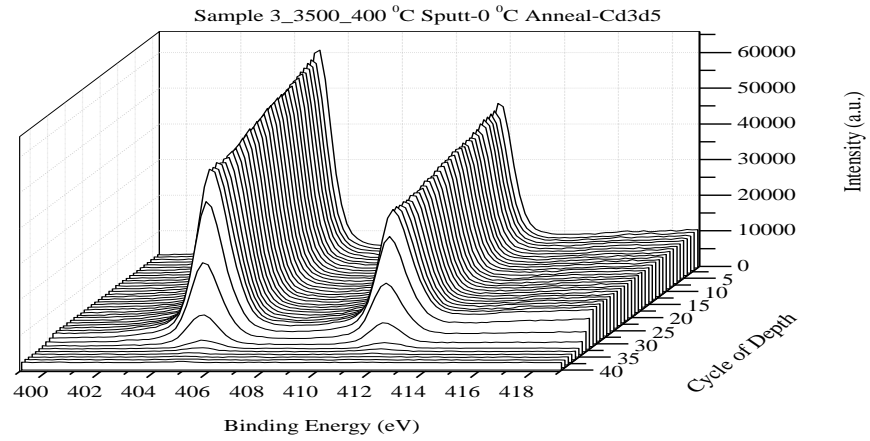


Figure 4.62. XPS spectra of Cd3d5 levels respectively, in the CZT film deposited on glass at $T_s=400^\circ\text{C}$ (as grown) for 25 spectra.

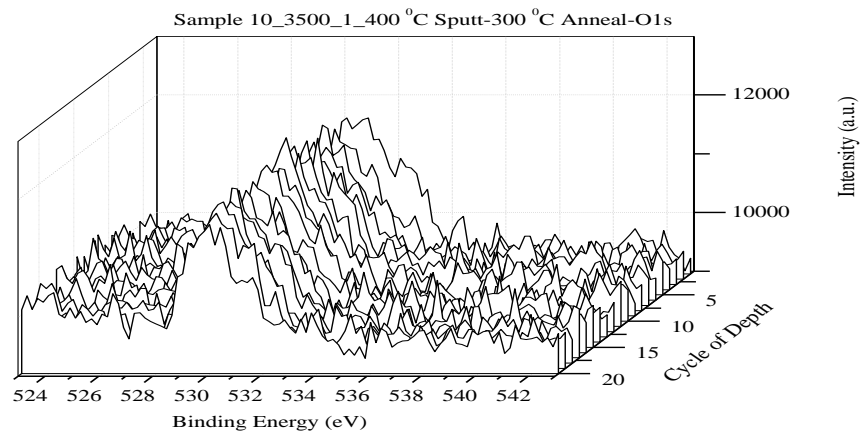


Figure 4.63. XPS spectra of O1s level in the CZT film deposited on glass at $T_s=400^\circ\text{C}$ and at $T_a=300^\circ\text{C}$ for 25 spectra.

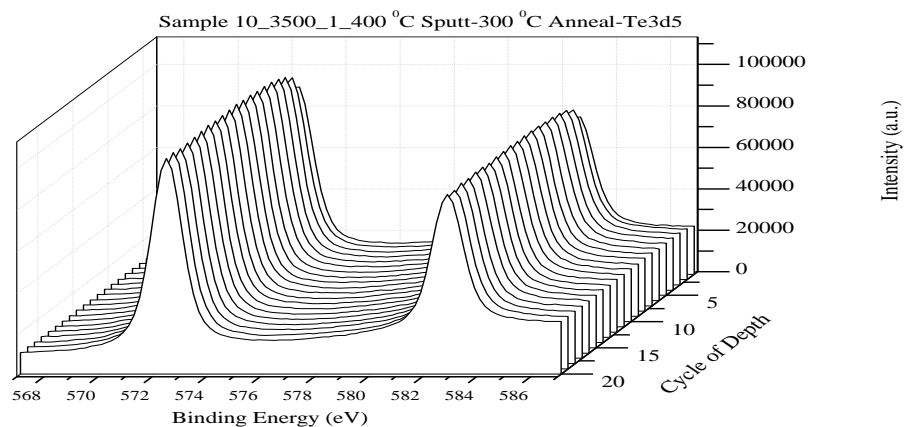


Figure 4.64. XPS spectra of Te3d5 level in the CZT film deposited on glass at $T_s=400^\circ\text{C}$ and at $T_a=300^\circ\text{C}$ for 25 spectra.

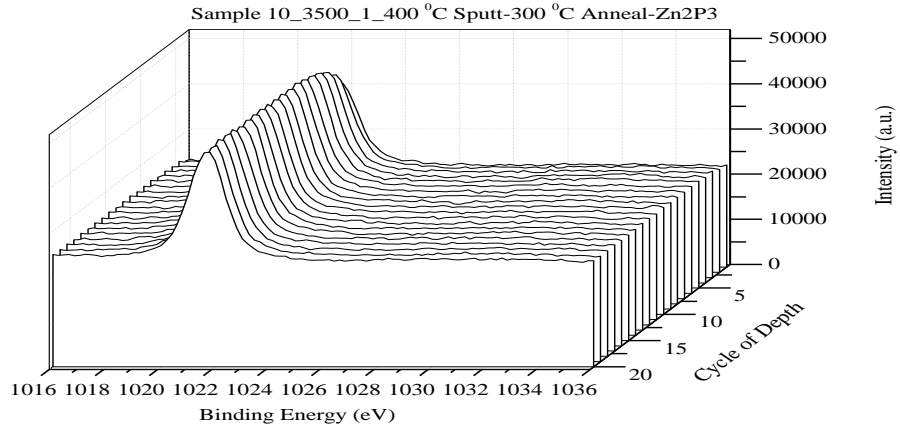


Figure 4.65. XPS spectra of Zn2p3 level in the CZT film deposited on glass at $T_s=400^\circ\text{C}$ and at $T_a=300^\circ\text{C}$ for 25 spectra.

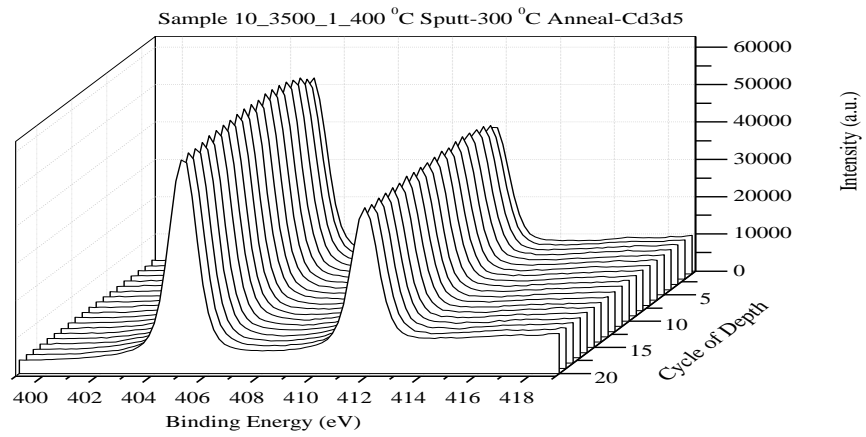


Figure 4.66. XPS spectra of Cd3d5 level in the CZT film deposited on glass at $T_s=400^\circ\text{C}$ and at $T_a=300^\circ\text{C}$ for 25 spectra.

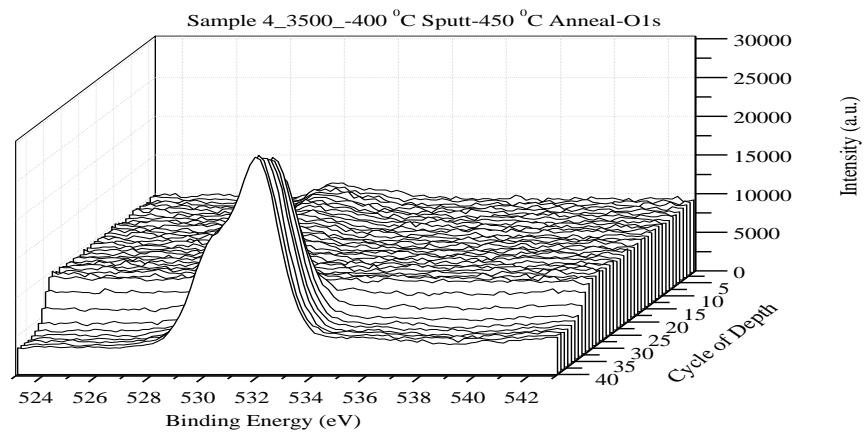


Figure 4.67. XPS spectra of O1s level in the CZT film deposited on glass at $T_s=400^\circ\text{C}$ and at $T_a=450^\circ\text{C}$.

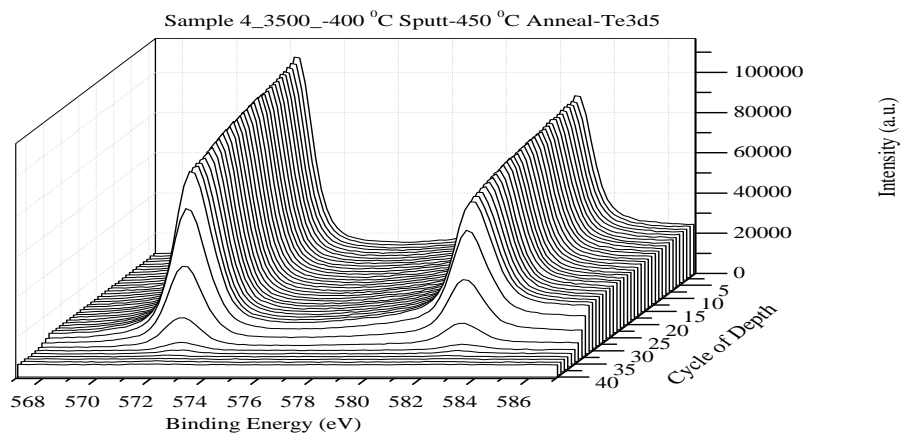


Figure 4.68. XPS spectra of Te3d5 level in the CZT film deposited on glass at $T_s=400^\circ\text{C}$ and at $T_a=450^\circ\text{C}$.

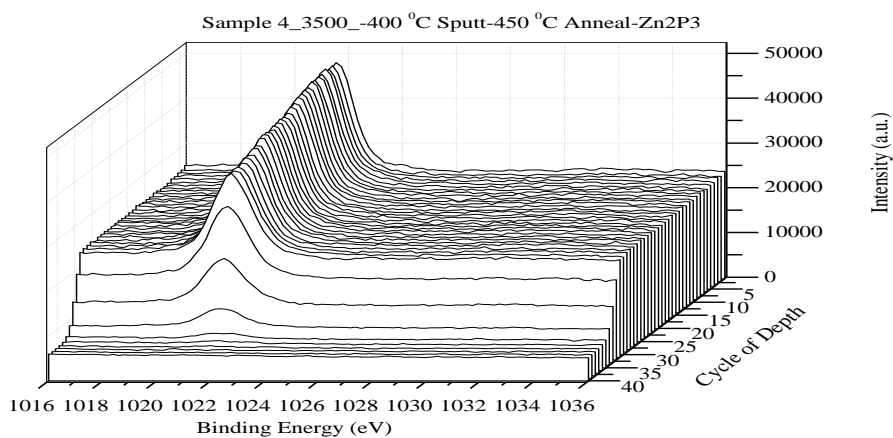


Figure 4.69. XPS spectra of Zn2p3 level in the CZT film deposited on glass at $T_s=400^\circ\text{C}$ and annealed at $T_a=450^\circ\text{C}$.

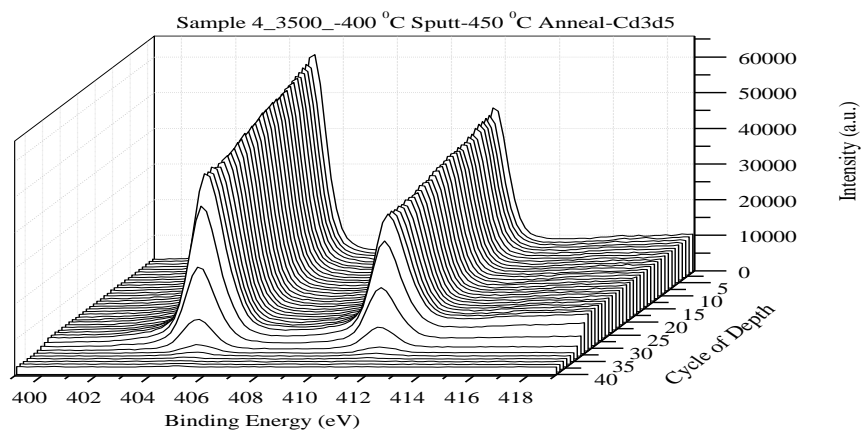


Figure 4.70. XPS spectra of Cd3d5 level in the CZT film deposited on glass at $T_s=400^\circ\text{C}$ and annealed at $T_a=450^\circ\text{C}$.

Consequently, XPS results demonstrate that oxidation only occurs on the all film surface due to oxygen affinity of Te. In addition, CZT layer is uniformly distributed throughout the whole film structures indicating that film stoichiometry is well distributed. On the other hand, it seems that heat treatments slightly enhance Zn concentration in the films.

4.2.5 Optical Analysis

4.2.5.1 Absorption and Transmission Measurements

The film homogeneity, crystallite size and surface roughness of samples were also determined by transmittance spectra. It has been known that low surface roughness, good homogeneity and crystallite films exhibit high transmission spectra. Thermal energy is not enough to create more nuclei at low temperatures and small grains randomly oriented in the structure compared to higher temperatures. Hence, the crystallite size and homogeneity of the film are lower than thin films fabricated at higher T_s . Randomly located high defect densities and vacancies in the structure are contained by lower crystalline films. Therefore, the defects and vacancies in the structure may absorb the incident light and it causes reduction in the transmission. Moreover, the films exhibit higher transmission spectra at lower surface roughness due to the optical scattering nature of the crystal structure. The optical transmittance in the wavelength range 450-700 nm for fabricated CZT films deposited at different sputtering temperatures are measured and displayed in Figs 4.71- 4.73. The spectra show the transmissions are located in the visible region and depend on wavelength and surface morphology. It increases considerably with an increase of T_s and the film deposited at 400°C which is an indication of good crystallinity and low surface roughness obtained the highest transmittance. In addition, the obtained transmission at 400°C T_s is also higher than some other reported value indicating the better crystal quality and transparency for photovoltaic applications.

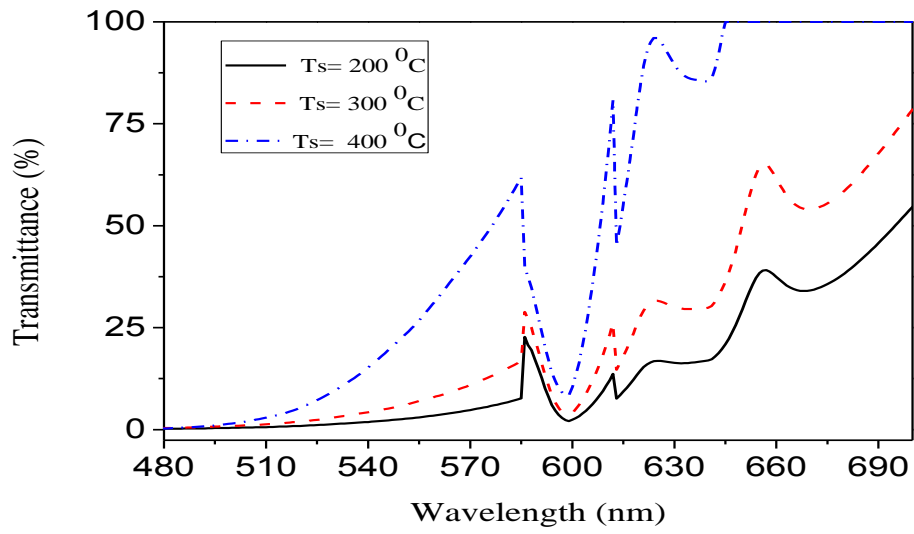


Figure 4.71. Transmission spectra of CZT thin films grown at 200, 300, and 400°C under as grown.

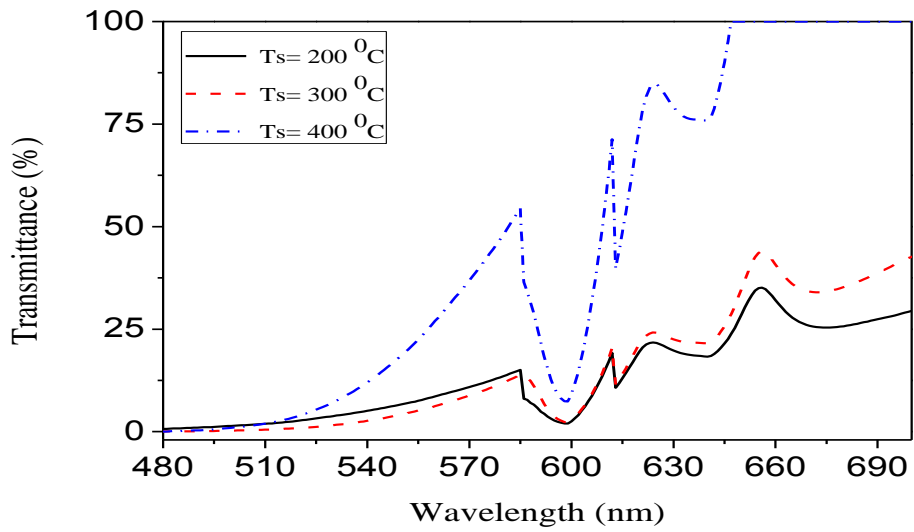


Figure 4.72. Transmission spectra of CZT thin films grown at 200, 300, and 400°C under $T_a=300^\circ\text{C}$.

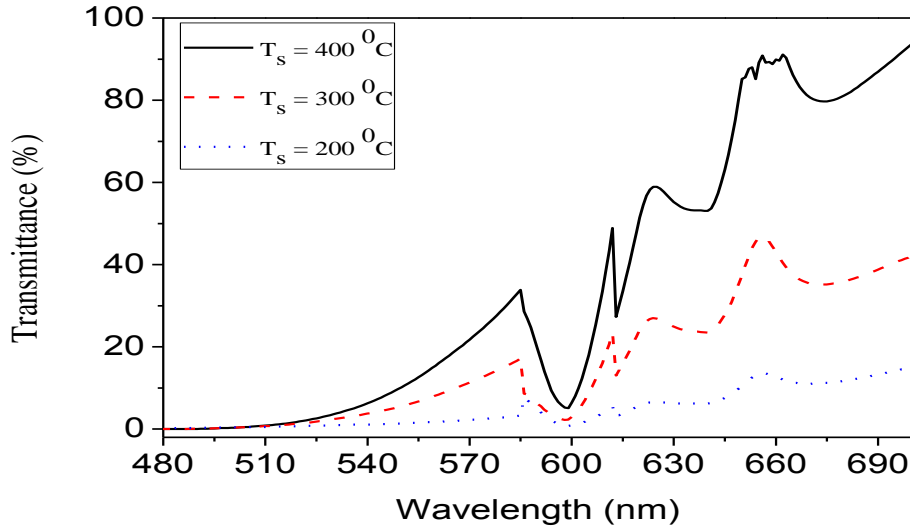


Figure 4.73. Transmission spectra of CZT thin films grown at 200, 300, and 400°C under $T_a=450^\circ\text{C}$.

4.2.5.2 Band Gap of the Deposited CZT Films

We measured the transmission spectra in the region of the optical adsorption band edge for as-deposited and heat-treated CZT patterns. The optical adsorption coefficient (α) was computed from the transmittance using the undermentioned expression $\alpha = (1/t)\ln(100/T)$, where ‘T’ is the transmittance and ‘t’ is the thickness of the crystal. As a direct band gap semiconductor, the crystal under study has an α according the undermentioned expression for high photon energies ($h\nu$): $(\alpha h\nu) = A (E_g - h\nu)^2$, where E_g is the optical band gap of the crystal and A is a constant.

In accord with the relation $(\alpha h\nu) = A (E_g - h\nu)^2$, it would be probable to suit portions of $\alpha h\nu = f(h\nu)$ curves to one or more of the standard dependences, that is, $(\alpha h\nu)^2 = f(h\nu)$ for permitted direct transitions, $(\alpha h\nu)^{2/3} = f(h\nu)$ for banned direct transitions, and $(\alpha h\nu)^{1/2} = f(h\nu)$ for indirect transitions. The analysis of our empirical consequences, (Figs. 4.74- 4.76) exhibit that the best suit is obtained for $(\alpha h\nu)^{1/2} = f(h\nu)$ curves which have a linear portion. As a result, these curves have been utilized for the assessment of the band gap values (Schroder, 2006; Lucaa, and Hsu, 2003; Rusu, 2009; Tigau, 2007; Ting, 2000; Baban et al. 2005).

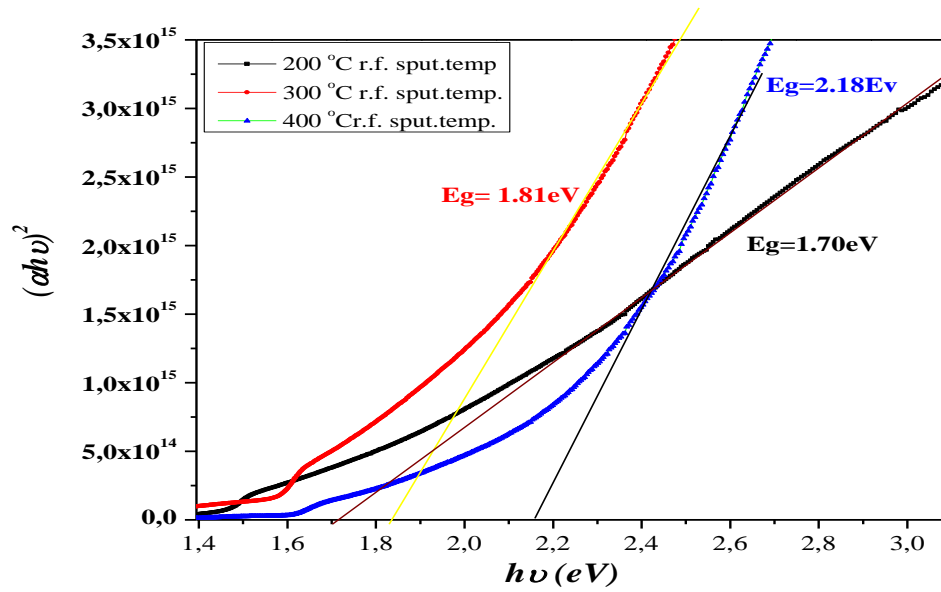


Figure 4.74. UV spectroscopy band gap measurement of CZT thin films grown at 200, 300, and 400°C under as grown.

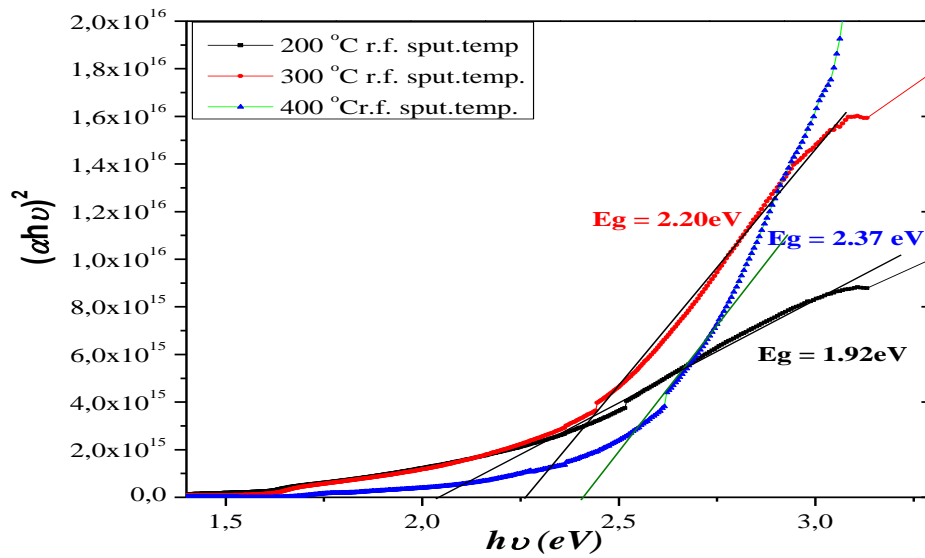


Figure 4.75. UV spectroscopy band gap measurement of CZT thin films grown at 200, 300, and 400°C under $T_a = 300^\circ\text{C}$.

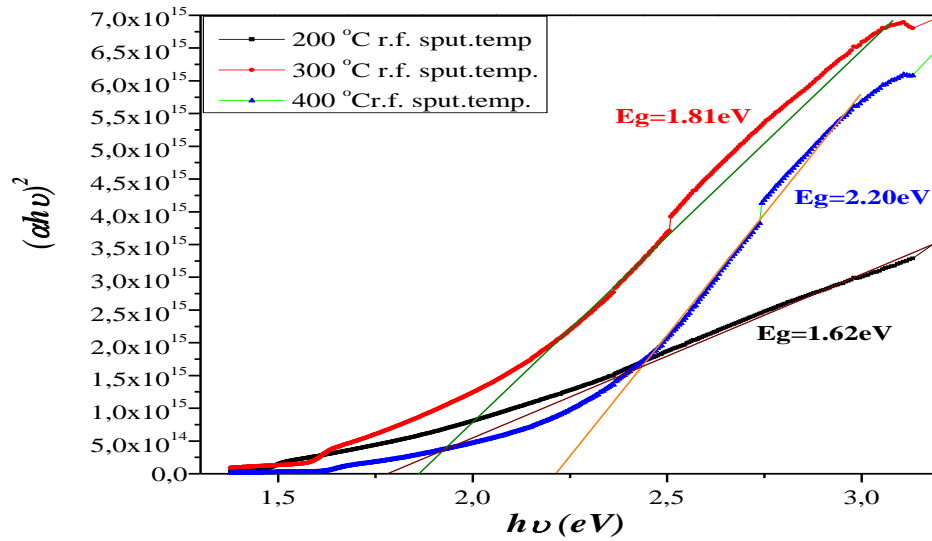


Figure 4.76. UV spectroscopy band gap measurement of CZT thin films grown at 200, 300, and 400°C under $T_a=450^\circ\text{C}$.

The band gap calculation is showed from the UV spectroscopy measurement of CZT in Figures 4.74, 4.75 and 4.76. It can be seen clearly from the Figures that the band gap generally increases with the enhancement of RF sputtering temperature proportionally. The further reduction of the optical band with increase annealing temperature might be owing to the residual free tellurium in the films. The localized sites in the forbidden band can be introduced their no saturated bonds and other structural defects that may be responsible for narrowing of the band gap. The optical band gap shave been appraised as in the range 1.55- 2.24 eV. The acquired values of E_g for different sputtering temperatures are given in tables 4.7 and 4.8. We see that heating the substrate during the deposition causes the band gap CZT increase slightly.

Table 4.7. CZT thin films band gap values calculated annealing under N₂ gases.

R.F. temperature °C	Annealing temperature °C	x by E_g	E_g From Figure eV (Indirect band gap)	E_g calculated from eV $(1.5045+0.631*x+0.128*x^2)$	E_g calculated from eV $(1.5+0.76x)$
200	As grown	0.46	1.82	1.78	1.81
	300	0.50	1.85	1.60	1.61
	450	0.22	1.65	1.53	1.53
300	As grown	0.43	1.80	1.78	1.80
	300	0.93	2.20	1.65	1.67
	450	0.43	1.80	1.65	1.67
450	As grown	0.68	2.15	1.78	1.80
	300	0.97	2.24	1.78	1.80
	450	0.81	2.10	1.65	1.67

Table 4.8. x values from all measurements.

R.F. sputtering temperature °C	Annealing temperature °C	x value from EDXA	x value from XRD	x by E_g	E_g from transmission
200	0	0.43	0.32	0.46	1.70
	300	0.44	0.30	0.50	1.92
	450	0.49	0.14	0.22	1.75
300	0	0.49	0.30	0.43	1.78
	300	0.43	0.31	0.93	2.20
	450	0.49	0.31	0.43	1.77
400	0	0.42	0.35	0.68	2.18
	300	0.40	0.46	0.97	2.40
	450	0.46	0.45	0.81	2.20

5. CONCLUSIONS AND RECOMMENDATIONS

CZT thin films were deposited by a single target sputtering method on heated glass substrates in vacuum medium. Deposition of CZT achieved nano layered CZT structures with uniform content at about 200 nm. With changing exploration settings homogenous CZT thin films can be achieved. The optical band gap of respective films is able to tune from 1.70 to 2.40 eV depending on arranging situations and heat treatment. Consequences show that CZT thin film sputtered at 400°C and annealed at 450°C under the N₂ and N₂H₂ ambient indicated the treatment. The consequences are dedicated the morphology and structure of nanostructure films of hopeful substance as CZT may be useful for experts and researchers. These kind of grown films have also large applications of semiconductor in different optoelectronic tools. Forward studies in this area are on the way to increase the performance of the film and its applications in photovoltaic and imaging tools.

X-ray Photoelectron Spectroscopy, Energy Dispersive X-ray (EDS-EDX), Scanning Electron Microscopy, Atomic Force Microscopy, and X-ray Diffraction Technique techniques were used to characterize CZT thin films.

The XPS measurements have been studied for investigation of homogeneity and chemical bonding on the surface and near to the surface of the CZT thin films. It is observed that oxidation was only occurs in the all film surface due to oxygen affinity of Te. In addition, CZT layer uniformly distributed to whole films structures indicating that films stoichiometry is well distributed. On the other hand, it seems that heat treatments slightly enhance Zn concentration of the films, so this shows that the stoichiometry of ternary films is maintained.

SEM images showed also that post-annealing and deposition temperature has an explicated effect on the modification of the CZT thin film structure and morphology in order to produce a magnified image of the pattern using Scanning Electron microscopy. It can be seen unambiguously that the large accumulation of Te on the surface of the films vanished while the annealing temperature increases,

especially at 450°C annealing temperature Te was vanished so there are some black holes seen in the SEM images.

The using energy dispersive X-ray analysis (EDX or EDS) measurements investigated the chemical composition of source and deposited CZT thin films. On the principle of EDXA analysis, it was found that the as grown films were not stoichiometric; as shown atomic weight of Cd was further than atomic weight of Zn in the composition, which was also substantiated by structural analysis.

The indicating best behavior CZT thin films sputtered at 400°C and annealed at 450°C under the N₂ medium will be used to produce the most sensitive radiation detectors. People will easily save from harmful radiation. Therefore these thin films are going to become the most important device for humanity.

6. REFERENCES

- Ahmed S N (2007) *Physics and Engineering of Radiation Detection*, First Edition, Academic Press Inc. Published by Elsevier, London.
- Ashcroft NW, and Mermin ND (1976) *Solid State Physics*, Thomson Learning, United States of America.
- Aydinly A, Compaan A, Contreras-Puente G and Mason (1991) "Polycrystalline Cd_{1-x}Zn_xTe thin films on glass by pulsed laser deposition", *A Solid State Commun*, 80:465.
- Baban C, Toyoda Y and Ogita M (2005) "Oxygen sensors based on Ga₂O₃ films operating at higher temperature", *J. Optoelectron. Adv. Mater.*, 7:891.
- Bansal A and Rajaram P (2005) "Electrochemical growth of CdZnTe thin films", *Mater. Lett.*, 59:3666.
- Basol M, Kapur VK and Ferris ML (1989) "Low Cost Technique for Preparing Cd_{1-x}Zn_xTe Films for Solar Cells", *J. Appl. Phys.*, 66:1816.
- Basol B M, Halani A, Leidhalm C, Norsworthy G, Kapur V K, Swatzlander A, and Matson R (2000) "Prog. Photovolt", *Res. Appl.*, 8:227.
- Becerril M, Silva-Lopez H and Zelaya-Angel O (2004) "Band gap energy in Zn-rich Zn_{1-x}Cd_xTe thin films grown by r.f. sputtering", *Revista Mexicana de Fisica*, 50:588-593.
- Bencivelli W, Bertoulucci E, Bottigli U, Del Guerra A, Messineo A, Nelson WR, Randaccio P, et al. (1991) "Evaluation of elemental and compound semiconductors for X-ray digital radiography," *Nucl. Instr. Meth.*, A310:210-214.
- Bergstrand ES, Shortt K, KRoss RC and Hole EO (2003) "An investigation of the photon energy dependence of the EPR alanine dosimetry system", *Phys. Med. Biol.*, 48:1753-1771.
- Bertuccio G (2005) "Prospect for energy resolving X-ray imaging with compound semiconductor pixel detectors", *Nucl. Instrum. Meth. Phys. Res.*, 546:232-241.
- Binnig G, Quate CF, and Gerber Ch (1986) "Atomic Force Microscope", *Physical Rev. Lett.*, 56(9): 930-934.
- Bruder M, Schwarz HJ, Schmitt R, Maier H and Omoier M (1990) *J. Cryst. Growth*, 101:266.

Butler JF, Lindgren C L and Doty FP (1992) "Cd_{1-x}Zn_xTe gamma ray detectors", IEEE Trans. Nucl. Sci., 39:605.

Butler F, Doty FP and Apotovsky B (1993) "Gamma- and x-ray detectors manufactured from Cd_{1-x}Zn_x Te grown by a high pressure bridgman method", Mater. Sci. Eng. B, 16:291.

Cavalcoli D, Fraboni B and Cavallini A (2008) "Surface photovoltage spectroscopy analyses of Cd_{1-x}Zn_xTe", Journal of Applied Physics, 103(4):043713.

Chattopadhyaya KK, Sarkar A, Choudhuri S and Pal AK (1991) "Preparation and optical properties of Cd_{1-x}Zn_xTe films", Vacuum, 42:1113.

Chaure NB, Chaure S and Pandey RK (2004) Sol. Energy Mater. Sol. Cells, 81:39.

Chu M, Terterian S, Ting D, Wang CC, Gurgenian HK and Mesropian S (2001) "Tellurium antisites in CdZnTe", Appl. Phys. Lett., 79:2728.

Chu TL, Chu SS, Ferekides C and Herrington C (1986) "Deposition and properties of zinc telluride and cadmium zinc telluride films", J. Appl.Phys., 59:1259.

Chu T L, Chu S S, Britt J, Ferekides C and Britt J (1992) "Cadmium Zinc Sulfide films and Heterojunctions", J. Appl. Phys., 71:5635.

Costa N and Cartaxo A (2010) Advances in Lasers and Electro Optics, Croatia.

Coutts TJ, Emery K, and Ward JS (2002) Prog Photovolt: Res Appl., 10(3):195-203.

Cullity BD (1978) Elements of X-ray Diffraction. Addison-Wesley, Second Edition.

Debertin K and Helmer R G (1988) Gamma-and X-Ray Spectrometry with Semiconductor Detectors, Elsevier, Amsterdam.

Derbin A, Khusainov A, Muratova V, Mouratov O and Arlt R (2001) Nucl. Instr. And Meth., 458:169.

Del Sordo S, Abbene L, Caroli E, Mancini AM, Zappettini A and Ubertini P (2009) "Progress in the Development of CdTe and CdZnTe Semiconductor Radiation Detectors for Astrophysical and Medical Applications", Sensors, 9:3491-3526.

Dhere R, Gessert T, Zhou J, Asher S, Pankow J and Moutinho H (2003) Material Research Society Symposium Proceedings, 763:409.

Dinan JH and Qadri SB (1985) "Heteroepitaxial growth of ZnCdTe by molecular beam epitaxy", Vac. Sci. Technol., 3:851.

Eaton P and West P (2010) Atomic Force Microscopy, Oxford University Press, New York.

Eisen Y (1974) "Current state-of-the-art industrial and research applications using room-temperature CdTe and CdZnTe solid state detectors", Nucl. Instr. Meth., 117:431-439.

Enderlein R and Horing NJM (1997) Fundamentals of Semiconductor Physics and Devices, World Scientific, Singapore.

Fougeres P, Siffert P, Hageali M, Koebel JM and Regal R (1999) "CdTe and Cd_{1-x}Zn_xTe for Nuclear detectors: facts and fictions", Nucl. Instr. Meth., 428:38-44.

Fiederle M, Feltgen T, Meinhardt J, Rogalla M, and Benz KW (1999) "State of the art of (Cd,Zn)Te as gamma detector", J. Cryst. Growth, 197:635.

Frank F C and Van der Merwe J H, (1949) Proc. R. Soc. London, Ser. A. 198:205.

Fu D J, Lee JC, Choi S W, Lee SJ, Kang TW, Jang MS, Lee HI and Woo YD (2002) "Study of ferroelectricity and current-voltage characteristics of CdZnTe Appl.", Phys. Lett., 81:5207

Gaduputi J (2004) "Characterization of Cadmium Zinc Telluride Films and Solar Cells on Glass and Flexible Substrates by RF Sputtering", M. S., Master of Science in Electrical Engineering Department of Electrical Engineering College of Engineering University of South Florida.

Ghosh B, Ghosh D, Hussain S, Bhar R and Pal AK (2012) "Growth of ZnTe lms by pulsed laser deposition technique", Journal of Alloys and Compounds, 541:104-110.

Goela JS, and Taylor RL (1987) "Growth of CdZnTe on Si by Low-Pressure Chemical Vapor Deposition", Appl. Phys. Lett., 51:928.

Goldstein JI, et al. (2003) Scanning Electron Microscopy and X-ray Microanalysis, 3rd Edition Plenum Press, New York.

Gonzales-Hernandes J, Zelaya JO, Mendoza-Alvares JG, Lopez-Cruz E , Pawlick D A and Alred DD (1991) J. Vac. Sci. Technol., 9:550.

Greenberg JH (1999) "Vapor pressure scanning implications of CdTe crystal growth." J. Crystal Growth, 197:406.

Guskov VN, Greenberg JH, Fiederle M and Benz K-W (2004) J. Alloys Compounds, 371:118.

Haloui A, Feutelais Y and Legendre B (1997) "Experimental Study of the Ternary System Cd-Te-Zn", J. Alloys Compounds, 260:179.

[http:// www.foothills-analytical.com/EDX.html](http://www.foothills-analytical.com/EDX.html) - 4k (04 May 2013).

<http://www.intertek-cb.com/microscopy/SEMAnalysisLaboratories.shtml> (05 July 2012).

http://www.sckcen.be/microstructure/Infrastructure/XPS/Infrastructure_XPS.htm (08 Jude 2013).

<http://www.quality-analysis.de/de/raster> (08 March 2013).

Iller A, Karczewski G, Kolmhofer G, Eusakowska E, and Sitter H (1998) *Crystal Research Technology*, 33:401.

Iwanczyk J S, Patt BE, Wang YJ, and Khusainov AKh (1996) “Comparison of HgI₂, CdTe, and Si (p-i-n) X-ray detectors”, *Nucl. Instr. Meth.*, 380:186-192.

James RB, and Siffert P, Eds. (2001) 11th International Workshop on Room Temperature Semiconductors and Associated Electronics, *Nucl. Instrum. Methods Phys. Res. A*, 458:1- 603.

Jursinic PA (2007) “Characterization of optically stimulated luminescent dosimeters, OSLDs, for clinical dissymmetric measurements”, *Medical Physics*, 34 (12), December.

Kaleli M (2010) “Investigation of Electrical and Optical Properties of Ag-In-Se Based Devices”, PhD, Thesis in Physics Department of Middle East Technical University and Natural and Applied Sciences, Ankara.

Kim KH, Na YH, Park YJ, Jung TR, Kim SU and Hong JK (2004) “Characterization of High-Resistivity Poly-CdZnTe Thick Films Grown by Thermal Evaporation Method”, *IEEE Trans. Nucl. Sci.*, 51:3094.

Lecomber PG and Mort J (Eds.), (1973) Academic, London and New York.

Li G, Jie W, Wang T and Gu Z (2004) “Characteristics of doped indium in Cd_{0.9}Zn_{0.1}Te grown by the Bridgman method”, *Semicond. Sci. Technol.*, 19:457.

Lucaa D and Hsu LS (December 2003) “Structural Evaluation and optical properties of TiO₂ Thin Films Prepared by Thermal Oxidation of PLD Ti Films”, *Journal of Optoelectronics and Advanced Materials*, 5(4):835.

LuttgeInna A, Andrew K, and Barron R, <http://cnx.org/> (14 July 2014).

Luque A, and Hegedus S (2005) *Handbook of Photovoltaic Science and Engineering.*, John Willey and Sons.

Maissel LI, and Francombe MH (1973) *An Introduction to Thin Films.* Gordon and Breach Science Publishers, New York-London-Paris.

Malkas H, Kaya S, and Yilmaz E (2014) “Effects of Substrate Temperature on the Microstructure and Morphology of CdZnTe Thin Films”, *Journal of Electronic Materials*, 43(11):4011-4017.

Mattox DM (1998) *Handbook of Physical Vapor Deposition (PVD) Processing,* Noyes Publications.

Moshfegh AZ, Kanel HV, Kashyap SC and Wuttig M (2004) *Physics and Technology of Thin Films IWTF 2003*, World Scientific Publishing.

Nette P and Svensson (1994) *Radiation dosimetry in health care: Expanding the reach of global Networks*, IAEA BULLETIN, 4.

Neamen DA (2003), *Semiconductor Physics and Devices*, Third Edition, McGraw-Hill, Newyork.

Neumark GF (1997) "Defects in Wide Bandgap II-VI Crystals", *Mater. Sci. Eng. Rep.*, 21:1.

Niemela A and Sipila H (1994) "Evaluation of CdZnTe Detectors for Soft X-Ray Applications", *IEEE Trans. Nucl. Sci.*, 41:1054.

Ohring M, (2002) *Materials Science of Thin Films - Deposition and Structure*, Academic Press, San Diego.

Owens A, and Peacock A (2004) "Compound semiconductor radiation detectors", *Nuclear Instruments and Methods in Physics Research*, 531:18–37.

Pellicary B, Chamonal JP, Destefanis GL and DiCiocio L (1988) *Proc. SPIE* 865:22-29.

Peter C, Graat J, Marcel A and Somers J (1996) *Applied Surface Science* 100/101, 36-40.

Philips B (2006) Ed. 15th International Workshop on Room-Temperature Semiconductor X- and Gamma-Ray Detectors, *IEEE Nucl. Sci. Symp. Conf. Re.*, 6:3585-3939.

Polit JJ, Sheregii EM, Burattini E, Marcelli A, Cestelli Guidi M, Calvani P, Nucara A, Piccinini M, Kisiel A, Konior J, Sciesińska E, Sciesiński J and Mycielski A (2004) "Analysis of phonon spectra of the $Zn(x)Cg(1-x)Te$ solid-solution", *J. Alloys Comp.*, 371:172-176

Prabakar K, Ventkatachalam SaK, Jeyachandram YL, Narayandass S and Mangalaraj D (2004a) *Sol Energy Mater Sol Cells*, 81(1):1-12.

Phabakar K, Narayandass SK and Mangalaraj D (2004b) "Effect of annealing on the optical constants $Cd_{0.2}Zn_{0.8}Te$ thin films", *J. Alloys Compounds*, 364:23.

Rajavel D and Zinck JJ (1993) "Metalorganic molecular beam epitaxial growth of high-quality $Cd_{1-x}Zn_xTe$ ($0 \leq x \leq 0.27$) films," *Appl. Phys. Lett.*, 63:322.

Ray B (1969) *II-VI Compounds*. Pergamon Press, First Edition, Oxford.

Reimer L, (1985) *Scanning Electron Microscopy*, Springer-Verlag, Berlin.

Ringel SA, Sudharshanan R, Rohatgi A and Carter WB (1990a) "A Study of $Cd(Zn,Mn)Te/CdS$ Films and Interfaces", *J. Electron. Mater.*, 19:259-263.

- Ringel SA, Sudharshanan R, Rohatgi A, Owens MS and Gills HP (1990b) "Effects of Annealing and Surface Preparation on the Properties of MBE-Grown Polycrystalline CdZnTe Films", *J. Vac. Sci. Technol.*, 8:2012-2016.
- Rizzi M, Maurantonio M and Castagnolo B (2005) "Novel micro strips system detectors for medical applications", *WSEAS Trans. Biol. Biomed.*, 2:220-227.
- Rizzi M, Maurantonio M and Castagno B (2006) "Comparative analysis of GaAs, CdTe, and CdZnTe Radiation detectors", *WSEAS Trans. Elect.*, 3:7-13.
- Rohatgi A, Sudharsanan R and Ringel SA (1991) "Growth and Process Optimization of Polycrystalline CdTe and CdZnTe Films for High Efficiency Solar Cells", *Solar Cells*, 30:109-122.
- Reno JL and Jones EJ (1992) "Determination of the Dependence of the Band-Gap Energy on Composition for Cd_{1-x}Zn_xTe", *Phys. Rev.*, B 45:1140.
- Rudolph P (2003) "Non-stoichiometry related defects at the melt growth of semiconductor compound crystals", *Cryst. Res. Technol.*, 38(7-8):542-554.
- Russ JC (1984) *Fundamentals of Energy Dispersive X-ray Analysis*, Butterworths. London.
- Rusu G and Rusu M (2005) "Optical Behavior of Multilayered CdTe/Cu Thin Films Deposited by Stacked Layer Method", *J. Optoelectronic. Adv. Mater.*, 7 (2): 885.
- Rusu GG (2006) "Structural, Electronic Transport and Optical Properties of Zn-doped CdTe Thin Films", *J. Optoelectron. Adv. Mater.*, 8:931.
- Rusu GG Rusu M and Girtan M (2007) "Optical characterization of vacuum evaporated CdZnTe thin films deposited by a multilayer method", *Vacuum*, 81:1476.
- Rusu GI (2009) "Electronic and Optical Properties of Some Polysulfone-Polydimethylsiloxane Copolymers in Thin Films", *Journal of Macromolecular Science R, Part B: Physics*, 48:238-253.
- Samantha B, Sharma SL, and Choudhuri AK (1994) "Optical and micro structural properties of Cd_{0.8}Zn_{0.2}Te thin films," *Ind. J. Pure, Appl. Phys.*, 32, 62.
- Sato G, Takahashi T, Sugiho M, Kouda M, Mitani T, Nakazawa K, Okada Y and Watanabe S (2001) "Characterization of CdTe/CdZnTe detectors", *IEEE Transactions on Nuclear Science*, XX (Y).
- Schropp REI, Stannowski B, Brockhoff AM, van Veenendaal PATT and Rath JK (2000) "Hot Wire CVD of Heterogeneous and Polycrystalline Silicon Semiconducting Thin Films For Application in Thin Film Transistor and Solar Cells", *Materials Physics and Mechanics*, 73-82.
- Sharma R, Dori, Chandra S and Misra K (2000) *Proc. SPIE* 3975:1278.

Scheiber C (2000) "CdTe and CdZnTe gamma ray detectors in nuclear medicine", Nucl. Instr. Meth., A448:513-524.

Schlesinger TE, Toney JE, Yoon H, Lee EY, Brunett BA, Franks L and James R (2001) "Cadmium zinc telluride and its use as a nuclear radiation detector material", Mater. Sci. Eng. Rep., 32:103.

Schimmel T, Koch T, Kupperts J and Lux-Steiner M (1999) Applied Physics A: Materials Science & Processing, 68(4):399-402.

Schlesinger TE and James RB (1995) "Semiconductors for Room Temperature Nuclear Detector Application", Semiconductors and semimetals, San Diego, Academic Press, p 18.

Schroder K (2006) Semiconductor Material and Device Characterization , Third Edition, A. John Wiley & Sons, Inc., Publication Hoboken, New Jersey.

Schwank JR, Roeske SB, Beutler DE, Moreno DJ and Shaneyfelt MR, (Dec.1996) "A dose rate independent PMOS dosimeter for space application", IEEE Trans. Nucl. Sci., 43:2671.

Stranski JN, and Krastanov L (1938) Ber. Akad. Wiss. Wien 146, p.797.

Sugimoto Y, Abe M, Jelinek P, Perez R, Morita S and Custance O (2007) Nature, 446(7131):64.

Sullivan CJ, Morrell JL, Allison DP, Doktycz M (2005), "Mounting of Escherichia Coli Spheroplasts for AFM Imaging", J. Ultramicroscopy 105:96.

Suryanarayana C, and Norton GM, (1998) X-ray Diffraction: a practical approach, Plenum Press, New York.

Sykes D, UK Surface Analysis Forum <http://www.uksaf.org/group/gang.html> (05March 2013).

Tigau N (2007) "Structure and electrical conduction of Sb₂S₃ thin films", Cryst. Res. Technol., 42:281.

Ting CC (2000) "Structural Evolution and Optical Properties of TiO₂ Thin Films Prepared by Thermal Oxidation of Sputtered Ti Films", Journal of Applied Physics, 88(8):4628-4633.

Tavernier S (2010) Experimental Techniques in Nuclear and Particle Phys., Springer-Verlag Berlin, Heidelberg, Dordrecht, London, New York.

Tromas C, Eaton P, Mimault J, Rojo J and Penade's S (2005) Langmuir 21(14):6142.

Van de Walle C G (1989) "Band lineups and deformation potentials in the model-solid theory", Physical Review B, 39(3):1871.

Venkataraman R and Croft S (2003) "Determination of plutonium mass using gamma-ray spectrometry", Nucl. Instrum. Methods Phys. Res. A, 505 (1-2), 527.

Vydyanath HR, Ellsworth JA and Fisher RF (1993) "Vapor phase equilibria in the $\text{Cd}_{1-x}\text{Zn}_x\text{Te}$ alloy system," J. Electron.Mater. 22:1067.

Volmer M, and Weber ZA (1926) Phys. Chem., 119:277.

Wagendristel A and Wang Y (1994) "An Introduction to Physics and Technology of Thin Films". World Scientific Publishing, Singapore-New Jersey-London-Hong Kong.

Watts JF and Wolstenholme (2003) An Introduction to Surface Analysis by XPS and AES. John Willey and Sons Ltd.

Yacobi BG (2002) Semiconductor Materials: An Introduction to Basic Principles Kluwer Academic/Plenum Publishers, London.

Zelaya-Angel O, Mendoza-Alvarez JG, Becerril M, Navaro-Contreras N, Tirado-Nejia N (2004) "On the bowing parameter in $\text{Cd}_{1-x}\text{Zn}_x\text{Te}$ ", J Appl. Phys., 95(11):6284-8.

7. CURRICULUM VITAE

Name SURNAME : Hasan Malkaş

Place and Date of Birth : Istanbul 08.12.1968

Universities

Bachelor's Degree : İnönü Üniversitesi

MSc Degree : İnönü Üniversitesi

e-mail : hasan.malkas@inonu.edu.tr

Address : Inonu University Malatya Junior Technical College
44200 Battalgazi/Malatya

List of Publications : Yilmaz E, Malkas H, Kaya S, Aktag A, Karacali H, Kahraman A and Lok R (2015) “A Detailed Study on The Structural and Optical Characterization of CdZnTe Thin Films For photovoltaics”, 3rd Turkish Solar Electricity Conference & Exhibition” April 27-29 2015, Middle East Technical University, Ankara.

Malkas H, Kaya S and Yilmaz E (2014) “Effects of Substrate Temperature on the Microstructure and Morphology of CdZnTe Thin Films”, Journal of Electronic Materials, 43(11):4011-4017.

Kaya S, Malkas H and Yilmaz E (2014) “Influence of Sputtering Temperature on Surface Morphology of CdZnTe Thin Films”, 1st International Semiconductor Science and Technology Conference, Istanbul.

İde S, Ancin N, Malkas H and Öztaş SG (2007) “Structural features of some diorganotin (IV) complexes of ONO donor Schiff bases”, Acta Cryst., A63, s169. 24th European Crystallography Meeting, 22-27 August 2007, Morocco, Marrakech.

Atalay S, Şahingöz R and Malkas H, (1996) “Magneto-inductive effect in rapidly solidified CoSiB wires” Rapidly Quenched and Metastable Materials RQ9 Ninth Conference, Elsevier pbl., 251-253, Bratislava, Slovakia, 25-30 August, 1996.

Atalay S and Malkas H, (1995) “Influence of Annealing on Magneto-Inductive Effect in FeSiB Amorphous Wires”, 6th European Magnetic Materials and Application Conference, Wien (Also, to be published J. Mag. Mag. Mater.).

Uluğ B, Malkas H ve Aytekin Ö (1993) “Argon ortamının C_{20+2H} Moleküllerinin eldesine Etkisi”, 14. Ulusal Fizik Kongresi, Lefkoşe.

Awards :

Hobbies (Optional) :